Centre Énergie Matériaux et Télécommunication

IMPACT OF OXYGEN ON THE CONDUCTION MECHANISM THROUGH $Hf_{0.5}Zr_{0.5}O_2$ FOR ReRAM MEMORY APPLICATIONS

Par

Yoandris Lazaro GONZALEZ HERNANDEZ

Thèse présentée pour l'obtention du grade de
Philosophiae Doctor (Ph.D.)
en sciences de l'énergie et des matériaux

Jury d'évaluation

Président du jury et examinateur interne	Prof. Sharif SADAF Institut National de la Recherche Scientique Centre Énergie Matériaux et Télécommunication
Examinateur externe	Prof. Matthew DAWBER Department of Physics and Astronomy Stony Brook University
Examinateur externe	Prof. Aimé PELAÍZ BARRANCO Faculty of Physics University of Havana
Directeur de recherche	Prof. Andreas RUEDIGER Institut National de la Recherche Scientique Centre Énergie Matériaux et Télécommunication

ACKNOWLEDGMENTS

First, I would like to acknowledge my supervisor Andreas Ruediger who welcomed me at INRS and allowed me to conduct my research in a privileged technological environment. Thank you for establishing a climate of trust and enjoyable conditions to exchange ideas throughout the last four and a half years. It has been an absolute pleasure to work with you!

I would like to express my sincere thanks to the jury members who agreed to evaluate this thesis, Prof. Sharif Sadaf of INRS-EMT, Prof. Matthew Dawber of Stony Brook University, and Prof. Aimé Pelaíz of University of Havana.

I would also like to mention our industrial partner Plasmionique Inc. and its leader Andranik Sarkissian, for their assistance in all aspects of sputtering.

I would also like to thank all my colleagues who are part of the Nanophononics Nanoelectronics group. Thank you for the pleasant exchanges and rich scientific working environment. I would like to specifically thank the members with whom I have been able to publish throughout my time at INRS, notably Azza, Ifeanyi, Rajesh, Clarick, Gitanjali, Andreas D., Mohamed D., Bernhard, Johannes, and Georgios. A few special mentions go to my office mates and friends Aura, Azza, and Lilian. When my English was barely enough to say “yes” and “no,” Aura was my first interpreter. She was also a reassuring reminder of the people I had to leave back home. I sincerely thank you for your friendship, Aura. Azza, thank you for the training on all laboratory equipment and for the elaborate and relevant scientific discussions. Meeting Lilian made me a better person. Many of our conversations about politics or other topics happened at our lunch table, during which I always learned something new or was pushed to question my opinions. Thank you!

I would also like to thank the INRS Mexican Community, where I was welcomed with open arms as early as my first day in Canada. Thanks to Juan Carlos, Uriel, Angel, Fabiola, Aura, Alonso, Mike.

Thank you also to my previous supervisors, Maruchy and Melo, with whom I have maintained a close friendship and a productive scientific collaboration.

Finally, I want to thank my entire family with a special thought for my lovely wife, and my mother. Thank you very much for the support and for allowing me the freedom of choice during these long studies. Without you, I wouldn’t be where I am today. Thank you.

RÉSUMÉ

Les jonctions tunnel ferroélectriques (*Ferroelectric Tunnel Junctions* – FTJs) sont des mémoires résistives non volatiles émergentes qui promettent de combiner la polyvalence de la ReRAM (*Resistive Random Acces Memory*) de l'informatique neuromorphique avec la résistance en fatigue bien établie des dispositifs ferroélectriques. Une FTJ comprend deux électrodes métalliques entourant une couche ferroélectrique ultrafine (métal/ferroélectrique/métal). Le développement et l'introduction des FTJs dans les processus industriels étaient initialement limités, entravés par l'incompatibilité des matériaux ferroélectriques disponibles avec la technologie CMOS (*Complementary Metal-Oxide Semiconductor*) et la difficulté de réduire la taille à quelques nanomètres. La récente découverte de la ferroélectricité dans le HfO_2 dopé ouvre la voie à des dispositifs de mémoire FTJ entièrement compatibles avec la technologie CMOS. En outre, il est possible d'obtenir une plasticité fonction du temps d'occurrence des impulsions (*Spike-Time-Dependent-Plasticity* – STDP) dans les FTJ, ce qui souligne leur potentiel pour l'informatique neuromorphique. La phase orthorhombique ($Pca2_1$) est largement acceptée comme responsable de la ferroélectricité dans le HfO_2 dopé. Cependant, cette phase ferroélectrique est une phase métastable. Par conséquent, des recherches approfondies visant à stabiliser cette phase non centrosymétrique sont en cours, notamment en ce qui concerne le dopage, la déformation, l'énergie à la limite de la surface/interface/grain, la température de recuit et les lacunes d'oxygène introduites intentionnellement.

Néanmoins, bien que ces mécanismes améliorent les propriétés ferroélectriques des couches minces à base de HfO_2, ils ont également un effet adverse sur les performances d'une FTJ à base de HfO_2. Dans cette thèse, nous nous intéressons à l'influence des lacunes d'oxygène sur la formation de la phase ferroélectrique orthorhombique dans $Hf_{0,5}Zr_{0,5}O_2$ et aux mécanismes de conduction de charges à travers cette couche. Cette étude utilise la pulvérisation cathodique magnétron à radiofréquence pour fabriquer des structures TiN/$Hf_{0,5}Zr_{0,5}O_2$/Au, dans lesquelles la pression partielle d'oxygène pendant le dépôt de la couche à base de $Hf_{0,5}Zr_{0,5}O_2$ était variable. L'intensité du pic de diffraction (111) de $Hf_{0,5}Zr_{0,5}O_2$ correspondant à la face orthorhombique a augmenté lorsque la concentration en oxygène a été réduite dans la chambre de pulvérisation. Cette augmentation de la phase orthorhombique est associée à la génération de défauts dans la couche mince de $Hf_{0,5}Zr_{0,5}O_2$, soit en conséquence d'une déficience en oxygène lors du dépôt. Une étude plus approfondie des implications de ces défauts dans le mécanisme à effet tunnel à travers le $Hf_{0,5}Zr_{0,5}O_2$ est fournie. Les échantillons déposés sous atmosphère riche en oxygène

(p_{O_2}= 67%) se sont avérés appropriés pour un effet tunnel direct. En revanche, ceux obtenus sous atmosphère semi-déficiente en oxygène (p_{O_2}= 50%) étaient favorables à l'effet tunnel assisté par piège. Il a également été démontré que la formation d'un filament de lacunes d'oxygène est possible pour les échantillons déposés sous atmosphère totalement appauvrie en oxygène (p_{O_2}= 0%). Nos résultats corroborent le processus de recuit thermique rapide (*Rapid Thermal Annealing* - RTA) comme une voie directe pour la formation de la phase ferroélectrique orthorhombique ($Pca2_1$) dans $Hf_{0,5}Zr_{0,5}O_2$. De plus, une amélioration de la phase ferroélectrique dans les couches minces de $Hf_{0,5}Zr_{0,5}O_2$ déposées sous atmosphère sans oxygène a été démontrée. Le test d'endurance démontre la stabilité des dispositifs à effet tunnel direct par rapport à ceux basés sur l'effet tunnel médié par pièges. En utilisant le modèle PATT (*Phonon-Assisted Tunnelling between Traps*), il a été possible d'obtenir la distance moyenne entre les pièges. Une épaisseur critique pour le mécanisme dominant à effet tunnel direct a été déterminée à partir d'une analyse comparative des modèles PATT et à effet tunnel direct (approximation de Wentzel-Kramers-Brillouin). De même, la comparaison de différentes densités de pièges (distance moyenne entre les pièges) nous permet de déterminer le seuil de distance moyenne entre les pièges pour la prévalence des mécanismes à effet tunnel. Ce travail fournit donc un intervalle d'épaisseurs de couches minces et de densités de pièges pour des performances optimales d'effet tunnel dans les FTJs

Mots-clés: FTJ, ReRAM, Lacunes d'oxygène, $Hf_{0,5}Zr_{0,5}O_2$, Effet tunnel direct, Effet tunnel assisté par pièges.

ABSTRACT

Ferroelectric tunnel junctions (FTJs) are emerging non-volatile resistive memory holding the promise of combining the versatility of resistive random-access memory (ReRAM) in neuromorphic computing with the well-established fatigue resistance of ferroelectric devices. An FTJ comprises two metallic electrodes surrounding an ultrathin ferroelectric layer (metal/ferroelectric/metal). The development and introduction of FTJs into industrial processes were initially limited, impeded by the incompatibility of available ferroelectric materials with CMOS technology and the difficulty of scaling down to a few nanometers. The recent discovery of ferroelectricity in doped-HfO_2 paves the way for fully CMOS-compatible FTJ memory devices. In addition, it is possible to achieve spike-time-dependent-plasticity (STDP) in FTJs, highlighting its potential for neuromorphic computing. The orthorhombic phase ($Pca2_1$) is widely accepted as responsible for ferroelectricity in doped-HfO_2. However, this ferroelectric phase is a metastable phase. Therefore extensive research to stabilize this non-centrosymmetric phase is ongoing, including doping, strain, surface/interface/grain boundary energy, annealing temperature and intentionally introduced oxygen vacancies.

Nevertheless, while these mechanisms improve the ferroelectric properties of HfO_2-based films, they also adversely affect the performance of an HfO_2-based FTJ. In this thesis, we focus on the influence of oxygen vacancies on the formation of the ferroelectric orthorhombic phase in $Hf_{0.5}Zr_{0.5}O_2$ and on the mechanisms of charge conduction through this film. This study uses radio frequency magnetron sputtering to fabricate TiN/$Hf_{0.5}Zr_{0.5}O_2$/Au structures, in which the oxygen partial pressure during $Hf_{0.5}Zr_{0.5}O_2$ film deposition was variable. The diffraction peak (111) intensity of $Hf_{0.5}Zr_{0.5}O_2$ corresponding to the orthorhombic phase increased when the oxygen concentration was reduced in the sputtering chamber. This enhancement of the orthorhombic phase is associated with the generation of defects in the $Hf_{0.5}Zr_{0.5}O_2$ film as a consequence of oxygen-deficient deposition. Further investigation of the implications of such defects in the tunneling mechanism through the $Hf_{0.5}Zr_{0.5}O_2$ is provided. Samples deposited in an oxygen-rich atmosphere (p_{O_2}= 67%) were demonstrated to be suitable for direct tunneling. In contrast, those obtained in a semi-oxygen-deficient atmosphere (p_{O_2}= 50%) were favourable for trap-assisted tunneling. It was also demonstrated that the formation of an oxygen vacancy filament is possible for samples deposited in a fully oxygen-depleted atmosphere (p_{O_2}= 0%). Our results corroborate the rapid thermal annealing (RTA) process as a straightforward pathway for forming the ferroelectric orthorhombic phase ($Pca2_1$) in $Hf_{0.5}Zr_{0.5}O_2$. Furthermore, an enhancement of the ferroelectric phase in $Hf_{0.5}Zr_{0.5}O_2$ films deposited in an oxygen-free atmosphere was demonstrated. The endurance test demonstrates the stability of direct tunneling devices over those based on trap-mediated tunneling. Using the phonon-assisted tunneling between traps (PATT) model was possible to obtain the average distance between traps. A critical thickness for a dominant direct tunneling mechanism was determined from a comparative analysis of the PATT and direct tunneling (Wentzel-Kramers-Brillouin approximation) models. Likewise, comparing different trap densities (average distance between traps) allows us to determine the average distance between traps threshold for the prevalence of the tunneling mechanisms. This work, therefore, provides a window of thin film thicknesses and trap densities for optimal FTJ tunneling performance.

Keywords: FTJ, ReRAM, Oxygen vacancies, $Hf_{0.5}Zr_{0.5}O_2$, Direct tunneling, Trap-assisted tunneling.

TABLE OF CONTENTS

LIST OF FIGURES

LIST OF TABLES

LIST OF EQUATIONS

LIST OF ABBREVIATIONS

RAM: random-access memory

SRAM: static random-access memory

DRAM: dynamic random access memory

HDD: hard disc drive

SSD: solid state discs

USB: universal serial bus

SD: secure digital

MOSFET: metal–oxide–semiconductor field-effect transistor

FeRAM: ferroelectric random-access memory

ReRAM: resistive random-access memory

MRAM: magnetic random-access memory

PRAM: phase-change random-access memory

MIM: metal-insulator-metal

FTJ: ferroelectric tunnel junction

FE: ferroelectric

TER: tunneling electroresistance effect

CMOS: complementary metal-oxide semiconductor

HRS: high resistance state

LRS: low resistance state

STDP: spike-time-dependent-plasticity

RF: radiofrequency

E_c: coercive field

ALD: atomic layer deposition

PVD: physical vapor deposition

NVM: non-volatile memories

OxRAM: oxide-based random-access memory

CBRAM: conductive bridging random-access memory

VCM: valence change memories

TE: top electrode

BE: bottom electrode

FNT: Fowler-Nordheim tunneling

DT: direct tunneling

PFE: Poole-Frenkel emission

SCLC: space-charge-limited conduction

TAT: trap-assisted tunneling

WKB: Wentzel-Kramers-Brillouin

J: current density

SCLC: space-charge-limited conduction

PAT: phonon-assisted tunneling

DC: direct current

PID: proportional–integral–derivative

XRR: X-ray reflectivity

GIXRD: grazing incidence X-ray diffraction

AFM: atomic force microscopy

SMU: source measurement unit

RMS: root mean square

XRD: X-ray diffraction analysis

RTA: rapid thermal annealing

PATT: phonon-assisted tunneling between traps

SCIENTIFIC CONTRIBUTIONS

Publications

1- M. Delfag, G. Rachovitis, **Y. González**, J. Jehn, A. Hadj Youssef, C. Schindler, and A. Ruediger, “Fully printed ZnO-based valency-change memories for flexible and transparent applications” *Flex. Print. Electron*. **2022**

2- C. Calvo, V. Torres-Costa, **Y. González**, A. Ruediger, M. Sánchez, G. Santana, G. Contreras-Puente, C. de Melo, J. Ghanbaja and O. de Melo. “Temperature dependence of Raman and photoluminescence spectra of pure and high-quality MoO_3 synthesized by Hot Wall Horizontal Thermal Evaporation” *J. Alloys Compd.* 924, 166545 ,**2022**.

3- I. Amaechi, A. Hadj Youssef, A. Dörfler, **Y. González**, R. Katoch, and A. Ruediger. “Catalytic Applications of Non-Centrosymmetric Oxide Nanomaterials: A review” *Angew. Chem. Int. Ed.* **2022**

4- O. de Melo, M. Ramírez-López, M. Pérez-Caro, S. Gallardo-Hernández, Y.L. Casallas, M. Sánchez, J. Ortega, G. Santana, M. Behar, **Y. González** and M. López-López “Indium incorporation at $In_xGa_{1-x}N$ relaxed self-assembled nanostructures on Si substrates” *Mater. Sci. Semicond. Process.*150 (1), 106946, **2022**.

5- **Y. González**, A. Hadj Youssef, R. Katoch, A. Dörfler, S. Asadollahi, A. Sarkissian and A. Ruediger “Mechanism of oxygen vacancy filament-based resistive switching in non-polar $Hf_{0.5}Zr_{0.5}O_{2-\delta}$ thin films” *ACS Appl. Electron. Mater.* 4 (3) 1311–1317, **2022**

6- C. Oliveira Soares, G. Buvat, **Y. González**, S. Garbarino, M. Duca, A. Ruediger, G. Denuault, A.C. Tavares, and D. Guay, " Au (001) Thin Films: Impact of Structure and Mosaicity on the Oxygen Reduction Reaction in Alkaline Medium" *ACS Catal.* 12 (3), 1664–1676, **2021**

7- **Y. González**, A. Hadj Youssef, A. Dörfler, R. Katoch, A. El Mesoudy, A. Sarkissian, D. Drouin, and A. Ruediger “Competing tunneling conduction mechanisms in oxygen-deficient $Hf_{0.5}Zr_{0.5}O_2$” *Appl. Phys. Lett.* 119, 132906, **2021**

8- A. Hadj Youssef, G. Kolhatkar, I. C Amaechi, R. Katoch, **Y. González**, A. Merlen and A. Ruediger, “Giant step bunching on $SrTiO_3$ thin films grown epitaxially on vicinal MgO (100) surfaces,” *Appl. Surf. Sci.*, 570, 151266, **2021**

9- M. Delfag, R. Katoch, J. Jehn, **Y. González**, C. Schindler, and A. Ruediger, “Sinter-free inkjet-printed PEDOT:PSS/WO_3/PEDOT:PSS flexible valency change memory,” *Flex. Print. Electron.*, 6, 035011, **2021**

10- **Y. González** A. Abelenda, O. de Melo, C. Calvo-Mola, L. García-Pelayo, B.J. García and M. Sánchez, “Automated system for surface photovoltage spectroscopy,” *Rev. Sci. Instrum.*, 92, 013104, **2021**

11- O. de Melo, V. Torres-Costa, **Y. González**, A. Ruediger, C. de Melo, J. Ghanbaja, D. Horwat, A. Escobosa, O. Concepción, G. Santana and E .Ramos, “Interfacial strain defines the self-organization of epitaxial MoO_2 flakes and porous films on sapphire: experiments and modelling,” *Appl. Surf. Sci.*, 514, 145875, **2020**

12- J. Zhang, **Y. González**, R. Sany, and A. Ruediger, “A facile fabrication procedure for platinum nanoprobes with high-aspect-ratio and low tip radii via electrochemical etching,” *Rev. Sci. Instrum.*, 91, 033702, **2020**

13- G. Kolhatkar, B. Mittermeier, **Y. González**, F. Ambriz-Vargas, M. Weismueller, A. Sarkissian, C. Gomez-Yanez, R. Thomas, C. Schindler and A. Ruediger, “$BiFe_{1-x}Cr_xO_3$ Ferroelectric Tunnel Junctions for Neuromorphic Systems,” *ACS Appl. Electron. Mater.*, 1, 828–835, **2019**

14- O. de Melo, **Y. González**, A. Climent-Font, P. Galán, A. Ruediger, M. Sánchez, C. Calvo, G. Santana and V. Torres-Costa, “Optical and electrical properties of MoO_2 and MoO_3 thin films prepared from the chemically driven isothermal close space vapor transport technique,” *J. Phys. Condens. Matter*, 31, 295703, **2019**

Conferences

1- M. Delfag, R. Katoch, J. Jehn, **Y. González**, C. Schindler and A. Ruediger, *"Sinter-free inkjet-printed PEDOT:PSS/WO_3/PEDOT:PSS flexible valency change memory"* 2021 IEEE 16th Nanotechnology Materials and Devices Conference (NMDC), 12-15 Dec 2021, pp. 1-1, doi: 10.1109/NMDC50713.2021.9677487. Vancouver, Canada

2- **Y. González**, R. Katoch, A. Dörfler, A Hadj Youssef, S. Netzke, S. Urquhart, D. Drouin, A. Sarkissian, A. Ruediger *“Effect of Oxygen Deficiency on the Resistive Switching of $Hf_{0.5}Zr_{0.5}O_2$ Ferroelectric Tunnel Junctions”* Oral presentation IEEE ISAF-ISIF-PFM May 16-21, 2021 Virtual Conference

3- **Y. González**, R. Katoch, A. Dörfler, A. Sarkissian, D. Drouin, S. Netzke, S. Urquhart and A. Ruediger, *“Trap assisted- versus direct tunneling in CMOS-compatible ferroelectric tunnel junctions based on $Hf_{0.5}Zr_{0.5}O_2$”* Oral presentation XV Symposium of the Cuban Physics Society, March 9-13, 2020, Havana, Cuba

4- R. Arriaga, R. Katoch, **Y. González**, A. Dörfler, F. Ambriz-Vargas, A. Hadj Youssef, G. Kolhatkar, A. Sarkissian, C. Gómez Yáñez, A. El Mesoudy, S. Netzke, S. Urquhart, A. Ruediger. “*CMOS compatible $Hf_xZr_{1-x}O_2$ ferroelectric tunnel junctions*”. Oral presentation IEEE ISAF-ICE-EMF-IWPM-PFM, July 14-19, 2019, Lausanne, Switzerland.

5- G. Kolhatkar, B. Mittermeier, **Y. González**, F. Ambriz-Vargas, M. Weismueller, A. Sarkissian, C. Gomez-Yanez, R. Thomas, C. Schindler, A. Ruediger. *“$BiFe_{1-x}Cr_xO_3$ ferroelectric tunnel junctions for non-volatile memories and neuromorphic computing”* International Conference on Memristive Materials, Devices & Systems, Memrisys2019, 8-11 July 2019 Dresden, Germany.

6- V. Torres-Costa, **Y. González**, N. Cornejo-Gómez, M. Manso-Silván, C. de Melo, J. Ghanbaja, D. Horwat, G. Santana and O. de Melo. *“Influence of the substrate in the morphology and crystalline orientation of MoO_2 flakes grown by chemically driven isothermal close space vapor transport”* Oral presentation XI International Conference on Surfaces, Materials and Vacuum, 23-28 September 2018, Playa del Carmen, Mexico.

7- O. de Melo, M. Manso-Silván, A. Climent-Font, P. Galán, **Y. González**, M. Sánchez, C. Calvo, V. Torres-Costa and G. Santana, “Properties and oxidation of MoO_2 films grown by chemically driven isothermal close space vapor transport” Oral presentation XI International Conference on Surfaces, Materials and Vacuum, 23-28 September 2018, Playa del Carmen, Mexico.

1 INTRODUCTION

Nowadays, smartphones, computers, and tablets are an integral part of our daily lives, and their use has become widespread among an ever-increasing proportion of the population; an example of mobile subscribers in the Canadian population is shown in Figure 1-1. According to Statistics Canada, in 2020, 84.4% of Canadians owned a smartphone, an increase of 4.1 percentage points since 2018 [1]. This spread of electronic devices is the consequence of extremely rapid progress in the microelectronics industry since the 1970s. These electronic devices are supported by integrated circuits, which enable their diverse functions. These integrated circuits (or chips) are built up of several transistors, which are the basic unit of these circuits. In 1965, Gordon Moore introduced an empirical law that predicted that the density of these transistors would double every 18 months, known as Moore's law [2]. The industry's efforts to follow this prediction resulted in a drastic reduction in manufacturing costs, which made electronic devices accessible to a more significant number of people, as well as increased their portability.

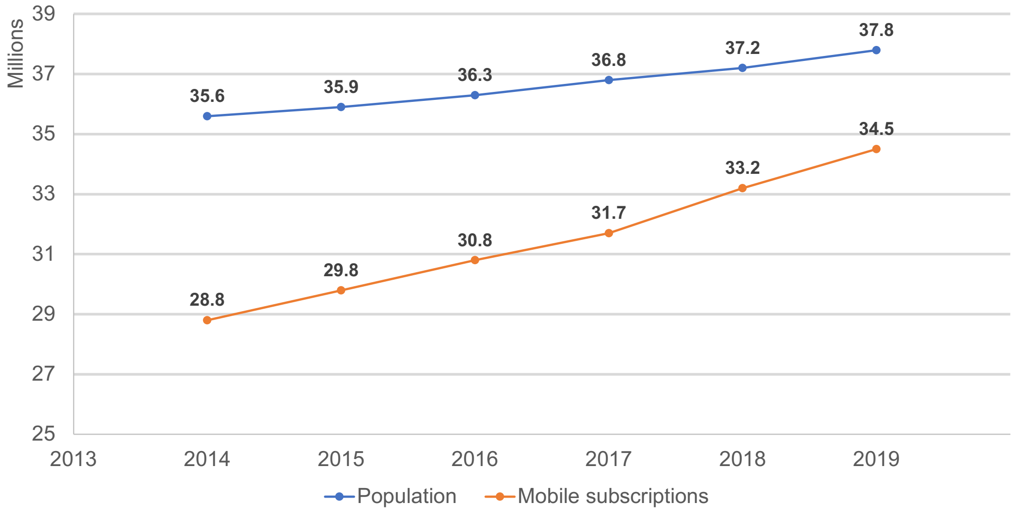

Figure 1-1: Mobile subscribers and population in Canada.

Figure adapted from [1].

At the same time, these constant reductions in feature sizes responded to a rapidly increasing demand for information storage (music, photos, videos, etc.). This continuously growing market has been driven by advances in non-volatile memory (memory that retains information after the power supply has been cut off) and, in particular, the arrival of flash memory in the mid-1980s, which completely revolutionized the market [3].

In current computer systems, information is encoded in binary form and stored in three different types of memory:

- Static random-access memory (SRAM), the closest to the arithmetic logic unit, is a high-speed type of memory with a large footprint of typically six transistors and, for that matter, is relatively expensive.
- Dynamic random access memory (DRAM), also known as “working memory,” is based on charge storage in a capacitor.
- Mass storage either in a magnetic hard disc drive (HDD) or via Flash memory in solid state discs (SSD).

The former two types of memory are volatile, and HDDs rely on failure-prone mechanical components. For this reason, Flash has emerged as the dominant type of mass storage in recent years ranging from Universal Serial Bus (USB) sticks to secure digital (SD) cards for cameras and phones to large-capacity devices such as SSD. Flash memories are based on the floating gate Metal–oxide–semiconductor field-effect transistor (MOSFET). It is a field-effect transistor whose gate metal is totally isolated from the rest of the structure by an oxide. Like in a conventional transistor, a difference of potential generates a channel of electrons between the source and drain. Above a threshold voltage applied to the control gate, some very energetic electrons are injected into a reservoir across an insulator barrier. This way, these electrons are trapped in the gate metal even after the power is removed. In terms of information, an absence of charges trapped in the metal corresponds to a "1" in binary coding, while the presence of charge corresponds to a "0".

The MOSFET is relatively inexpensive and can easily follow the overall scaling of semiconductor technology. However, the technology is energy-inefficient, slow, and gradually approaches its physical limits of scalability since the device becomes sensitive to the tunneling effect at nanometric dimensions, causing substantial load losses and leakage currents [4].

In response to this problem, new non-volatile memory concepts have been developed to replace floating gate MOSFETs. These concepts are either charge- or resistance-based. Ferroelectric memories (FeRAM) are an example of charge-based devices with intrinsic critical scaling limitations as the feature size decreases to dimensions that do not allow for the storage of a sufficient number of charges to be detected (and amplified) by a transistor. Resistive random-access memories (ReRAMs) overcome this problem by storing information in multiple resistance states. In the case of a binary device, these two resistance states represent a zero and one. Integrating the current that passes through such a device provides the required charges to trigger a read transistor. For that matter, even a very low current that results from a high resistance in a very small device may still yield sufficient charges for sufficiently long integration times. In other words, resistive RAM provides the opportunity for a trade-off between size and readout speed. Among these resistive RAMs, different concepts have progressed beyond the prototyping stage, including magnetic memories (MRAM), phase-change RAMs (PRAMs), and conducting filament RAM. For the latter, there are again multiple sub-categories, including metallic filamentary switching (conductive bridge RAM or electrochemical metalization cells) and valency change memory, that rely on the reversible formation of a localized conduction path across a metal-insulator-metal (MIM) structure. Among the most recent contenders for non-volatile resistive memory, we find ferroelectric tunnel junctions (FTJs) that hold the promise of combining the fatigue resistance of ferroelectric devices with the compatibility of circuitry for resistive memories.

An FTJ is a resistive random-access memory composed of two metallic electrodes surrounding an ultrathin ferroelectric (FE) layer (Metal/Ferroelectric/Metal), presenting two stable polarization states at zero applied field. The polarization direction of the FE layer can be switched from one of these memory states to the other by an electric field exceeding the coercive field. The surface charges associated with the permanent polarization induce a modulation of the barrier height, significantly altering the stack's tunneling current, known as the tunneling electroresistance effect (TER) [5].

The TER effect in a memory cell was experimentally demonstrated in 2009 using an ultrathin layer of $BaTiO_3$ as a ferroelectric barrier [6, 7]. The experimental demonstration of an FTJ memory device based on perovskite materials triggered intense research on its properties. High fatigue resistance (endurance ~ 10^6 cycles) [8] due to its non-destructive readout operation [9], high speed (written speed down to 10 ns) [10], high scalability [11] and a simple architecture [5] are the key advantages of this technology over the classic Flash or DRAM memories.

However, despite the excellent memory properties of FTJ devices, their introduction into the semiconductor market has been restricted, as the integration of FTJs with ultrathin ferroelectric films with perovskite structure in conventional Si-based memory technology (CMOS) remains a challenge for essentially three reasons: I) the limitation of thermal budget for front- and even back-end-of-CMOS processes since perovskites require crystallization temperatures and times that exceed the tolerances of CMOS technology, II) the lack of compatibility of most ternary metal oxides with silicon. As Hubbard *et al.* [12] and Schlom *et al.* [13] pointed out, a rule-of-thumb about the compatibility of a ternary oxide with silicon is whether the constituent binary oxides are individually compatible with silicon, excluding, e.g. those perovskites with a TiO_2 sublattice such as $BaTiO_3$, $PbTiO_3$ and their derivates $Ba_xSr_{1-x}TiO_3$ and $PbZr_xTi_{1-x}O_3$, and III) the sensitivity of most perovskite ferroelectrics to forming gas, a common chemical in the semiconductor industry to limit or reverse effects of oxidation. So, there was a strong demand for a CMOS-compatible ferroelectric throughout the evolution of micro- and nanoelectronics.

In the early 2000s, ferroelectric tunnel junctions were demonstrated based on $BaTiO_3$ [6, 7] ultrathin films and soon after with $BiFeO_3$ [9] and yet, while these early investigations were valuable as a proof of concept underlining the tremendous potential of FTJs as non-volatile memories, triggering broader interest in the field, they remained of primarily academic interest for the aforementioned reasons of material incompatibility with industrial processes.

The discovery of ferroelectricity in silicon-doped hafnium oxide by Böscke *et al.* in 2011 [14], boosted the interest in ferroelectric tunnel junction memories. Suggested as a CMOS-compatible material in 2002 by Gilmer *et al.* [15], Intel fully integrated hafnium oxide into CMOS fabrication processes as of 2007 [16]. Moreover, the ferroelectricity of doped HfO_2 was demonstrated for thicknesses even below 10 nm [17], paving the way for fully CMOS-compatible FTJ memory devices.

The basic model of ferroelectric tunnel junctions is based on two distinct states of polarization that yield two resistive states. These resistive states are commonly referred to as high resistance state (HRS) and low resistance state (LRS) and are associated with “OFF” and “ON” or “0” and “1,” respectively. These terms are not unified but widely consistent throughout the literature. As Gruverman *et al*. [18] pointed out, the mechanism of heterogeneous domain nucleation at the beginning of the switching process provides a progressive, strictly monotonous polarization reversal that is a function of both the applied bias voltage and the duration of its application. In other words, the overall area of a ferroelectric capacitor will not switch instantaneously rather than progressively, leaving a large number of possible intermediate area fractions of reversed polarization that are generally stable even without bias. So, while each area fraction (i.e. domains of possibly different sizes) between the electrodes only has two possible polarization states, the integrated polarization across the entire surface changes gradually during the switching event [19]. Now, all these domains create a network of parallel resistors for a given FTJ. Therefore, during polarization reversal, the resistance state will change gradually between the HRS and LRS or vice versa [9].

Consequently, it is possible to achieve multi-level switching, which allows for the storage of n bits for each 2^n distinguishable resistance state. For the extreme case of quasi-continuous resistance changes, which has been shown to be possible with FTJs [20, 21], it is possible to achieve spike-time-dependent-plasticity (STDP), a phenomenon known from synapses. While the biological analogy is strictly speaking the result of overlapping signals from two neighboring nerve cells, their superposition is generally well represented by a single voltage pulse with defined duration and amplitude. These voltage pulses are able to tune the resistance state of a synapse that will retain that state subsequently until another pulse arrives. Such a “training” of resistances in a neural network is a key feature for learning. Ferroelectric tunnel junctions are clearly able to mimic this capacity. Since they are two-terminal devices, their integration into crossbar arrays for neuromorphic computing is also the subject of current research in a different research project of our team.

Since 2011, a cornucopia of studies has been carried out on this type of memory. Furthermore, still, several challenges remain in order to considering integration by the industry.

The non-centrosymmetric orthorhombic phase of space group $Pca2_1$ is widely accepted as responsible for the ferroelectricity in HfO_2-based thin films [22-24]. However, it is a metastable phase. Numerous efforts have been made to stabilize this non-centrosymmetric phase, including tuning properties such as doping [25], strain [26, 27], surface/interface/grain boundary energy [28], annealing temperature [29], and intentionally introduced oxygen vacancies [30-32]. Nevertheless, while these mechanisms improve the ferroelectric properties of HfO_2-based films, they also adversely affect the performance of an HfO_2-based FTJ. During the first few memory life cycles, the remnant polarization values gradually increase (in absolute value) as the cycling proceeds until they reach their maximum value and stabilize. This phenomenon is called “wake-up” and is attributed to a redistribution of oxygen vacancies in the material [33]. A decrease in remnant polarization values marks the memory life, which corresponds to fatigue of the ferroelectric material attributed to an increase in the number of defects generated (e.g. oxygen vacancies) in the material. So, while the effect of oxygen vacancies at the early stage of polarization reversal in hafnia-based devices is beneficial to the remnant polarization, the ultimate consequence of oxygen vacancy migration causes fatigue, i.e. a reduction of reversible polarization after numerous cycles.

Oxygen vacancies, therefore, need to be considered as a key element in understanding the electronic properties of ferroelectric tunnel junctions based on doped HfO_2. In particular, they also influence the conduction mechanisms in the structure. In this work, we investigate the effect of oxygen vacancies on the tunneling mechanism in $Hf_{0.5}Zr_{0.5}O_2$ tunnel junctions and these films. As we will show, it is possible to switch from direct tunnel conduction to phonon-assisted tunneling between traps conduction [34] or even further to the oxygen vacancy filaments formation [35].

An important question resulting from all these considerations is how the competition between the idealized ferroelectric tunnel junction switching and oxygen vacancy-based tunneling mechanisms affects the opportunities to deploy these devices.

1.1 Research objectives

This thesis investigates the role of oxygen vacancies in the electrical conduction mechanism through $Hf_{0.5}Zr_{0.5}O_2$ deposited by radiofrequency (RF) magnetron sputtering and its applications for ReRAM memory. This relates to the following specific objectives:

- i) Stabilize the ferroelectric orthorhombic phase ($Pca2_1$) in $Hf_{0.5}Zr_{0.5}O_2$ and determine its dependence on oxygen partial pressure during radiofrequency magnetron sputtering of $Hf_{0.5}Zr_{0.5}O_2$.
- ii) Fabrication of thin films with a controlled thickness of $Hf_{0.5}Zr_{0.5}O_2$ with and without polar order. The thickness needs to be controlled with sufficient precision to obtain ultrathin films with charge transport in the tunneling regime and slightly thicker films where, e.g. thermionic mechanisms prevail. This objective deals in particular with the control of deposition parameters to decouple the oxygen vacancy concentration from the growth rate.
- iii) Identification of the dominant charge transport mechanisms based on a microscopic model of possibly coexisting and competing tunneling mechanisms.
- iv) Extraction of material parameters e.g. oxygen vacancy concentration from quantitative experiments of charge transport across ferroelectric tunnel junctions.
- v) The start of an investigation on how these oxygen vacancies affect the fatigue behavior of ferroelectric tunnel junctions.

1.2 Thesis outline

This dissertation is divided into five chapters, as follows:

- i) The Introduction to this dissertation.
- ii) The fundamentals chapter discusses the principles of ferroelectricity and its origin and causes in hafnium oxide-based films. This chapter also outlines the fundamentals of emerging non-volatile memories, particularly ferroelectric tunnel junction memories. The last section of this chapter presents the possible conduction mechanisms in metal-insulator-metal structures.

iii) The materials and methods chapter is dedicated to presenting RF sputtering as the thin-film synthesis technique used in this study. In addition, the characterization techniques employed are described, such as X-Ray diffraction, atomic force microscopy, and several electrical characterizations.

iv) The results and discussions chapter is structured in three sections. The first section presents and discusses the general characteristics of the TiN/$Hf_{0.5}Zr_{0.5}O_2$/Au structures. In addition, the influence of oxygen partial pressure on the formation of the ferroelectric orthorhombic phase is investigated. The second section studied the conduction mechanisms for two oxygen partial pressures. By fitting the I-V characteristic for both cases with the direct tunneling and trap-assisted tunneling models, we obtain parameters that allow us to establish the conditions for which one mechanism will predominate over the other. The last section presents a resistive switching memory based on oxygen vacancy filaments in non-polar $Hf_{0.5}Zr_{0.5}O_{2-\delta}$ thin films. Features of these memories are presented, such as endurance and retention, as well as a discussion of the conduction mechanisms.

v) The conclusions and perspectives chapter includes a summary of the effect of oxygen partial pressure during $Hf_{0.5}Zr_{0.5}O_2$ sputtering on charge transport through the TiN/$Hf_{0.5}Zr_{0.5}O_2$/Au structures is given at the end of the present document. The chapter also highlights recommendations for future studies.

2 FUNDAMENTALS

This chapter discusses the fundamentals of ferroelectricity. The class of HfO_2-based ferroelectrics is introduced, discussing advantages over perovskite-based ferroelectrics in scalability and CMOS compatibility. The origins of ferroelectricity in HfO_2-based ferroelectrics are explored. In the second half of the chapter, resistive non-volatile memories are discussed. The operation, advantages, and disadvantages of ferroelectric and ferroelectric tunnel junction memories are examined. The last part of this chapter will be dedicated to presenting the most common conduction mechanisms in metal-insulator-metal type memory structures.

2.1 Ferroelectricity

Crystals are classified according to seven systems of symmetry. These systems are triclinic, monoclinic, orthorhombic, tetragonal, trigonal, hexagonal, and cubic in increasing symmetry order (i.e. number of symmetry operations). Depending on the number of symmetries, these systems can be subdivided into so-called point symmetry groups, also known as crystal classes. There are 32 crystallographic point groups.

As shown in Figure 2-1, 11 of the 32 crystal classes are centrosymmetric. When a constant strain is applied to a centrosymmetric crystal, the charge displacement is symmetrically distributed around the center of symmetry, so the relative charge displacements are fully compensated on a macroscopic scale. This effect inhibits the occurrence of ferroelectric polarization-related properties.

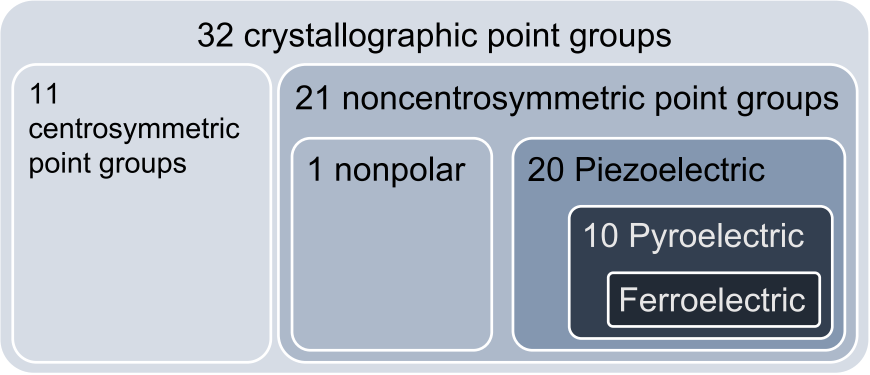

Figure 2-1: Classification of the 32 crystallographic point groups.

Of the remaining 21 non-centrosymmetric crystal structures, all but one show polarization when subjected to mechanical stress. This effect is called the piezoelectric effect. Both it and its reciprocal effect are linear and reversible, i.e., the application of an electric field induces a strain in the material. A subgroup of 10 piezoelectric crystals has a single axis of symmetry, which makes its members polar i.e., exhibiting a spontaneous polarization. This spontaneous polarization is usually temperature-dependent, and its existence can be detected as a flow of charges from one surface to another through an external circuit with the variation of temperature; the latter is called the pyroelectric effect. Finally, the spontaneous polarization of certain pyroelectrics is reversible under an external electric field and remains non-zero when the field is removed. These are called ferroelectrics materials. Ferroelectricity is a cooperative phenomenon [36], i.e. the spontaneous polarization of a unit cell interacts with adjacent cells, orienting them in the same direction. It was first observed in 1920 by Joseph Valasek during experiments on Rochelle salt [37].

These aforementioned groups can be summarized by their contribution to the electric displacement (D_i) equation.

Equation 2-1: Electric displacement

$$D_i = \underbrace{\varepsilon_0 \varepsilon_{ij} E_j}_{I} + \underbrace{d_{ik} T_k}_{II} + \underbrace{\gamma_i \Delta T}_{III} + \underbrace{P_i^s}_{IV}$$

where $\boldsymbol{\varepsilon_0}$ **is the vacuum permittivity,**
$\boldsymbol{\varepsilon_{ij}}$ **is the permittivity tensor,**
$\boldsymbol{E_j}$ **is the electric field in direction** $\boldsymbol{j}$**,**
$\boldsymbol{d_{ik}}$ **is the piezoelectric tensor,**
$\boldsymbol{T_k}$ **is the mechanical stress,**
$\boldsymbol{\gamma_i}$ **is the pyroelectric coefficient,**
$\boldsymbol{\Delta T}$ **is the change of temperature, and**
$\boldsymbol{P_i^s}$ **is the spontaneous polarization.**

The first term (I) of equation 2-1 is relevant to all 32 crystal classes. The second term (II) represents the piezoelectric effect, while the third term (III) corresponds to the pyroelectric effect. The spontaneous polarization inherent to ferroelectrics is considered in the electric displacement equation's fourth term (IV).

Polarization is, therefore, the characteristic quantity of a ferroelectric. Microscopically, it emerges from a dipole moment formed by the delocalization of the barycenter of the positive and negative charges of the crystal lattice.

Using Gauss' law, the surface charge (Q) enclosed by a surface *S* can be expressed as the volume integral of the polarization.

Equation 2-2: Gauss's law

$$-Q = \oiint_S \vec{P} dA$$

Figure 2-2 shows a typical class of ferroelectric material structure called perovskite: a metal ion, such as Ti or Zr, is embedded in an oxygen octahedron stretched in a given orientation (along the c-axis in the diagram). This deformation leads to a position of the metal ion slightly displaced from the center of the octahedron. Resulting in an electric dipole moment in the crystal lattice since the barycenter of the negative charges induced by the oxygen atoms no longer coincides with the metal ion, which carries the positive charges. In the case of perovskites, the atoms surrounding the crystal lattice are also metal ions (such as Pb or Ba), but their participation in the dipole moment is negligible. The following illustrations of the microscopic origin of spontaneous polarization start with the perovskite structure for which it is easier to visualize the respective displacements of the barycentre's of charge. With the knowledge about this structure, we will then illustrate the microscopic origin of spontaneous polarization in the fluorite structure of $Hf_{0.5}Zr_{0.5}O_2$ (Figure 2-5).

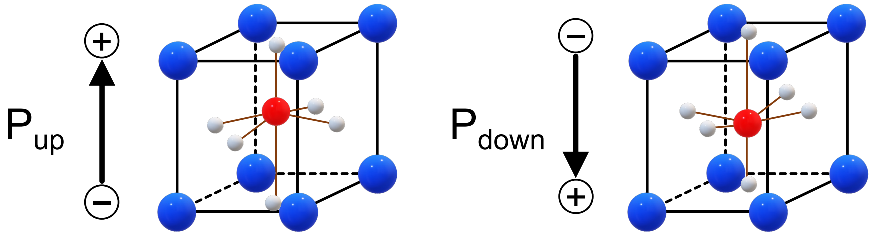

Figure 2-2: Atomic structures of perovskite oxides ABO_3.

Atomic structures of ferroelectric perovskite oxides ABO_3 for the upward and downward polarization. The oxygen anions (gray) in the horizontal plane of the structure undergo a small displacement in the opposite direction of the central B-cation (red), thus providing long-range ordering.

2.1.1 Domains and polarization

The definition of a ferroelectric can be summarized through the hysteresis cycle linking the spontaneous polarization to the applied electric field (Figure 2-3). Initially directed in one direction, the polarization flips in the other direction, i.e. for the case of a perovskite, the B-site cation in Figure 2-2 moves from one position to the other when a strong electric field is applied in that direction. This field is called the coercive field, noted E_c.

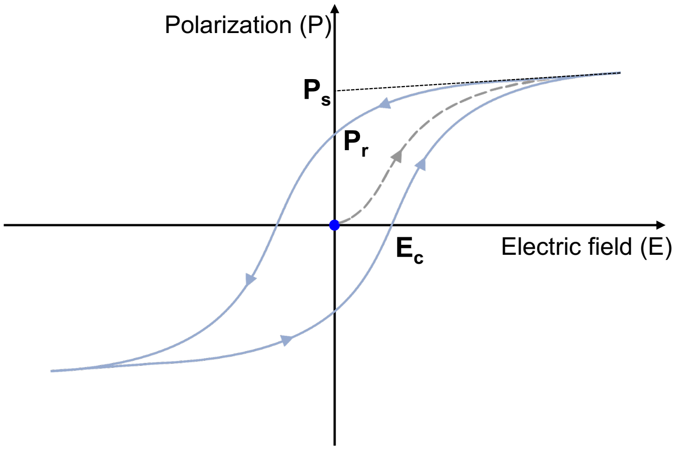

Figure 2-3: A typical ferroelectric hysteresis loop.

The dotted line illustrates the transition from an initial polydomain state with overall zero polarization towards a state with two distinct polarization states.

Typically, there are at least two possible polarization states. Therefore, there are regions of the material where the polarization is in one or the other of these states. These regions are called domains. When an electric field is applied, the polarization is forced to align with the field, resulting in the formation of new domains or a rearrangement of pre-existing domains. A domain wall separates two domains of different polarization.

The nature of the walls of ferroelectric domains partly explains the attraction of these materials. The wall dividing two domains extends over a very short distance, on the order of the lattice parameter. Such a wall width implies that many ferroelectric domains can be formed on a small area, which allows, by using the polarization direction as binary information, to design memories with high capacity.

The walls are also crucial in the distribution of the domains. The introduction of domain walls generally minimizes the system's total energy through a competition between the electric field energy density on the outside of the sample and the costs of domain wall formation, considering that domains reduce the electric field outside the sample [38].

2.1.2 Polarization switching

Examining the actual ferroelectric hysteresis cycle, as shown in Figure 2-3, it can be inferred that the polarization does not change instantaneously throughout the volume subjected to the electric field but through the formation of multiple domains that grow, eventually merging until the entire volume is reversed. The switching process takes place in three steps (Figure 2-4); heterogeneous nucleation of domains, fast vertical domain growth and relatively slow lateral growth of domains [39].

In the first step, the formation of a domain begins with the appearance of a domain seed (nuclei). This germination is done at the so-called nucleation sites. The surface, punctual or extended defects, the border of existing domains, or more generally, all inhomogeneities locally modulating the electric field are as many active centers decreasing the activation energy and can thus initiate the nucleation of a domain. After its formation (usually at the interface), the domain grows along the polar axis, propagating with the speed of an optical phonon. For a thin film with a thickness of 10 nm and a speed of sound of approximately 5000 m/s, this step therefore only takes a few picoseconds. The lateral extension of the domain, i.e., perpendicular to the polar axis, constitutes the third step. Lateral growth is much slower than vertical growth, which is understandable since the direction of extension is perpendicular to the applied field. Lateral growth has been observed via the different methods of the domain visualization [40].

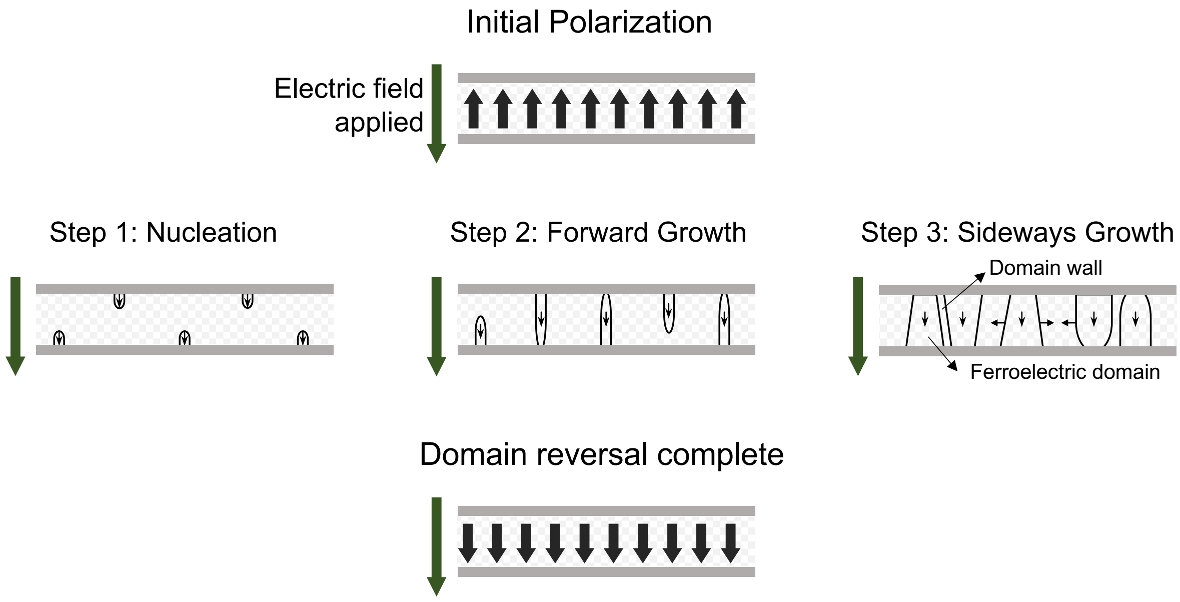

Figure 2-4: The three phases of domain reversal.

The three steps of the domain reversal process; are nucleation of domains, vertical domain growth and lateral growth of domains. Figure adapted from [39]

2.2 Ferroelectricity in $Hf_{0.5}Zr_{0.5}O_2$

The non-centrosymmetric orthorhombic phase (space group $Pca2_1$) has been extensively accepted to be responsible for the ferroelectricity in HfO_2-based thin films [22-24]. This is a metastable phase and, therefore, was not shown in the phase diagram of bulk HfO_2 [24, 41, 42]. The need for high-*k* materials to replace SiO_2 in the microelectronics scaling process triggered the exploration of HfO_2 at the nanoscale level [43]. In 2011 Böscke *et al.* first reported the presence of the metastable orthorhombic phase in Si-doped HfO_2 thin films [14]. This discovery had a direct impact, among others, in the field of ferroelectric memories, where the incompatibility of perovskite-based materials with CMOS was a major obstacle to their integration into CMOS electronics. HfO_2-based ferroelectrics are fully CMOS-compatible, with a high scalability [17]. Different mechanisms have been investigated to stabilize the orthorhombic phase, e.g. doping, strain, surface/interface/grain boundary energy, and oxygen vacancies.

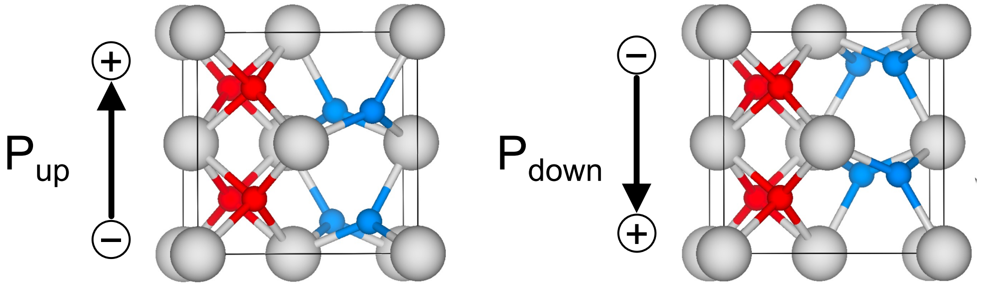

Figure 2-5: Ferroelectric orthorhombic phase (space group *Pca2₁*) for $Hf_{0.5}Zr_{0.5}O_2$

Atomic structures of ferroelectric orthorhombic phase in $Hf_{0.5}Zr_{0.5}O_2$ for the upward and downward polarization. The Hf/Zr atoms in gray and oxygen in red/blue where blue is the bistable oxygen. Figure adapted from [44].

2.2.1 Doping

Multiple dopants have been used to induce ferroelectricity in HfO_2 e.g. Si [14], Al [23], La [17], Y [45], Gd [46]. The HfO_2-ZrO_2 solid solution has attracted special attention as it exhibits a high remnant polarization for the composition 50-50 [41], low crystallization temperature, and similar atomic radii and crystal structures of Zr and Hf atoms.

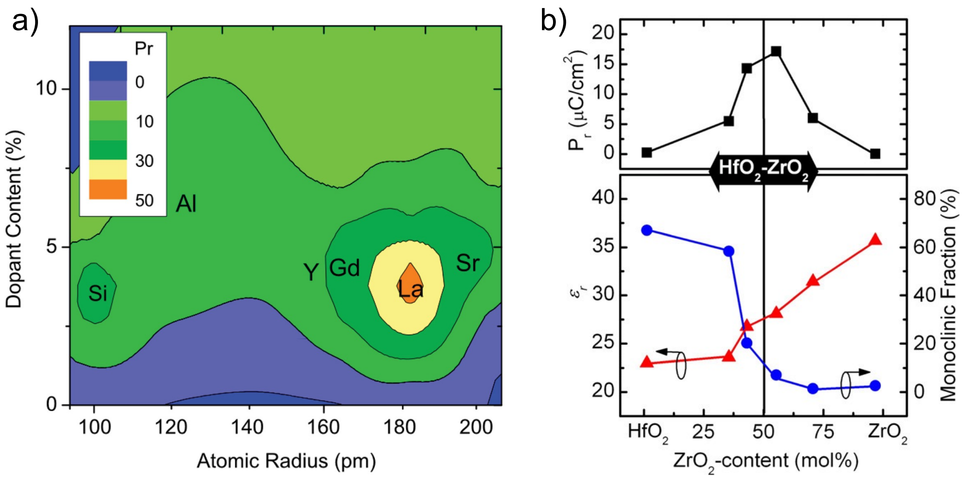

Figure 2-6: Remnant polarization in HfO_2 for different dopants.

a) Illustrate the numerical simulation of a contour plot of P_r values as a function of atomic radius and dopant content for different dopants [47]. b) Remnant polarization, dielectric constant, and monoclinic phase fraction in the HfO_2−ZrO_2 solid solution with respect to the mixing ratio of the oxides [41].

2.2.2 Stress and Strain

Stress/strain can induce distortions in the lattice parameter, leading to changes in material properties. As discussed in section 2.1, a rupture of the inversion symmetry is necessary for the piezo/ferroelectric effect. The role of strain in stabilizing the ferroelectric phase in hafnium oxide has been investigated theoretically [28] and experimentally [26, 48].

In epitaxial growth, the lattice mismatch between the substrate and the film can induce stresses in the thin film. The mismatch can be represented as the difference between the lattice parameters of the substrate and the layer as shown in the equation 2-1.

Equation 2-3: Mismatch film-substrate

$$\Delta = \frac{a_{substrate} - a_{film}}{a_{substrate}}$$

Where $a_{substrate}$ **is the substrate lattice parameter**
a_{film} **is the thin film lattice parameter**

For a mismatch Δ = 0, the growth is ideal, i.e., the compatibility between the layer and the substrate is perfect. Whereas for a mismatch Δ ≠ 0, the growth is accompanied by a lattice deformation at the interface to minimize the interface energy. In this case, growth is characterized by tension, tensile or compressive, depending on the sign of the mismatch between the substrate and the film. For a critical thickness, the elastic strain energy becomes very large, leading to the relaxation of epitaxial strain and the formation of dislocations. Since this kind of homogeneous strain engineering allows for a controlled deformation of the unit cell, it has been widely used to tune the ferroelectric properties of e.g. $BaTiO_3$ heteroepitaxial thin films [39, 49].

In the case of polycrystalline films, the formation of grains and grain boundaries are the sources of heterogeneous stress. The internal pressures of nanoparticles will depend on the radius (r) and the surface energy (γ); $P_{int} = {}^{2\gamma}/_{r}$. Accordingly, smaller grains produce higher inner stress. The thickness and thermal budget strongly influence grain size. Another source of stress is thermal expansion during heat treatments. The difference in thermal expansion coefficients between the film and the substrate can cause stress in the film. Different electrodes or electrodes/substrates have been extensively studied to control this stress in HfO_2-based films [26, 50, 51], with the TiN electrode being the most widely used [22]. A degradation/extinction of ferroelectricity is commonly observed with increasing HfO_2 layer thickness [52-54], also in agreement with computational investigations [28].

Strain plays a major role in the ferroelectricity in HfO_2. Most studies have been conducted on polycrystalline films in which multiple phases (m-, t- and o-phases) coexist [8]. The similarities between these phases and the small size of the crystallites make structural characterization complex. Therefore, increasing interest has been shown in well-oriented or epitaxial films to study the factors contributing to ferroelectricity in HfO_2 -based thin films [55-63].

However, it needs to be stated that the interfacial strain between substrate and thin film is only one parameter for a ferroelectric tunnel junction. While this strain has a possibly significant influence on the crystal structure and, therefore, on the existence and amplitude of the spontaneous polarization, the electronic structure (e.g. work function) of the electrode material also defines the nature of the contact for a resistive device. At least, there will be an impact of the electrode material on the Schottky barrier height, but the charge carrier density in different metals also accounts for a large range of screening depths. As we will see later, both barrier height and screening depth are dominant contributions to the conduction across a tunnel junction.

2.2.3 Oxygen vacancies

One of the most common defects in metal oxides is oxygen vacancies. These can form during deposition processes, doping, or operation, e.g., electrical cycling in resistive memories. Oxygen vacancies constitute a point defect and have a role in phase stabilization in HfO_2. In the phase diagram of HfO_{2-x} as a function of temperature and oxygen concentration proposed by Sharath *et-al.* [64], it is observed that a low oxygen concentration during deposition would tend to favour the tetragonal phase rather than the monoclinic phase. In work presented by Hoffmann *et al.* in 2015 [50], enhanced stabilization of the ferroelectric phase in TaN/Gd:HfO_2 films was observed, presumably due to an increased amount of oxygen vacancies. The authors confirmed this influence by *ab initio* simulations [50]. In sputter-deposited $Hf_{0.5}Zr_{0.5}O_2$ with varying O_2 partial pressure, Lee *et al.* [65] found an increase in ferroelectricity, reaching a remnant polarization of ~20 μC/cm^2 for 0% O_2 reactive gas. In 2019, Mittmann *et al.* [66] found that oxygen vacancies are a pathway to obtaining the ferroelectric phase in undoped HfO_2 by RF sputtering. The oxygen vacancies influence nucleation, which is correlated to grain size and thus surface/interphase energy, which influences subsequent phase transitions during annealing and cooling. A similar conclusion was recently reached by Materano *et al.* [30] when they studied the influence of oxygen content on orthorhombic phase evolution in $Hf_xZr_{1-x}O_2$ by atomic layer deposition (ALD) and physical vapor deposition (PVD) (Figure 2-7). Generally, while the qualitative effect has been established as indicated above, the quantitative assessment of oxygen vacancy concentrations in low relative and also low absolute concentrations due to the small sample volume of ultrathin ferroelectric films, is demanding and relies on additional assumptions as we shall see later.

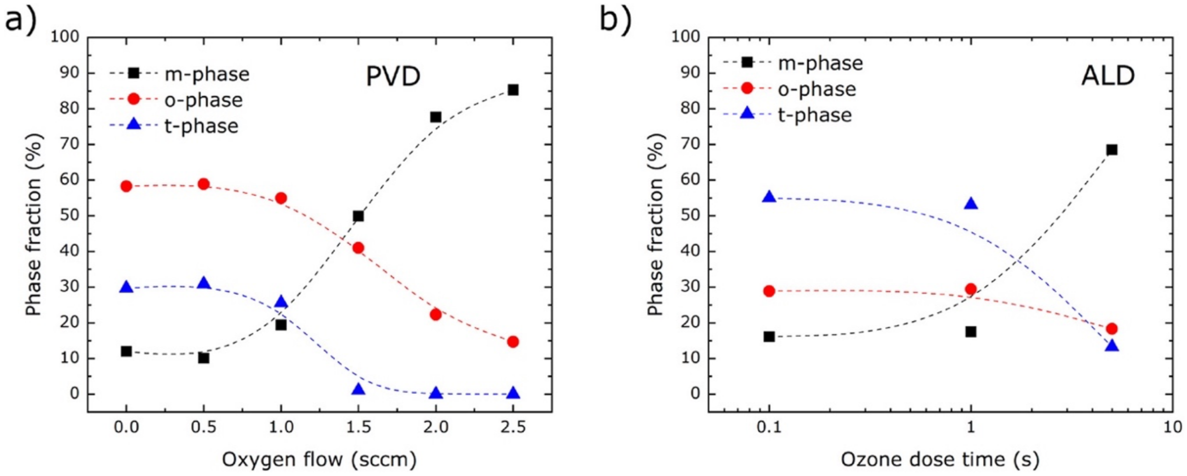

Figure 2-7: Phase fraction evolution of undoped hafnium oxide as a function of oxygen flow. Phase fraction evolution of undoped hafnium oxide layers as a function of the oxygen dose during deposition via a) PVD and b) ALD. From [30]

At this point, the author would like to emphasize that the influence of oxygen vacancies has been studied mainly to stabilize the orthorhombic nonpolar phase in doped and undoped HfO_2. In this context, it is however important to state that oxygen vacancies influence the leakage current of ferroelectric HfO_2 films [65, 67]. This is true regardless of whether the material is to be used as a capacitor or as a tunnel junction device but for the latter, the presence of oxygen vacancies will not only be a nuisance rather than a competing factor for the overall charge transport. At present, there is limited related work on the influence of oxygen during deposition on the electronic performance of HfO_2-based devices. An extensive discussion of the conduction mechanism(s) associated with oxygen vacancies is presented in Section 2.4.

2.3 Non-volatile memories

High-density storage has been developed in an array form (crossbar) since the 1960s. RAM (Random Access Memory) is typically used for data storage, while ROM (Read Only Memory) is reserved for instruction storage.

The RAMs can be divided into volatile RAMs, which must be refreshed every fraction of second and non-volatile memory, which have the advantage of preserving the information during a significant lapse of time (10 years or more) after powering off. Static and dynamic RAM (SRAM and DRAM) fall into the first category. However, DRAMs allow a higher storage density than SRAMs, which are faster to access. When it comes to assessing memory speed, it is worthwhile discriminating write- against read speed. Ideally, both of them should be fast.

The non-volatile memories (NVM), which appeared more recently, grouped different types of memory, as illustrated by the diagram below (Figure 2-8). Examples include Flash RAM and Ferroelectric memory (FeRAM). Memories whose information is stored in the form of resistance (ReRAM) include (in certain classifications) magnetic memories (MRAM), or metal oxide resistive memory (OxRAM), and especially memories whose resistance depends on polarization state (FTJ). However, this list is not exhaustive and gives only a glimpse of the many types of memories on which research is currently focused.

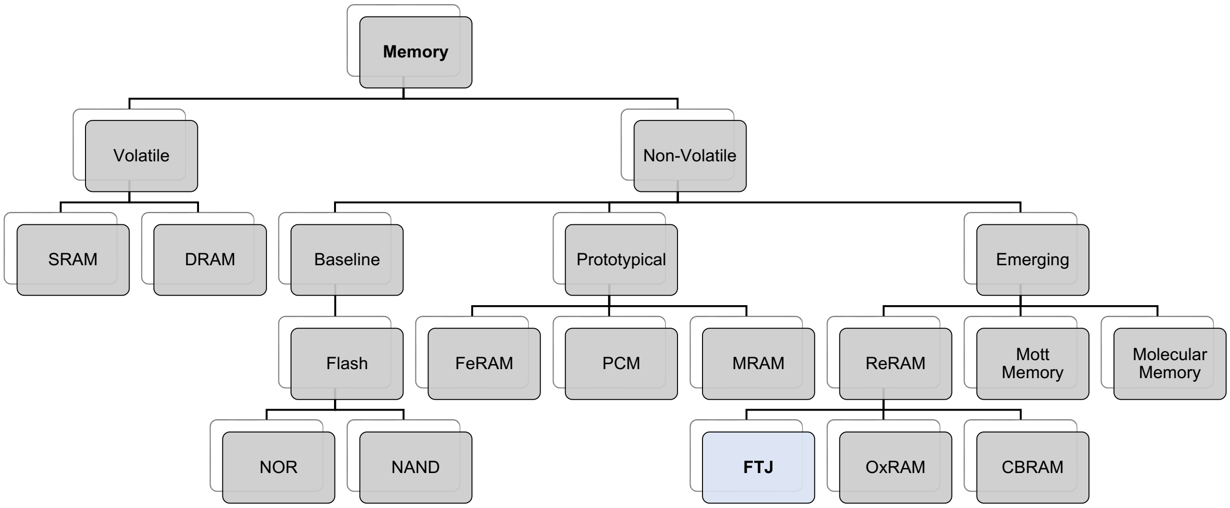

Figure 2-8: Memory classification, including volatile and non-volatile.

In terms of performance, the four most important parameters to consider are:

- The speed of writing/reading
- Endurance (the number of writes/erasures)
- Density (related to the minimum size of the cells)
- The energy required for writing.

To which then additional considerations add such as costs, scaling potential, compatibility with existing circuitry.

2.3.1 Resistive memories (ReRAM)

A resistive memory cell (ReRAM) is generally realized by a MIM structure (Metal/Insulator/Metal), with insulator material with mixed electronic/ionic conduction, significantly less conductive than the electrodes surrounding it, as illustrated in the diagram below. The reading operation will be performed by applying a voltage (usually < 1V) lower than the voltage values used for the writing operation (which modifies the state of the resistance of the "insulator" layer).

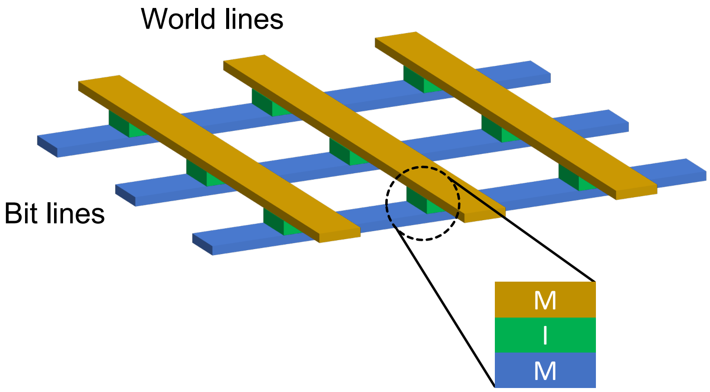

Figure 2-9: Simplified schematic of a MIM cell of ReRAM memory in a crossbar array. The insulator material is sandwiched between two electrodes.

The material resistance can be switched between at least two values: OFF (high resistive state) and ON (low resistive state). The transition between the states is usually differentiated between two types of switching: unipolar switching and bipolar switching [68]. Switching is called unipolar when the change from one state to the other (OFF → ON or ON → OFF) does not depend on the polarity of the writing voltage signal, as shown in Figure 2-10 (a). Switching is called bipolar when the OFF → ON transition occurs for one polarity of the voltage, and the ON → OFF transition occurs for polarity with the opposite sign (Figure 2-10 (b)).

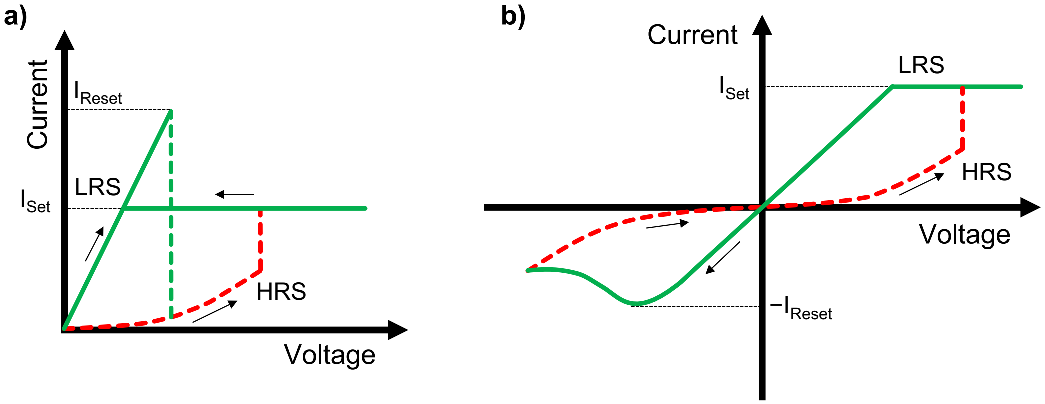

Figure 2-10: Classification of the switching characteristics from an I-V loop. Diagrams showing a) unipolar switching, b) bipolar switching. Adapted from [69].

A way to induce a breakdown in the insulation material is by creating a (semi-)conducting bridge or filament between the two electrodes on either side of the MIM structure. This type of resistive memory is known as a conductive bridge or electrochemical metallization cell (CBRAM). In these memories, a passive material is embedded between two metal electrodes. One of the two electrodes is electrochemically inert. The other electrode will be electrochemically oxidized under an appropriate positive bias voltage. The applied electric field will cause electromigration of the created cations to the inert cathode to form a conductive metal filament between the two electrodes, resulting in an abrupt change of the insulator conductivity, typically with a resistance change of up to 6 orders of magnitude. The effect is reversible for filaments of moderate size under reverse bias. A reversible change in conductivity can also be achieved by using transition metal oxides as an active layer without need for reactive electrodes in the so-called oxide resistive random-access memories (OxRAM) also known as valency change memory.

2.3.2 Oxygen vacancies in resistive switching

Like CBRAMs, OxRAMs operation is based on creating and destroying a filament. The main difference between these two types of memory is that contrary to CBRAMs whose filament nature comes from a diffusion of the metal ions of the active electrode, the filament of OxRAMs is created by the modification of the composition of the dielectric whose oxygen migrates or oxidizes under the effect of the bias. The result is the formation of a conduction filament composed of a sub-stoichiometric phase of the oxide or even a completely metallic [70]. This mode of operation explains the name given to these memories, OxRAM for Oxygen-based RAM or VCM for Valence Change Memories [71].

We can see an example of OxRAM memory in Figure 2-11, where the steps of formation and destruction of the filaments in the case of a bipolar component are schematized. In Figure 2-11 a), the initial component contains a large number of oxygen vacancies randomly distributed throughout the dielectric. In b), the forming step is shown. Applying a positive voltage on the top electrode (TE) causes the migration of the vacancies towards the bottom electrode (BE) until a filament gradually grows. When this filament reaches the upper electrode, the HRS state changes to LRS. In the case of a bipolar component, applying a voltage of reverse polarity in c) changes the direction of migration of the gaps until the filament breaks. A functional memory will switch from step b) to step c) during RESET and SET. The ratio of HRS to LRS states is generally inferior to that of CBRAM and is typically as large as two orders of magnitude.

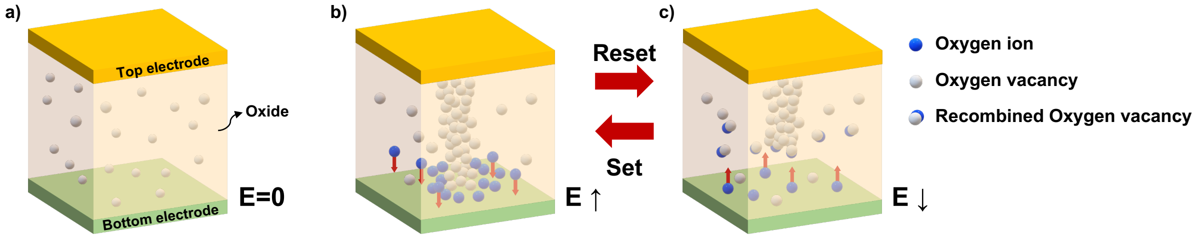

Figure 2-11: Schematic representation of the resistive switching process in a metal-oxide-metal structure.

a) The pristine state includes the oxygen vacancies randomly distributed throughout the dielectric. In b), the forming step (soft breakdown) is shown; a positive voltage on the top electrode causes the migration of the vacancies towards the bottom electrode until a filament gradually grows. Applying a voltage of reverse polarity in c) changes the direction of migration of the gaps until the filament breaks. A functional memory will switch from step b) to step c) during RESET and SET.

Other phenomena that do not involve filaments can cause resistive switching. A non-filamentary phenomenon of resistive switching related to anion migration can be observed. In this type of device, the resistance of the LRS and HRS states depends on the interface at the electrodes and the dielectric [69]. In an asymmetric structure, with one electrode in Ohmic contact with the dielectric (linear I(V) characteristic) and the second electrode in Schottky contact. The Schottky junction plays an essential role in this switching process as it is the one that limits the current flow. The application of a positive voltage on the electrode in Ohmic contact will cause the migration of oxygen vacancies within the dielectric and decrease the Schottky barrier. The overall resistance will then progressively decrease until an oxygen vacancy depletion zone is reached, synonymous with a minimal Schottky barrier and thus a low overall resistance, an LRS state. A reverse voltage will force the reverse migration of oxygen vacancies and, therefore, a return to the initial HRS state. This device is necessarily bipolar [71]. This effect may occur together with the formation of oxygen vacancy filaments.

The performance of these memories can be enhanced by modifying the materials of the MIM structure. As mentioned above, OxRAMs take advantage of vacancies in their dielectric. An increase in the presence of oxygen vacancies in these memories can be achieved by introducing a layer rich in oxygen vacancies, e.g., a substoichiometric titanium oxide [72] or an electrode with a high affinity for oxygen [73]. Oxygen vacancies can also be favoured during the deposition of the insulating layer [35]. This increase aims to promote the formation of a conductive filament inside the dielectric and, therefore, decrease the formation and switching voltages from HRS to LRS.

2.3.3 Ferroelectric memories

As mentioned above, ferroelectric materials exhibit a remnant polarization that can switch when exposed to an electric field. This quality can be used to store information by associating the remnant polarization states P_{r+} and P_{r-} to the logical states "0" and "1" of the binary coding. It was first reported in 1952 by Dudley Allen Buck in his master's thesis [74]. FeRAMs with high endurance and low energy consumption are currently commercially available [75]. FeRAMs use a 1T-1C (1 transistor - 1 capacitor) architecture similar to DRAMs but use a ferroelectric material instead of a dielectric (Figure 2-12). In a DRAM, when the transistor is in the ON state, the capacitor is charged, and when the transistor goes to the OFF state, the discharge of the capacitor generates a current that is returned to the overall system. Therefore, in the ON state, the polarization across the capacitor is induced and disappears in the OFF state. While in a FeRAM, replacing the capacitor with a ferroelectric capacitor will hold the polarization in the OFF state.

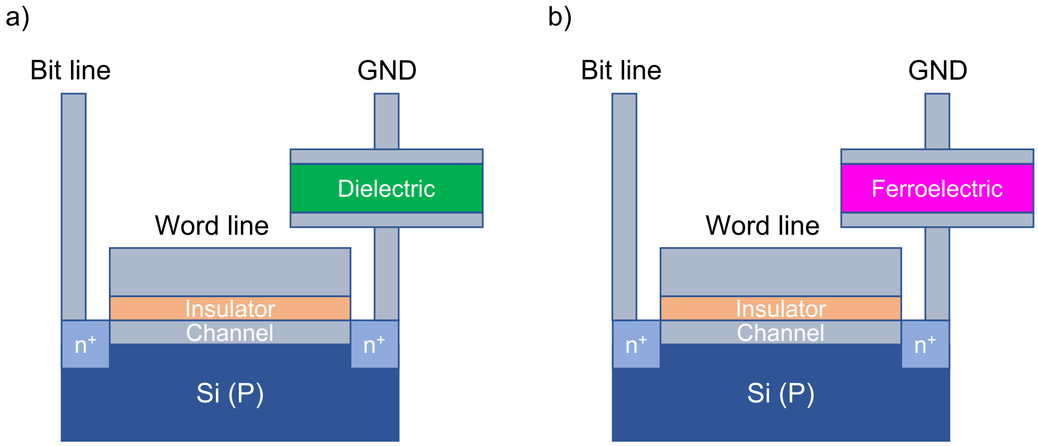

Figure 2-12: The architecture of a 1T-1C memories cells.

Comparison between a) DRAM and b) FRAM architecture.

In Figure 2-13 the hysteresis loop represents the electrical response of the ferroelectric material to the application of an external electric field. The direction of travel of this field allows for the writing and reading of binary data "1" or "0" in the form of two remnant polarization states. To write the logic state "0", regardless of the initial state of the ferroelectric material, it is sufficient to apply a positive electric field higher than the coercive field E_{c+}. After removing the applied electric field, the material spontaneously returns to the P_{r+} polarization state corresponding to the binary "0". According to the same principle, applying a negative electric field lower than the coercive field E_{c-} allows fixing the polarization in the negative remnant state and thus writing a "1".

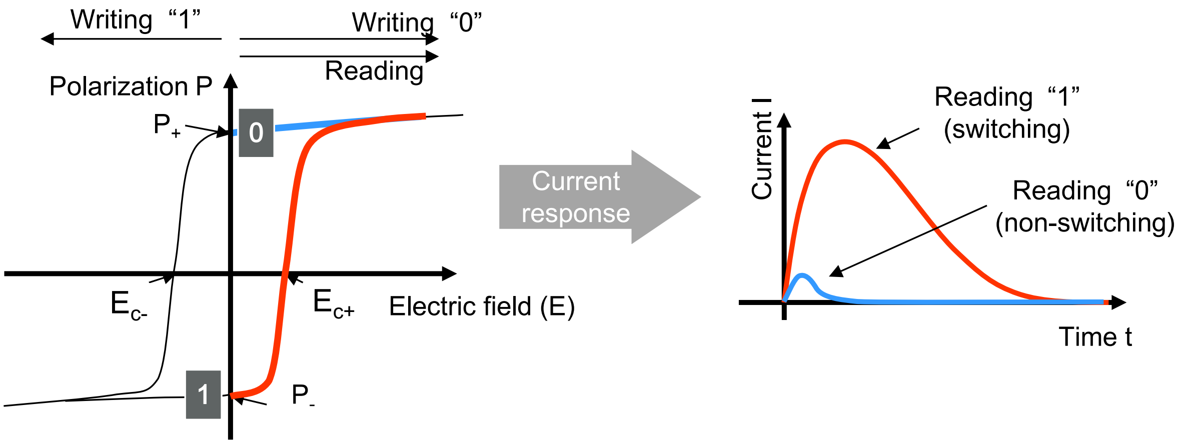

Figure 2-13: Process of writing and reading of a ferroelectric memory.

In the figure on the left, the hysteresis loop represents the polarization response of the ferroelectric material to the application of an external electric field. The direction of travel of this field allows the writing and reading of binary data "1" or "0" in the form of two remnant polarization states. On the right, the current response associated with the reading of binary data, in red for switching and blue for non-switching events. Adapted from ref [76].

Once this information has been written, it is necessary to be able to read it reliably and quickly. This step is carried out thanks to the application of an electric field higher than the coercive field E_{c+}, and this is whatever the initial logical state:

(i) If the stored information is a "0", the application of a positive voltage allows the bias to follow the blue curve in Figure 2-13. It is important to note that the sign of the polarization is not changed during the readout step: this is the "non-switching" polarization. The current generated by the charge flow associated with the non-switching polarization is represented in blue in the current response (Figure 2-13 right).

(ii) In the case where the stored information is a "1", the application of a voltage higher than the coercive voltage reverses the polarization state (according to the red curve in Figure 2-13). This reversal or "switching" of polarization is characterized by the appearance of a current represented in red in the current response (Figure 2-13 right). The "switching" current is higher than the "non-switching" current.

One particular strength of ferroelectric memories is an outstanding resistance to fatigue if the electrode material and the switching conditions are chosen appropriately.

The destructive readout is a notable limitation of FeRAM technology. Comparing the currents make it possible to distinguish the two polarization states initially written in the memory and thus read the information. After reading, the capacitor spontaneously returns to the P_{r+} polarization state, regardless of the information initially written. The latter is therefore lost and must be rewritten.

FeRAM technology, although very advantageous in terms of energy consumption and read/write speed, has several fundamental limitations. Two main limitations can be distinguished: extrinsic limitations due to the introduction of oxide materials in the manufacturing lines (contamination by oxides, etching steps). There are also intrinsic limitations to FeRAM technology linked to the ferroelectric character itself; One of the significant challenges to ensuring the development and sustainability of FeRAM technology is the ability to keep up with the constant miniaturization of the submicron silicon architecture. The chosen materials must continue to have a ferroelectric character at a low thickness and smaller area. The remnant polarization translates into a surface charge density (Gauss' law), so that for decreasing device area, the total amount of charges has already fallen below what is detectable via CMOS circuitry on board for current technology nodes. This is a fundamental limitation of all charge-based memory concepts including DRAM. There is a requirement to retrieve a minimum number of charges from the memory cell to amplify the signal in a CMOS circuit. Charge-based devices that are intrinsically limited by material parameters such as the remnant polarization, have therefore been discarded for further integration. To put these numbers into perspective, each unit cell of a ferroelectric in contact with the electrode will provide something of the order of 10% of an elementary charge to the surface charge density (100% being the ionization threshold).

The destructive reading imposing a rewriting of the information after reading constitutes the second intrinsic limitation of the technology. Additional circuitry is required for this purpose. To address these problems, a possible solution consists of designing an innovative memory architecture, presenting a non-destructive reading with extensive scalability. This is the case, for example, of the ferroelectric tunnel junction (FTJ) [5].

2.3.4 Ferroelectric tunnel junctions

A ferroelectric tunnel junction (FTJ) is a resistive random-access memory composed of an ultrathin ferroelectric (FE) layer sandwiched between two metal electrodes. It has therefore the conceptual potential to combine the excellent fatigue resistance of ferroelectric devices with the scaling and non-destructive read-out of resistive RAM. The concept of FTJ was first predicted in 1971 by Esaki *et al.* [77]. For decades, technological limitations and ferroelectric materials' difficulty scaling to a few nanometers delayed experimental FTJ validation. In 2003, Rodriguez *et al*. observed resistive switching in nanometric ferroelectric junctions, which could not directly relate to a polarization reversal of the ferroelectric layer [78]. In 2009, a group of authors established polarization reversal as responsible for resistive switching in FTJs [6, 7, 79]. The polarization direction of the FE layer can be switched between the top and bottom electrodes by an electric field across the stack. If the electrodes are asymmetric, it will produce a modulation of the barrier height, as shown in Figure 2-14. As a result, the tunneling current (resistance) through the stack is significantly altered.

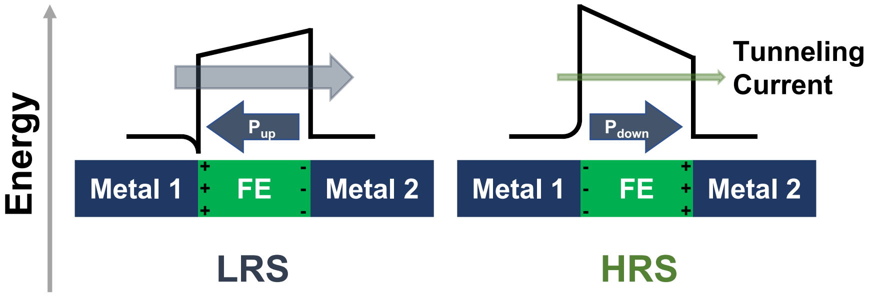

Figure 2-14: Band diagram of a Metal$_1$/FE/Metal$_2$ junction with different polarization directions.

In this schematic, the left electrode is sketched to contribute a certain amount of screening, while the right one is assumed to be ideal. TiN would be an appropriate example for the left and platinum for the right electrode.

It is called the tunneling electroresistance effect (TER), and is given by the equation 2-2.

Equation 2-4: Tunneling electroresistance effect.

$$TER = \frac{R_{HRS} - R_{LRS}}{R_{LRS}}$$

where R_{HRS} **is the high resistance and corresponds to the remnant polarization pointing to one electrode.**
R_{LRS} **is the low resistance and corresponds to the remnant polarization pointing to the other electrode.**

The writing process is achieved by applying an electric field higher than the coercive field that reverses the polarization. In contrast, the non-destructive readout is performed by sensing the tunnel current when a small potential is applied, preventing polarization reversal.

The first FTJs were based on materials such as $Pb(Zr_{0.2}Ti_{0.8})O_3$ (PZT) [79] or $BaTiO_3$ [6, 7]. These ferroelectric materials are members of the perovskite family. Although perovskites have been extensively studied, their integration with silicon electronics (CMOS technology) has faced some limitations. The first problem with these materials is the difficulty of integrating them directly onto silicon. It is often due to the chemical instability of the interface, which prevents the stabilization of the perovskite and the lattice mismatch that requires buffer layers such as $SrTiO_3$ [80]. The problem with using these buffer layers is that they increase the thickness of the capacitor stack. In addition, epitaxy of $SrTiO_3$ on Si requires temperatures above 900 ℃, well beyond the thermal budget of the CMOS industry. Another limitation of perovskites is the crystallization temperature. An annealing temperature of 450 ℃ is commonly accepted for back-end-of-line CMOS processes, where the thermal budget (a convolution of temperature and time) must not be exceeded to avoid interdiffusion of dopants from n- to p-doped regions and vice versa. However, a significant number of perovskite materials crystallize at temperatures exceeding 600 ℃ [81]. Finally, there are other problems with some of these materials, such as the presence of toxic lead in the PZT, the extraction of some perovskite is very polluting, or they are incompatible with the cross-contamination standards of clean rooms. These limitations of perovskites, combined with the technical requirements of FTJs themselves (ferroelectrics a few nanometers thick with low leakage current), limited the initial development of FTJs. In 2011, interest in FTJs was boosted by the breakthrough of a polar phase in Si-HfO_2 [14].

As discussed in section 2.2, HfO_2-based ferroelectrics have high scalability (up to a few nanometers) with substantial remnant polarization. In addition, it has the advantage of CMOS-compatibility, with HfO_2 presently used in the technological processes as a dielectric barrier in transistors.

As the name implies, tunneling is the primary mechanism in FTJs. However, parameters such as operating voltage or ferroelectric film thickness can differentiate the conduction mechanism in the FTJ device [82]. The following section discusses the most commonly encountered conduction mechanisms in metal-insulator-metal structures.

2.4 Conduction mechanism in metal-insulator-metal structures

Insulators are materials or devices which do not readily conduct electricity. Electrical conduction across a very thin metal-insulator-metal (MIM) interface, where the thickness is in the order of the extension of the electronic wavefunction is therefore a quantum phenomenon. The solution, for the simplest case, a quantum particle tunnel across a potential barrier, is discussed in numerous books on quantum mechanics. From the solution of the Schrödinger equation for this case, we know that the probability of the particle tunneling the barrier will depend on the barrier height or potential, the barrier width and the boundary conditions. It is important to remark that of these parameters, this probability is strongly affected by the width of the barrier in a non-linear way, exponential.

This section will discuss the most common conduction mechanisms in MIM-based resistive memories. These mechanisms are categorized into two groups: those that depend on the properties of the electrode-dielectric interface, e.g., Schottky emission; Fowler-Nordheim tunneling (FNT); and direct tunneling (DT) and those that depend solely on the properties of the dielectric, e.g., Poole-Frenkel emission (PFE); Ohmic conduction; space-charge-limited conduction (SCLC); and trap-assisted tunneling (TAT).

2.4.1 Schottky emission

Thermionic or Schottky injection describes the current due to charge carriers, which overcome the potential barrier at the electrode-oxide interface under sufficient thermal energy. A schematic representation of this mechanism is shown in Figure 2-15.

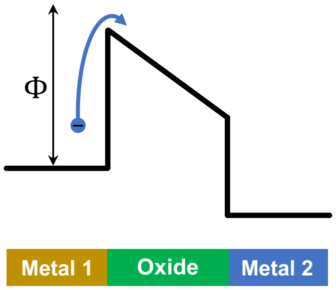

Figure 2-15: Schematic energy band diagram of Schottky emission in metal insulator metal interface.

The current density for Schottky emission is described by the equation 2-5 [83]:

Equation 2-5: Schottky emission.

$$J_s = AT^2 \exp - \left[\frac{\Phi}{k_B T} - \frac{1}{k_B T} \left(\frac{q^3 V}{4\pi\varepsilon_0 \, \varepsilon_r d} \right)^{1/2} \right]$$

where ***A*** **is the Richardson constant,**
Φ is the height of the Schottky barrier,
ε_r is the dielectric permittivity of the film, and
d **is the film thickness.**

2.4.2 Direct tunneling

Direct tunneling (DT) is the primary mechanism desired in a ferroelectric tunnel junction memory. Under this mechanism, the charge carriers will quantum-mechanically cross the potential barrier from one electrode to the other (imaginary solution of the Schrödinger equation).

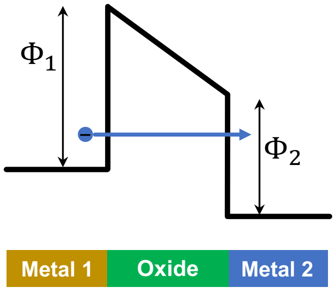

Figure 2-16: Schematic energy band diagram of direct tunneling in metal insulator metal interface.

The tunneling current can be based on the Wentzel-Kramers-Brillouin (WKB) approximation [84]. The analytical expression for the tunneling current density (J) is depicted in Equation 2-6 [7]. The WKB expression does not take into consideration screening effects or thermal expansion of the barrier.

Equation 2-6: Wentzel-Kramers-Brillouin (WKB) approximation.

$$J_{DT} = -\frac{4em^*}{9\pi^2\hbar^3}\frac{exp\left[\alpha\left\{\left(\Phi_2-\frac{eV}{2}\right)^{3/2}-\left(\Phi_1+\frac{eV}{2}\right)^{3/2}\right\}\right]}{\alpha^2\left[\sqrt{\Phi_2-\frac{eV}{2}}-\sqrt{\Phi_1+\frac{eV}{2}}\right]^2}\times\sinh\left[\frac{3eV}{4}\alpha\left\{\sqrt{\Phi_2-\frac{eV}{2}}-\sqrt{\Phi_1+\frac{eV}{2}}\right\}\right]$$

$$\alpha = \frac{4d\sqrt{2m^*}}{3\hbar(\Phi_1+eV-\Phi_2)}$$

Where **m^* is the effective electron mass,**
e is the electron charge,
$\hbar$ is the reduced Planck constant,
Φ_1 and Φ_2 are the potential barriers at the interface of the electrode and thin film,
V is the applied voltage and
d is thin film thickness.

All of the parameters in the above equation are either experimentally accessible or well documented for the respective materials.

2.4.3 Fowler-Nordheim tunneling

Figure 2-17 illustrates the Fowler-Nordheim tunneling (FNT) through a triangular-shaped potential barrier.

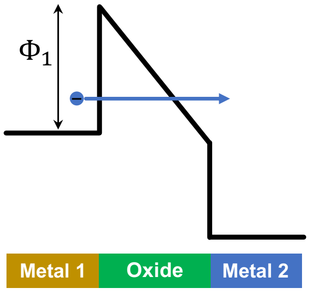

Figure 2-17: Schematic energy band diagram of Fowler-Nordheim tunneling in metal insulator metal interface.

This mechanism is typically associated with high voltage regimes, where the potential difference produces a band bending reaching a triangular-shaped potential barrier, in other words, the barrier width itself becomes a function of the electric bias, leading to a super-exponential dependence. The current density is given by Equation 2-7 [85].

Equation 2-7: Fowler-Nordheim tunneling.

$$J_{FNT} = \frac{(qE)^2}{8\pi h \Phi_B} exp\left[\frac{-8\pi\sqrt{2qm}}{3hE}{\Phi_B}^{3/2}\right]$$

Where q **is the electron charge,**
m **is the free electron mass,**
Φ_B **is the electrostatic potential barrier height,**
E **is the electric field across the barrier and**
h **is the Planck constant.**

2.4.4 Poole-Frenkel emission

The current density following the Poole-Frenkel emission (PFE) is expressed as equation 2-8 [86]. PFE refers to the release of charge carriers from trap states via a bias-induced reduction of the ionization potential of the respective defects, somewhat in analogy to Schottky barriers as shows in Figure 2-18.

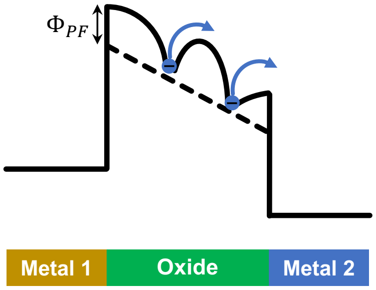

Figure 2-18: Schematic energy band diagram of Poole-Frenkel emission in metal insulator metal interface.

Equation 2-8: Poole-Frenkel emission.

$$J_{PFE} = \frac{q\mu n}{d} V\, exp\left[\frac{-q\left(\phi_{PF} - \sqrt{qV/\pi\varepsilon_0\varepsilon_r d}\right)}{k_B T}\right]$$

where ε_r **is the dielectric permittivity constant,**
$q\phi_{PF}$ **is the trap barrier height,**
μ **is the charge carrier mobility and**
n **is the concentration.**

2.4.5 Space-charge-limited conduction

Space-charge-limited conduction (SCLC) involves the injection of charge from a metal to a semiconductor or an insulator. The injected charge accumulates in traps inside the semiconductor, generating a space-charge region that prevents the injection of new charges. The current density for space-charge-limited conduction can be written as follows [87].

Equation 2-9: Space-charge-limited conduction.

$$J_{SCLC} = \frac{9\mu\varepsilon_0\,\varepsilon_r}{8}\frac{V^2}{d^3}$$

where μ **is the carrier mobility,**
ε_0 **is the vacuum permittivity,**
ε_r **is the dielectric permittivity, and**
d **is the film thickness.**

2.4.6 Trap-assisted tunneling

Trap-assisted tunneling (TAT) (also historically referred to as “hopping”) can be an elastic or inelastic process. The inelastic case involves the emission of phonons and is called phonon-assisted tunneling between traps. In contrast to direct tunneling mechanisms, which require relatively short lengths for tunneling to occur, the TAT mechanism can transport charge carriers over longer distances by tunneling between intermediate defects within the insulator (Figure 2-19).

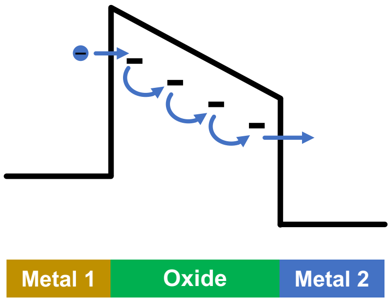

Figure 2-19: Schematic energy band diagram of trap-assisted tunneling in metal insulator metal interface.

The current density for the phonon-assisted tunneling is given by the equation 2-10 developed by Nasyrov and Gritsenko [88, 89].

Equation 2-10: Nasyrov–Gritsenko model for phonon-assisted tunneling (PAT) between traps.

$$J_{PAT} = \frac{e}{s^2}\frac{n_t}{N}\left(1 - \frac{n_t}{N}\right) v$$

$$v = \frac{2\sqrt{\pi}\hbar W_T}{m^* s^2 Q_0 \sqrt{kT}} \times exp\left(-\frac{W_{opt} - W_T}{2kT}\right) \times exp\left(-\frac{2s\sqrt{2m^* W_T}}{\hbar}\right) \times sinh\left(-\frac{eFs}{2kT}\right)$$

$$Q_0 = \sqrt{2\left(W_{opt} - W_T\right)}$$

where $\boldsymbol{s}$ **is the average distance between traps,**
$\boldsymbol{n_t/N}$ **represents the number of filled traps,**
$\boldsymbol{(1 - n_t/N)}$ **is the amount of empty trap,**
$\boldsymbol{W_T}$ **is the thermal energy of the trap,**
$\boldsymbol{W_{opt}}$ **is the optical energy of the trap,**
$\hbar$ **is the Planck constant,**
k is the Boltzmann constant,
$\boldsymbol{T}$ **is the temperature,**
$\boldsymbol{m^*}$ **is the effective mass of the electron and**
$\boldsymbol{F = V/d}$ **is the applied electric field.**

This transport mechanism provides an accurate description of current transport in both ferroelectrics and non-ferroelectrics $Hf_{0.5}Zr_{0.5}O_2$ [34, 90].

3 MATERIALS AND METHODS

In the first section of this chapter, we intend to explain in detail the principle of sputtering, particularly radiofrequency (RF)-magnetron sputtering. The TiN/$Hf_{0.5}Zr_{0.5}O_2$/Au structures used in this thesis were produced by RF-magnetron sputtering. On one hand, this technique allows for the production of thin film stacks of controlled thickness; on the other hand, it is perfectly scalable to industrial processes. Moreover, the modulation of the process parameters allows for maximum adjustment of the properties of the materials composing the future memory cell. The growth of the memory structures cannot be separated from an intensive characterization of these materials in order to optimize their properties. Among the characteristics measured are the thickness of the layers, their surface roughness, their crystalline structure and chemical properties, and an extensive electrical characterization. The second section of this chapter aims at describing some of the techniques used and at demonstrating their importance for the development of a MIM structure.

3.1 Growth of thin films

The devices analyzed in this study consist of a three-layer stack: bottom electrode (TiN), active layer or oxide layer ($Hf_{0.5}Zr_{0.5}O_2$) and Au as the top electrode. Each of these layers was deposited sequentially using RF-magnetron sputtering. This section will describe this deposition technique, which belongs to the physical vapour deposition technique family and describe the equipment used in this investigation. Given the polycrystalline nature of the relatively thick bottom TiN electrode, the substrate is of little importance. We use Si wafers with a native oxide on top.

3.1.1 Radiofrequency (RF)-magnetron sputtering

Within the most common techniques used to deposit thin films are the physical vapour deposition (PVD) methods. These methods are characterized by the physical generation of vapour of ions or atoms from the source material, usually known as a target, and then deposited on the surface of the substrate. The way in which this vapour is generated differentiates the PVD methods.

Principles

One of the PVD methods is sputtering. In the sputtering process, a solid surface (target) is bombarded with energized particles (in our case mainly accelerated argon gas ions or an oxygen-argon mixture for the film and nitrogen for the bottom electrode). The collisions affect the target's surface, causing the ejection of target atoms by momentum transfer which then deposit on the substrate (Figure 3-1). This deposition technique is widely used in academia and large-scale production. As an additional process parameter, the substrate temperature is often adjustable.

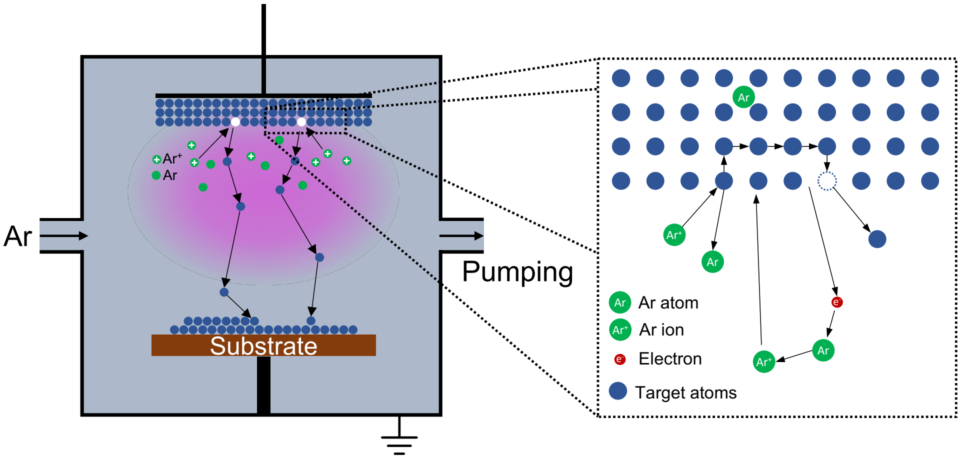

Figure 3-1: Diagram of the principle of sputtering.

Sputtering involves generating a plasma composed mainly of ions that will sputter the target and extract atoms from it. The atoms and ions created will then be deposited on the substrate.

RF-sputtering

The plasma formation can be triggered by a direct current (DC) or radiofrequency (RF) power supply in sputtering. DC sputtering works very well for conductive materials. While for insulating materials, DC polarization causes charge accumulation on the target surface. This charge accumulation during ion bombardment is a source of deposition heterogeneity and plasma instability [91]. Whereas, in the case of radiofrequency (RF) sputtering, deposition of conductive, insulating or semiconducting materials can be achieved. In contrast to DC systems, RF systems require an impedance matching network between the power supply and the sputtering chamber. Frequencies above about 1 MHz are sufficient to produce an almost continuous discharge of the insulator [92], with 13.56 MHz the most widely used frequency for the RF source [91].

Magnetron sputtering

The magnetron target has the effect of increasing the deposition rate. Its role is to confine the secondary electrons, emitted under the effect of the impact of the ions, close to the target to increase the ionic density of the plasma zone. This technique differs from the previous ones by the presence of a magnetic field perpendicular to the electric field created by the cathode, i.e., parallel to the target. This magnetic field is created by permanent magnets located in the target holder. The electron trajectories wrap around the field lines, thus increasing the probability of shock ionization. Thus, a large quantity of Ar^+ ions will be attracted to the target, and as an ion constantly expels, on average, the same number of atoms from the target, the sputtering effect will be more critical. This results in deposition rates about fifty times higher than those observed in the absence of magnetron.

The advantage of this technique is also to operate at lower gas pressures which increases the mean free path of the particles. Generally, the momentum transfer between the process gas and the target yields particle energies of several electron volts equivalent to tens of thousands of Kelvin of thermal energy. This energy is reduced prior to deposition on the substrate via multiple consecutive collisions in the plasma, so that the atoms/ions impinging on the substrate can be considered as thermalized.

Reactive sputtering

In the case where, for example, one of the elements constituting the target is volatile, it can be carried away during the pumping, and the recombination of the ejected atoms does not give the original material. It is then necessary to use a reactive gas during sputtering (oxygen in the case of oxides, nitrogen in the case of nitrites or hydrogen sulphide in the case of sulphides) in order to prevent the thin film from being deficient in this element. The role of the reactive gas is threefold:

- to restore the surface stoichiometry of the target.
- to promote the recombination of ions, atoms and molecules during the target-substrate transfer.
- to restore the composition of the thin layer or to modify it with respect to the target material.

3.1.2 Sputtering unit SPT310-TT

An SPT310-TT RF-Magnetron Sputtering unit from Plasmionique Inc. was used for this thesis. This sputtering is equipped with three sputtering magnetrons at an angle to allow co-deposition. It also has a heating system with a proportional–integral–derivative (PID) controller that allows depositions temperatures up to 800 °C (tungsten filament). Two mass flow controllers, Ar 20sccm and O_2 10sccm, allow the control of the partial pressure of the two gases. The configuration is on-axis with a distance of approximately 110 mm between target and substrate. As the deposition rate falls quadratically with the distance between target and substrate, this relatively large distance provides low deposition rates and an excellent control of thin films thicknesses.

3.2 Characterization techniques

The synthesis of materials by RF-Magnetron Sputtering cannot be isolated from an intensive characterization of these materials in order to optimize their properties. Among the measured characteristics are the thickness of the layers, their surface roughness, their crystalline structure, and their electrical properties.

3.2.1 X-Ray Diffraction

X-rays of approximately 0.1 nm wavelength have the particularity of penetrating deep into the material and of elastically interacting with the electrons that compose it without modifying the material's properties. Since the wavelength of the x-ray is of the same order of magnitude as the interatomic distance, the ray will be diffracted elastically at an angle defined by Bragg's law:

Equation 3-1: Bragg's law.

$$n\lambda = 2d_{hkl}\sin\theta_{hkl}$$

where $\boldsymbol{\lambda}$ **is the incident beam wavelength in Å,**
$\boldsymbol{d_{hkl}}$ **is the lattice distance between the parallel planes** $\boldsymbol{hkl}$**, and**
$\boldsymbol{\theta_{hkl}}$ **is the diffraction angle.**

The techniques that use X-rays are non-destructive and provide information on the structure of thin films and the properties of the materials that compose them.

This part deals with two methods used during this thesis to characterize the layers obtained by RF-magnetron sputtering: X-ray reflectivity (XRR) and grazing incidence X-ray diffraction (GIXRD). X-ray reflectivity allows us to quantitatively determine a material's electron density profile. We can extract information on the density, the thickness of the layers, as well as the roughness of these or at the interface between several layers.

The X-ray diffraction in grazing incidence brings information on the crystal structure of materials and allows for the identification of the atomic arrangement. We will only develop the essential principle of this technique.

3.2.2 Grazing incidence X-ray diffraction

In the case of thin films where the thickness to be analyzed is very small, X-ray diffraction in grazing incidence (GIXRD) is more appropriate than the Bragg-Brentano configuration. Indeed, the diffracting volume is more important. In addition, the smaller the angle of incidence, the smaller the penetration depth, so the information obtained on the diffractograms will be more about the film than its substrate.

This angle, which we will note Ω, was set to 1° for the GIXRD measurements performed during this thesis. The detector moves in the plane of incidence and recovers the diffracted signal as a function of the angle 2θ it forms with the sample surface (Figure 3-2).

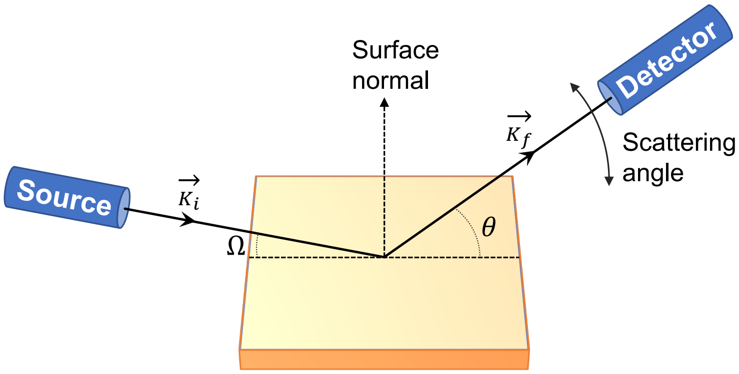

Figure 3-2: Schematic illustration of Grazing Incidence X-ray Diffraction. $\overrightarrow{K_i}$ and $\overrightarrow{K_j}$ are the respective wave vectors of the incident and diffracted wave.

A GIXRD measurement produces a spectrum showing the intensity of the diffracted signal as a function of the angle θ between the detector and the surface. When the incident beam is diffracted by an hkl plane, a peak of given intensity is observed at the position θ_{hkl} defined by Bragg's law. The peak's position, intensity, and shape are characteristic of the material studied.

3.2.3 X-ray reflectivity

X-ray reflectivity is a method that allows measurements of the thickness of crystalline or amorphous layers (up to a few Å in principle). It also permits obtaining a density profile as well as the roughness of the surface and the interfaces. XRR is based on measuring the scattering of X-rays from the material in specular reflection. The incident X-ray forms an angle θ with the sample surface, and a detector is placed symmetrically to collect the beam reflected from the surface ($\theta - 2\theta$ configuration). We progressively increase the value of the angle of incidence, and we measure the intensity of the reflected beam. The measured intensity of the reflected beam depends on the material's electron density: the electrons in the layer subjected to X-rays oscillate, then emit spherical waves which propagate isotropically in space and interfere with each other. The angle of incidence θ is such that the reflection of the X-ray source by the sample is total, denoted by critical angle θ_c. For $\theta > \theta_c$, a portion of the beam penetrates the sample and the intensity of the reflection decreases. Since the optical index is close to 1 for XRR during the decrease, we obtain interference called Kiessig fringes. Its interference is directly related to thickness, density and roughness and is independent of the nature of the material, unlike other methods such as ellipsometry.

A spectrum showing the beam's intensity reflected by the sample as a function of the angle of incidence $\theta(2\theta)$ is returned from the XRR analysis of a thin film deposited on a substrate.

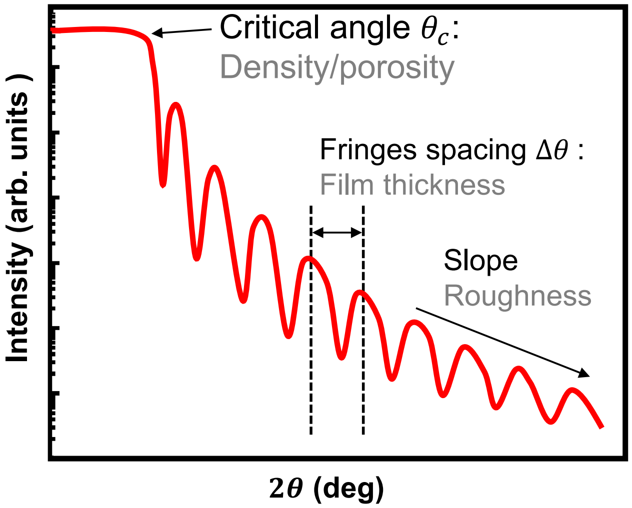

Figure 3-3: Schematic diagram of an XRR pattern.

The intensity scale is logarithmic.

The critical angle θ_c corresponds on the spectrum to the angle of incidence of the X-ray from which we observe a decrease of the detected intensity. Beyond this angle, the ray is also transmitted in the thin layer, and the reflection is not total anymore. Its value allows us to determine the mass density of the material ρ by the formula [93]:

$$\cos\theta_c = 1 - \frac{r_e}{2\pi}\lambda^2\rho$$

The interaction of the waves reflected at the surface and the different interfaces result in the appearance of Kiessig interference fringes. The period of these interferences allows us to determine the thickness of the thin layer(s) analyzed:

$$\Delta\theta = \frac{\lambda}{2d}$$

For large angles of incidence (right side of the spectrum), a significant portion of the incident beam is transmitted into the layer and thus reflected at the interfaces. The transmitted ray is less well-reflected when the layer presents a variation of its electrochemical density, such as a large interface roughness. This is reflected on the spectrum by a significant decrease in the amplitude of the fringes for large values of θ.

A marked decrease above the critical angle means that the surface is less effective in reflecting the incident beam and may reflect a significant surface roughness.

3.2.4 PANalytical X'Pert Pro

The equipment used during this thesis, for both reflectivity and diffraction measurements, is the X'PERT PRO from PANalytical. The X-ray source is from the copper Kα line ($\lambda_{CuK\alpha} = 1.5418\ \text{Å}$).

In the case of an XRR measurement, we add a 1/2° slit after the source and a 0.18 mm slit before the detector.

For GIXRD measurement, we add only a 1/8° slit at the source.

3.2.5 Atomic Force Microscopy

The invention of atomic force microscopy (AFM) in 1986 [94] revolutionized nanotechnology, as it has become a widely used technique for studying and exploring the topography, morphology, force measurement, and manipulation of physical and chemical surface properties of crystalline, semi-crystalline or amorphous samples in a vacuum, air and even in liquid media [95].

The first mode of operation invented was the contact mode. Its operating principle is briefly described below.

A tip with a small radius of curvature and mounted on a flexible cantilever is brought in contact with a surface where the contact force causes the cantilever to bend. An optical system consisting of a laser-focused on the end of the cantilever and a four-quadrant photodiode measures the position of the laser reflection. From this position, the cantilever's curvature and, therefore, the surface's height in contact is deduced. By scanning the surface tip, the sample's topography variation can be measured via the cantilever's curvature (or deflection) due to the laser reflection. By adding a piezoelectric system to control the height of the tip or the sample, and a feedback loop on the signal of the four-quadrant detector, it is possible to follow the variation of the height of the sample by keeping the tip/surface force constant (Figure 3-4).

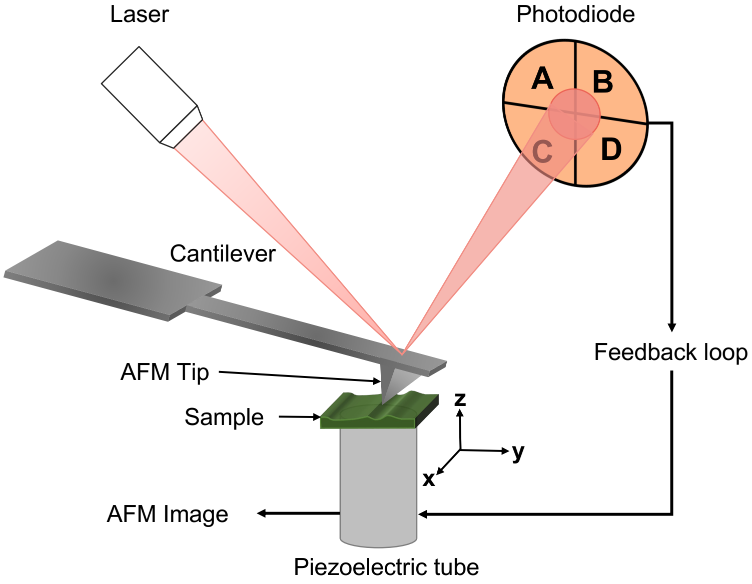

Figure 3-4: Principle of operation of the AFM.

A laser beam detects the cantilever's movements, which reflects it towards a photodiode. A feedback loop maintains the vertical position of the cantilever constant by acting on the piezoelectric cylinder whose voltage variations are used to construct the images.

This first contact mode was followed by so-called "dynamic" modes, which the first proposed by Martin *et al*. in 1987 [96]. This so-called intermittent-contact mode, also known as tapping mode or amplitude modulation, was followed by a second one invented by Albrecht in 1991 [97] called non-contact mode (or frequency modulation). These modes work as described below.

A piezoelectric system is used to vibrate the cantilever at a frequency close to the resonant frequency. Near the surface, the interaction varies the amplitude or phase of the oscillation. By feeding these parameters back to the sample scanner piezoelectric, as in the case of contact mode deflection feedback, measurement of the sample surface topography is achieved.

Interaction forces

The interaction potential U is obtained by adding all the attractive and repulsive contributions. Mie gives its general form as a function of the interaction distance r:

Equation 3-2: Mie potential.

$$U(r) = -\frac{A}{r^n} + \frac{B}{r^m}$$

where *n* and *m* are two integers where the first term represents the attractive part of the interaction, while the second corresponds to its repulsive contribution.

The best-known form of the Mie potential is the Lennard-Jones potential which is written:

Equation 3-3: Lennard-Jones potential.

$$U(r) = 3\varepsilon\left(-\left(\frac{\xi_0}{r}\right)^{12} + \left(\frac{\xi_0}{r}\right)^{6}\right)$$

where ξ_0 is the interatomic equilibrium distance.

When the tip is a few angstroms away from the surface, a repulsive force is created by the Coulomb repulsion and the interpenetration of the electronic orbitals. This interaction has a very short range (a few angstroms at most). Indeed, the Pauli exclusion principle forbids the presence, at the same place, of two electrons in the same quantum state, which would not fail to happen if the tip approaches too close to the surface.

The attractive forces are mainly the van der Waals forces. There are three contributions to van der Waals forces. The first is the polarization due to certain atoms or molecules possessing a permanent multipole moment. They can also create moments in non-polar molecules, which is the second contribution to the van der Waals potential. Finally, the third contribution is called dispersion and corresponds to the instantaneous polarization created by fluctuations in the position of the atoms around the nucleus.

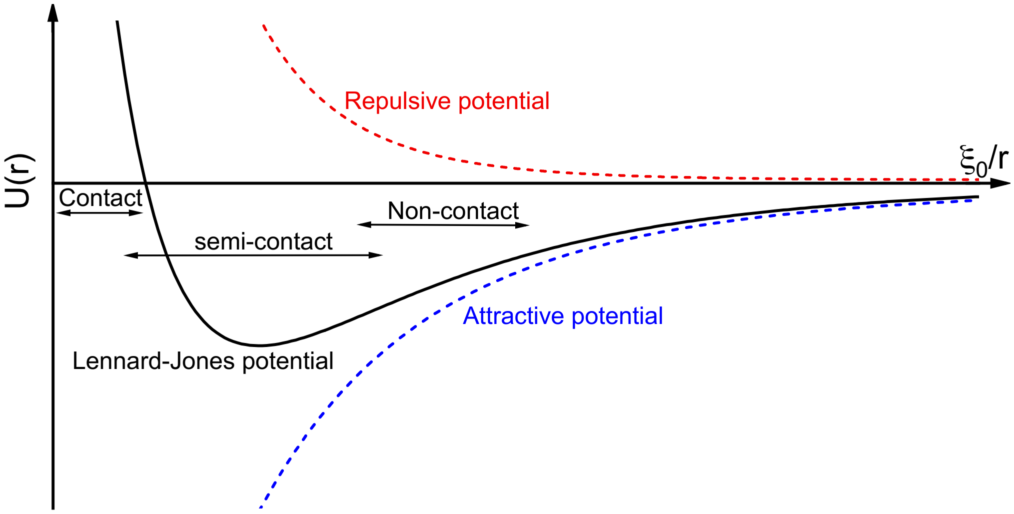

Figure 3-5: Representation of the Lennard-Jones potential.

The AFM can be used with a repulsive regime (contact mode), an attractive regime (non-contact mode), as well as a combination of both (intermittent or tapping mode).

The van der Waals forces are also very short range, usually decaying within a few nanometers. The nature of the interaction also sets the lowest limit to the spatial resolution, the shorter the interaction range, the better the resolution. Often, other limiting factors such as noise or tip-radius will impose restrictions well above this range.

3.2.6 SmartSPM1000

In this thesis, we used a SmartSPM1000 atomic force microscope from AIST-NT Inc to investigate the surface morphology of the synthesized thin films. The AFM was operated in semi-contact mode with a line scan frequency of 0.5 Hz using MikroMash AFM probes (Si) with; a tip radius of ~8 nm with a nominal resonance frequency of 325 kHz and a nominal spring constant of 40 N/m.

3.2.7 Electrical Characterizations

A Keysight B2901A Source/Measurement Unit (SMU) was used for the electrical characterization of the TiN/$Hf_{0.5}Zr_{0.5}O_2$/Au devices. The electrical connection with the memory cells was carried out utilizing tungsten probes (with a tip radius of 12 µm) coupled with two micromanipulators (Figure 3-6). The probe station is shielded in a Faraday cage.

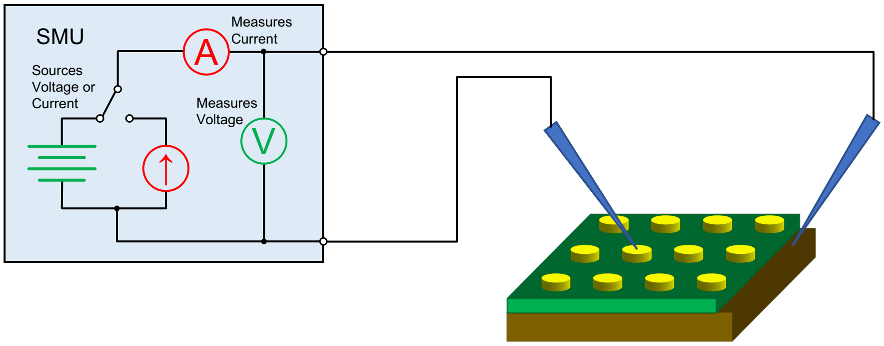

Figure 3-6: Schematic of the I-V probe station.

This experimental setup performed quasi-static voltage sweep characterization, response to pulse excitation, and memory cell retention and endurance tests.

3.2.8 Quasi-static voltage sweep

The measurement of the currents is done using the Keysight B2901A SMU. It provides a quasi-static voltage like the one shown in Figure 3-7(a). The current measurement is recorded after applying a voltage. A typical curve of the I(V) measurement is given in Figure 3-7(b).

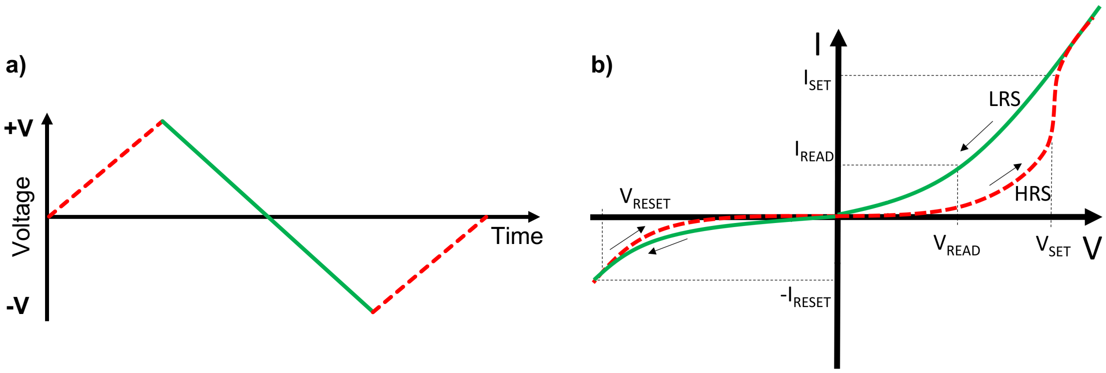

Figure 3-7: Current-voltage measurement.

a) The shape of the voltage waveform used during an I(V) loop measurement. b) A typical I(V) curve for an FTJ device. Adapted from [69].

From these curves, by comparison with the previously discussed models of charge transport, it is, in principle, possible to trace the nature of the conduction mechanism.

3.2.9 Endurance tests

Under device operation, the cell will not undergo quasi-static voltage sweeps, they are slow and impose an undue electrical strain on the device that will accelerate aging/fatigue. Under real conditions, the sample will be repeatedly subjected to voltage pulse, and different mechanisms will cause it to break down over time. Therefore, it is necessary to perform endurance tests to know after how many cycles the sample will typically break down. The sample is generally subjected to two distinct sequences: a "cycling" sequence and a "measurement" sequence. The sequence used in this work is shown in Figure 3-8, which combines writing and reading sequences.

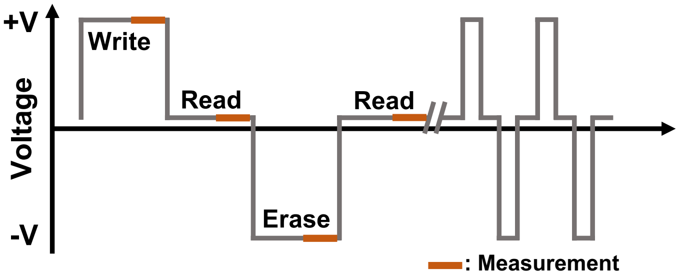

Figure 3-8: Pulse sequence applied for the fatigue tests.

The sequence represents a write pulse, followed by a read pulse, an erase pulse and a second read pulse. The red segment at the plateau of each pulse represents the measurement window.

3.2.10 Retention tests

Very few memories will store information for an indefinite duration, even though non-volatile devices are by definition conceived to do so. When the sample is no longer subjected to any voltage, a loss of polarization in the case of FTJ, filament diffusion in the case of CBRAM, or oxygen vacancy migration in the case of OxRAM may occur over time. The samples eventually lose their initial state. Retention tests consist in measuring I(V_{read}) over different time intervals. These intervals can be spaced at regular or logarithmic intervals. Between each measurement, no external field is applied. A voltage-time dilemma occurs when the read voltage needs to be chosen close to the write voltage so that consecutive reading may over time alter the memory state due to cumulative effects of consecutive reading processes.

3.2.11 Van der Pauw resistivity measurement

The van der Pauw Method is a technique widely used to measure the resistivity of materials in the form of thin films. This method operates in a four-probe mode and can be used in any arbitrary shape with a flat shape of uniform thickness, no isolated holes, and the four contacts must be located at the edges of the sample.

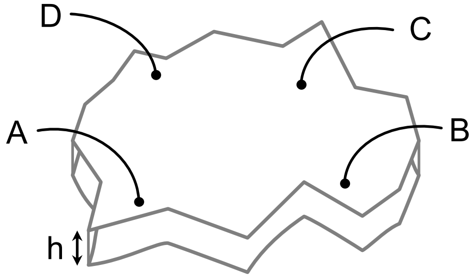

Figure 3-9: Van der Pauw method for the determination of resistivity.

In Van der Pauw the resistivity is gives the equation [98]:

Equation 3-4: Van der Pauw resistivity.

$$\rho = \frac{\pi h}{\ln(2)} \frac{\left(R_{AB,CD} + R_{BC,DA}\right)}{2} f\left(\frac{R_{AB,CD}}{R_{BC,DA}}\right)$$

Were *h* is the sample thickness and f is found from the relation:

$$\frac{R_{AB,CD} - R_{BC,DA}}{R_{AB,CD} + R_{BC,DA}} = f \operatorname{arcosh}\left[\frac{1}{2} e^{\ln(2)/f}\right]$$

For ${}^{R_{AB,CD}}\!/\!_{R_{BC,DA}} \approx 1$, f can be approximate by:

$$f = 1 - \left(\frac{R_{AB,CD} - R_{BC,DA}}{R_{AB,CD} + R_{BC,DA}}\right)^2 \frac{\ln 2}{2} - \left(\frac{R_{AB,CD} - R_{BC,DA}}{R_{AB,CD} + R_{BC,DA}}\right)^4 \left(\frac{(\ln 2)^2}{4} - \frac{(\ln 2)^3}{12}\right)$$

4 RESULTS AND DISCUSSION

This chapter presents a characterization of the TiN bottom electrode, the $Hf_{0.5}Zr_{0.5}O_2$ ferroelectric film and a study on the influence of oxygen partial pressure on the electrical conduction through $Hf_{0.5}Zr_{0.5}O_2$ films. In section 4.1, the influence on the roughness and conductivity of TiN films deposited by sputtering from different targets and annealing methods is investigated. We discuss the effects of two annealing methods, in-situ annealing and rapid thermal annealing (RTA), and the influence of oxygen partial pressure on the formation of the ferroelectric orthorhombic phase. Section 4.2 covers the discussion of two conduction mechanisms: Direct tunneling and trap-assisted tunneling. These mechanisms are mainly determined by the film thickness and the average distance between traps. The operation and performance of a resistive switching device based on oxygen vacancy filaments in $Hf_{0.5}Zr_{0.5}O_2$ are presented in section 4.3. The presence of a high number of oxygen vacancies was intentionally induced by the reduced oxygen partial pressure during sputter deposition.

4.1 The structure TiN/$Hf_{0.5}Zr_{0.5}O_2$/Au

A ferroelectric tunnel junction is not just about the ferroelectric, its operation relies on the stack of different materials in the metal-insulator-metal structure and the way they are structurally, chemically and electronically interfacing. While the structural aspect via epitaxy is not addressed in this work (see discussion above), the chemical stability of $Hf_{0.5}Zr_{0.5}O_2$ with respect to the diffusion of oxygen is exceptionally good, far better than that of perovskites. However, different electrode materials have different affinity to react with oxygen and while e.g. gold can be considered inert, we shall see that TiN has a tendency to form oxynitrides. So, the main focus of this chapter is on the nature of the electrical interface that is primarily determined by the work function of the metal and the electron affinity of the semiconductor/insulator. For all these reasons and keeping in mind CMOS compatibility, an appropriate selection of materials must be made during the conception of an FTJ since the intrinsic properties of each one of them, and the interfaces between the constituent materials will ultimately determine the device function as a whole. Asymmetric (nominally or unintentionally) electrodes with high work functions are desired to maximize the TER effect. On the other hand, stabilizing the orthorhombic phase in the $Hf_{0.5}Zr_{0.5}O_2$ can be a complex process favoured with a proper lattice mismatch between the bottom electrode and the $Hf_{0.5}Zr_{0.5}O_2$ layer. In this study, we use nominal TiN as a bottom electrode which has shown promising results in favouring the non-centrosymmetric phase in $Hf_{0.5}Zr_{0.5}O_2$-based devices [22].

4.1.1 TiN characterization

In FTJ memories, the tunnel current is limited by, among other factors, the thickness of the ferroelectric film and the roughness at the interface with the electrodes [5, 99]. The calculation of Dörfler *et al*. indicates that roughness of a fraction of nanometers leads to the rapid extinction of the TERS effect [99]. Therefore, it is crucial to produce smooth electrodes. On the other hand, a small roughness will favor the nucleation of domains and, therefore, the polarization switching.

Two methods of TiN deposition were employed: reactive sputtering from a Ti metal target and direct sputtering from a TiN ceramic target. While they should both yield the same result, the following experiments were conducted to understand the effect of the sputtering chamber that we used for the production: The sputtering chamber is designed for the deposition of oxides, as a consequence, the base pressure is not particularly low, in the range of 10^{-5} mbar. This leaves 20% of this base pressure as the partial pressure of oxygen, thus providing ample opportunity for oxygen reactive sputtering in the case of susceptible metals such as titanium. The deposition parameters for both targets are listed in Table 4-1.

Table 4-1: Deposition parameters for TiN bottom electrode

Target	Power	Deposition pressure	N_2 gas	Substrate temperature	Deposition time
Ti metal	40-60 W	10 mTorr	20 sccm	650℃	1 h
TiN ceramic	20-40 W	10 mTorr	20 sccm	650℃	1 h

Figure 4-1 shows the surface topography obtained by both methods for different powers. The atomic force microscopy images were used to determine the root mean square (RMS) of the TiN layers under investigation. The RMS values are shown in Table 4-2. Roughnesses below nanometers are achievable by both methods.

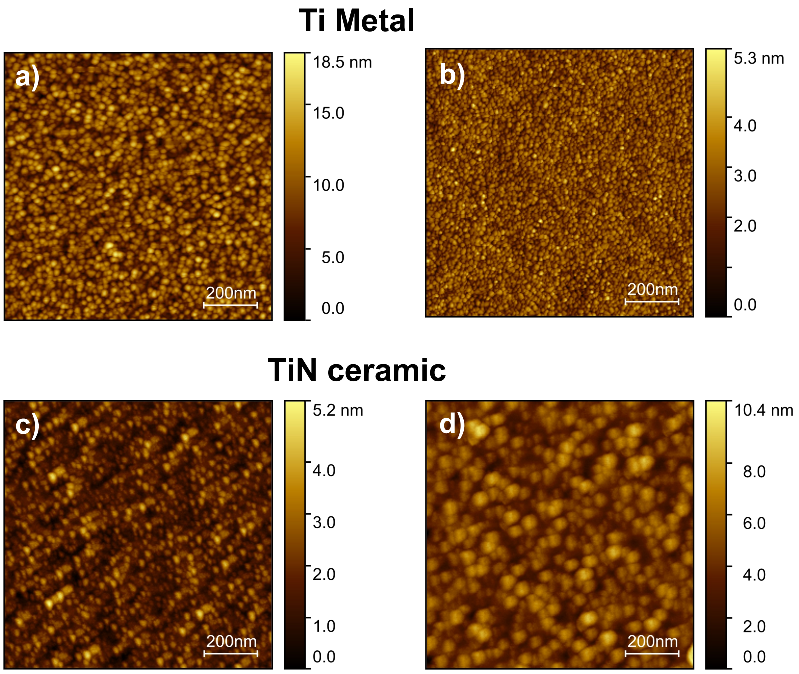

Figure 4-1: Surface topographies (AFM) of the effect of the target's type and power on the TiN bottom electrode surface.

Surface topographies of TiN sputtering from a Ti metal target at two different powers a) 40W, and b) 60 W and TiN sputtering from a Ti ceramic target at two different powers c) 20 W and d) 40 W.

Using the Van-der-Pauw method, the resistivity of the TiN layers was determined. The resistivity and RMS values for each film tested are shown in Table 4-2. The resistivity of TiN films obtained from a ceramic target was higher (an order of magnitude) than that obtained from a metallic target. As seen in the table, conductivity similar to that reported in the literature for TiN [100] was achieved when a metallic Ti target was used.

Table 4-2: Resistivity and roughness values for TiN.

Target	Power (W)	RMS (nm)	Resistivity (Ω·cm)
Ti metal	40	2.56	4.03×10^{-4}
	60	0.50	3.15×10^{-4}
TiN ceramic	20	0.73	8.83×10^{-3}
	40	2.98	1.11×10^{-3}

Two annealing methods were investigated to obtain the TiN electrode from metalic Ti target. In situ, heat the substrate during the sputtering process. Outside, sputter the sample at room temperature and then anneal it in a tubular oven under a nitrogen atmosphere. The TiN in situ was deposited at 80 W for one hour and at a substrate temperature of 600 °C. The TiN outside was again deposited at 80 W for one hour but at room temperature. Subsequently, the sample was annealed at 600 °C in a 60 sccm nitrogen flow for one hour.

Roughness (RMS) and resistivity (ρ) were used to compare these two methods. The external annealing method yielded an RMS = 2.47 nm and $\rho = 3.29 \times 10^{-4}$ Ω·cm. While the improved results were obtained by the in-situ annealing method an RMS = 0.54 nm and $\rho = 1.13 \times 10^{-4}$ Ω·cm.

Table 4-3: Resistivity and roughness values of TiN for two annealing method

Annealing method	Roughness (RMS) (nm)	Resistivity (Ω·cm)
In-situ	0.54	1.13×10^{-4}
External	2.47	3.29×10^{-4}

For the following of this document, TiN from a metallic target with an in-situ annealing process was used as the bottom electrode.

4.1.2 Orthorhombic phase in $Hf_{0.5}Zr_{0.5}O_2$

As discussed throughout this document, stabilizing the ferroelectric polar phase in $Hf_{0.5}Zr_{0.5}O_2$ is a complex process. In this section, we will discuss the effects of two annealing methods on the formation of the ferroelectric orthorhombic phase ($Pca2_1$), in-situ annealing and rapid thermal annealing (RTA). Diffractograms of samples of different thicknesses subjected to these two thermal processes were analyzed. Figure 4-2 shows the 2θ interval where the most distinctive peaks of the monoclinic ($P2_1/c$) at 28.5° (-111) and 31.8° (111), orthorhombic ($Pca2_1$) at 30.8° (111), and tetragonal ($P4_2/\mathrm{nmc}$) at 30.8° (101) phases are located. As is observed in the figure, the sample deposited for 30 minutes at a temperature of 550 °C shows a majority contribution from the monoclinic phase, with negligible or no contribution from the orthorhombic/tetragonal phases. In contrast, the samples subjected to rapid thermal annealing (RTA) for 60 seconds at a temperature of 750 °C showed an increase in the orthorhombic/tetragonal intensity. The overlapping positions of peaks (111) and (101) corresponding to the orthorhombic and tetragonal phases, respectively makes it difficult, if not impossible, to discriminate between them.

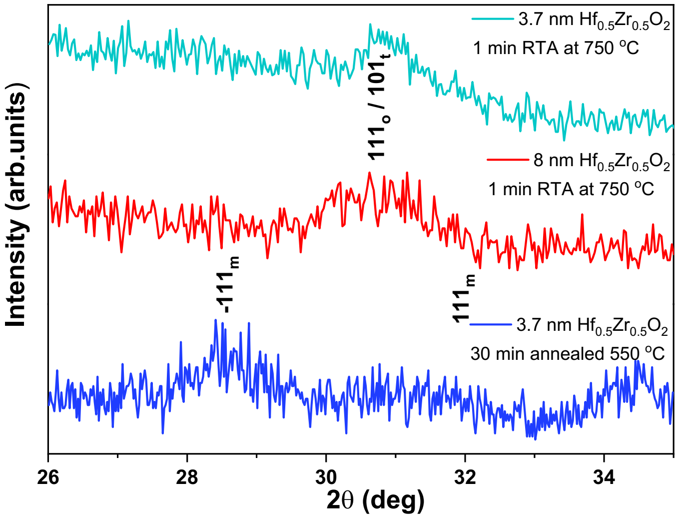

Figure 4-2: Diffractograms of samples of different thicknesses subjected to in-situ and RTA thermal processes.

The interval shows the most distinctive peaks of the monoclinic (*P*2_1/c) at 28.5° (-111) and 31.8° (111), orthorhombic (*Pca*2_1) at 30.8° (111), and tetragonal (*P*4_2/nmc) at 30.8° (101) phases.

In order to discriminate between the orthorhombic and tetragonal phases, a $Hf_{0.5}Zr_{0.5}O_2$ sample with a thickness of 3.7 nm subjected to RTA was investigated by piezoresponse force microscopy (PFM). A square area of 1 µm × 1 µm on the bare surface of the $Hf_{0.5}Zr_{0.5}O_2$ film was mapped with a constant tip voltage (-2V). Subsequently, a 0.5 µm × 0.5 µm constricted square was mapped with an opposite polarity constant voltage at the tip (+2V). As a result, in Figure 4-3, a phase contrast of ~180° can be distinguished between the two square regions written at -2V and +2V in a 2 µm × 2 µm phase map. The pristine area surrounding the external square showed a preferential spontaneous downward polarization. The dark line observed in the amplitude map (Figure 4-3) at the boundary between the oppositely polarized regions is commonly attributed to the domain walls [101].

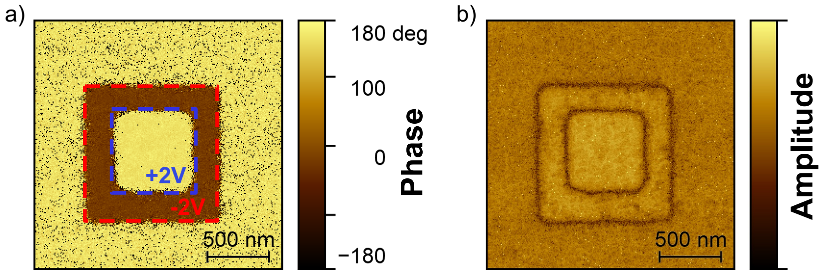

Figure 4-3: PFM phase and amplitude obtained on $Hf_{0.5}Zr_{0.5}O_2$ film exposed to RTA thermal processes.

a) phase, b) amplitude obtained on 3.7 nm thick $Hf_{0.5}Zr_{0.5}O_2$ film exposed to RTA thermal processes.

PFM measurements show steady reversible polarization in the ultrathin $Hf_{0.5}Zr_{0.5}O_2$ layer, coupled with the presence of the diffraction peak corresponding to the orthorhombic/tetragonal phase, indicates that the annealing of $Hf_{0.5}Zr_{0.5}O_2$ ultrathin films by RTA is a straightforward pathway for the formation of the ferroelectric orthorhombic phase ($Pca2_1$).

The RTA annealing time was also investigated. The diffractograms of two samples annealed for 60 seconds and 90 seconds are shown in Figure 4-4. As can be seen, the increase in annealing time slightly increased the intensity of the diffraction peak at $2\theta = 30.8°$. In addition, a new diffraction peak was observed at $2\theta = 27.74°$, related to the formation of an ultrathin TiO_2 film at the TiN/$Hf_{0.5}Zr_{0.5}O_2$ interface for 90 seconds of RTA.

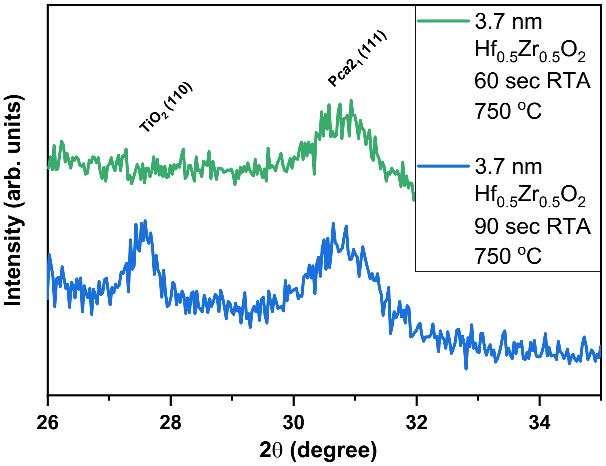

Figure 4-4: Diffractograms of TiN/$Hf_{0.5}Zr_{0.5}O_2$ samples subjected RTA at different deposition times.

The diffraction peak at $2\theta = 27.74°$ correspond to TiO_2 and $2\theta = 30.8°$ to orthorhombic ($Pca2_1$) and tetragonal ($P4_2$/nmc) phases

A detailed study of the formation of this TiO_2 layer is beyond the scope of this work. However, our preliminary results indicate that the TiN bottom electrode is strongly susceptible to temperature under high-oxidizing atmospheres.

4.1.3 $Hf_{0.5}Zr_{0.5}O_2$ as a function of the oxygen partial pressures

This section investigates the influence of oxygen partial pressure on the deposition rate of $Hf_{0.5}Zr_{0.5}O_2$ in RF-magnetron sputtering. The oxygen partial pressure was manipulated by changing the Ar:O_2 ratio in the sputtering chamber. The change of ratio is required in order to provide different oxygen partial pressures inside the chamber and as a consequence, different chemical potentials that will in return affect the oxygen vacancy concentration inside the film. At the same time, the sputtering yield of argon and oxygen is different. Based on momentum transfer to expel atoms from the target, argon is substantially more efficient than oxygen so that the change of composition of the process gas, even for the same total operating pressure, will result in very different sputtering rates. Once the different deposition rates are established, the overall film thickness may again be determined by an appropriate choice of the deposition time.

The thickness of the layers obtained for the different partial pressures of oxygen was determined by XRR. The XRR spectra for five $Hf_{0.5}Zr_{0.5}O_2$ samples deposited for 30 minutes at a power of 20 watts and a substrate temperature of 600 °C with different oxygen partial pressures are shown in Figure 4-5 (a). The dependence of the $Hf_{0.5}Zr_{0.5}O_2$ layer thickness on the oxygen partial pressure is depicted in Figure 4-5 (b).

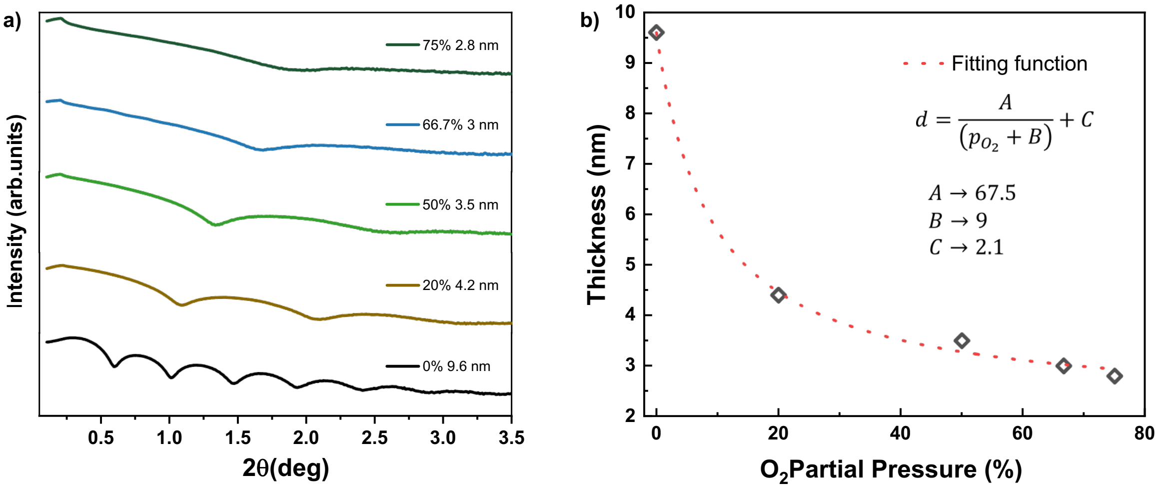

Figure 4-5: Thickness analysis of $Hf_{0.5}Zr_{0.5}O_2$ films deposited at different oxygen partial pressures.

a) XRR spectra measured on $Hf_{0.5}Zr_{0.5}O_2$ thin films deposited using different O_2 partial pressure during the sputtering process. b) $Hf_{0.5}Zr_{0.5}O_2$thin film thickness variation as a function of O_2 partial pressure in the sputtering chamber. The dashed red curve is a numerical fit.

Different Ar and O_2 sputtering yields will produce different deposition rates for each p_{O_2} and, consequently, a variation in the thickness of the sputtered $Hf_{0.5}Zr_{0.5}O_2$ films. The thickness of the $Hf_{0.5}Zr_{0.5}O_2$ film showed an inversely proportional dependence on oxygen partial pressure during the deposition, as can be seen in Figure 4-5(b). As expected, parameters *A*, *B* and *C* were found from the fit with the equation $d = C + A/(p_{O_2} + B)$ where d is the thickness of the deposited film and p_{O_2} is the oxygen partial pressure during the deposition.

The partial pressure of oxygen in the sputtering process of the $Hf_{0.5}Zr_{0.5}O_2$ film also influenced the post-annealing (RTA) of the $Hf_{0.5}Zr_{0.5}O_2$ films. Three samples obtained at different oxygen partial pressures were subjected to RTA for 60 seconds at a temperature of 750 °C. The diffractograms obtained in the GIXRD configuration for these samples are depicted in Figure 4-6.

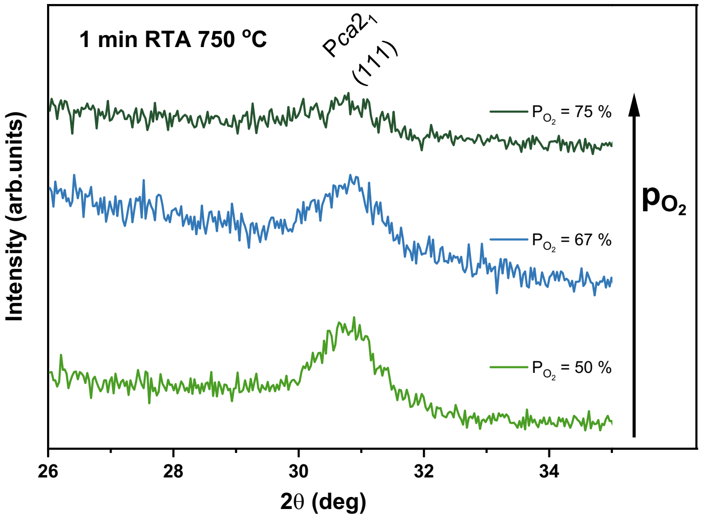

Figure 4-6: Diffractograms of samples sputtered under different O_2 partial pressure subjected RTA. Diffraction peak for orthorhombic (*Pca2$_1$*) phase at 30.8°. The arrow indicates the direction of the increase in oxygen partial pressure.

The intensity of the diffraction peak increases with the decrease of the oxygen partial pressure during sputtering. This result is in good agreement with the observations of Monica *et al.*, indicating that an oxygen-deficient $Hf_{0.5}Zr_{0.5}O_2$ film will promote the appearance of the ferroelectric orthorhombic phase [30].

A homogeneous $Hf_{0.5}Zr_{0.5}O_2$ film with a large portion of the orthorhombic phase is a crucial requirement for the functionality of $Hf_{0.5}Zr_{0.5}O_2$-based FTJs. However, achieving this orthorhombic phase via induction of oxygen vacancies will adversely affect the device's leakage current. A study of the influence of oxygen partial pressure on the conduction mechanisms through the TiN/$Hf_{0.5}Zr_{0.5}O_2$/Au stack is presented in the following section.

4.2 Competing tunneling conduction mechanisms in oxygen-deficient $Hf_{0.5}Zr_{0.5}O_2$

Disclaimer: This section contains a partial or complete description (including verbatim) of the results published on *Appl. Phys. Lett.* 119, 132906 **2021** with the permission of AIP Publishing.

Tunneling regimes represent the ultimate thickness limitation for solid-state electronics. While tunneling was mainly addressed as a nuisance for the scaling of dielectrics, its control holds promise for ultrathin memory devices with tunable resistivity, including ferroelectric tunnel junction (FTJ). Hafnium zirconium oxide-based FTJ devices sparked a growing interest due to their full compatibility with the CMOS process [102]. When the thickness of the $Hf_{0.5}Zr_{0.5}O_2$ layer decreases to a few nanometers, the conduction mechanism can be described by direct tunneling at low electric fields [7]. However, at high electric fields, the variation of barrier thickness can lead to the domination of additional transport mechanisms such as Fowler-Nordheim tunneling (FNT) [82].

The most common intrinsic defects in an idealized perfect and undoped material are vacancy. Despite extensive studies on the ferroelectric phase of $Hf_{0.5}Zr_{0.5}O_2$ for non-volatile ferroelectric random-access memories, the investigation of the effect of oxygen vacancies on the switching mechanism is only beginning [103]. Aware that the effect of oxygen vacancies on the ferroelectric phase deserves full attention for the sake of ferroelectric tunnel junctions, [30, 50, 66] the mere presence of oxygen vacancies in any tunnel junction, regardless of whether they are ferroelectric or not, offers the opportunity for another type of resistive switching via trap-assisted tunneling. This mechanism is intrinsically compatible with multilevel-switching and neuromorphic switching via a controlled modulation of the oxygen vacancy concentration.

This section shows the electrical properties of structures with different intrinsic oxygen vacancies concentrations, achieved via controlling the oxygen partial pressure during the deposition of $Hf_{0.5}Zr_{0.5}O_2$ thin films by RF magnetron sputtering. We aim to study the contribution of direct tunneling and trap-assisted tunneling conduction mechanisms to the current through $TiN/Hf_{0.5}Zr_{0.5}O_2/Au$ devices synthesized with two different oxygen partial pressures: $p_{O_2}= 50\%$ and $p_{O_2}= 67\%$.

4.2.1 Two-terminal $Ti/Hf_{0.5}Zr_{0.5}O_2/Au$ capacitors fabrication

Two-terminal $Ti/Hf_{0.5}Zr_{0.5}O_2/Au$ capacitors were designed for this study. The samples were fabricated on (100) p-type Si substrates by radio frequency (RF) magnetron sputtering (tabletop SPT310 system from Plasmionique Inc.). Before each deposition, the chamber is evacuated with a mechanical vacuum pump followed by a turbomolecular vacuum pump to reach a base pressure below 10^{-5} Torr. The TiN bottom electrode and $Hf_{0.5}Zr_{0.5}O_2$ thin oxide films were deposited on a cleaned 0.5 cm x 0.5 cm Si/SiO_2 substrate sequentially without breaking the vacuum of the sputtering chamber. TiN was sputtered from a metal target onto the substrate at a temperature of 650°C for 30 minutes with a power of 100 watts at a pressure of 5 mTorr under a nitrogen atmosphere. A detailed characterization of the TiN deposition can be found in section 4.1.1. A polycrystalline, stoichiometric $Hf_{0.5}Zr_{0.5}O_2$ ceramic disk was used as a sputtering target for the ferroelectric films. The $Hf_{0.5}Zr_{0.5}O_2$ was sputtered in the TiN-coating substrate at a temperature of 600°C, with a power of 20 watts for 30 minutes at a pressure of 5 mTorr under a mixture of Ar:O_2. The oxygen partial pressure in the mixture varied for each sample. In the two samples under investigation, the Ar:O_2 rate varied from 1 to 1.5, corresponding to an oxygen partial pressure (p_{O_2}) of 50% and 67%, respectively. The Au top electrodes were deposited using a shadow mask with circular holes with a diameter of 300 μm, resulting in electrodes with a contact area $A = 7.1\times10^{-4}$ cm^2. The deposition was conducted at room temperature using an Au target for five minutes, a power of 20 watts, and a pressure of 6 mTorr with an Argon flow rate of 8 SCCM.

4.2.2 Structural characterization

The crystal structure and crystalline quality of the deposited $Hf_{0.5}Zr_{0.5}O_2$ thin films were evaluated from X-ray diffraction analysis (XRD). Figure 4-7(a) shows the XRD pattern for two samples of $Hf_{0.5}Zr_{0.5}O_2$ deposited by RF- magnetron sputtering under an oxygen partial pressure of $p_{O_2} = 50\%$ and $p_{O_2} = 67\%$. The diffractogram was recorded in a PANalytical X'pert Pro diffractometer using 2° grazing incidence configuration (ω-2θ mode) from 20° to 55° with a 0.02° step size and an integration time of 3 s/step.

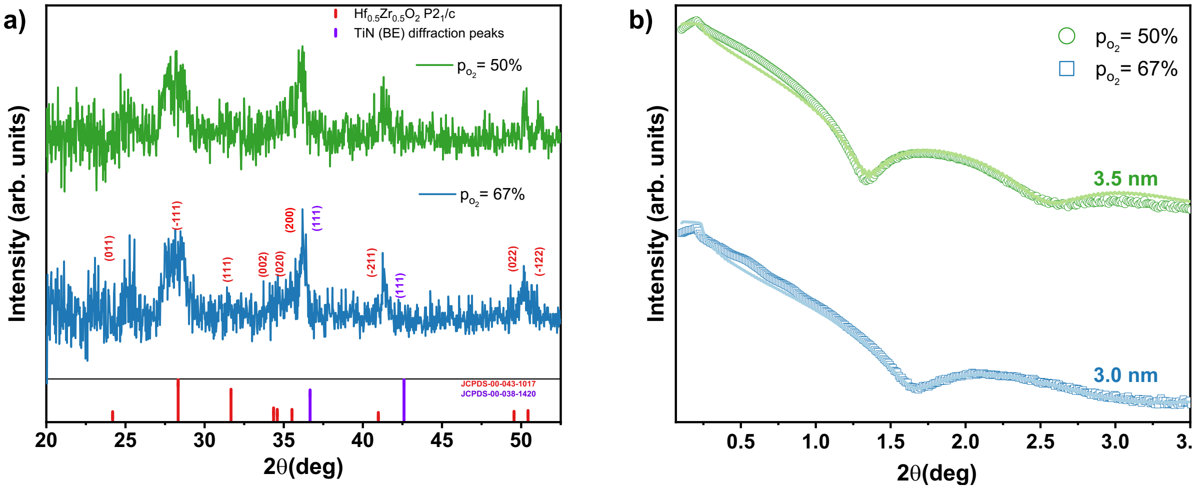

Figure 4-7: X-ray diffraction analysis of $Hf_{0.5}Zr_{0.5}O_2$ deposited by RF- magnetron sputtering under different oxygen partial pressures.

(a) XRD patterns and (b) XRR spectra (symbols) and fitted curves (solid line) measured on $Hf_{0.5}Zr_{0.5}O_2$ thin films deposited using p_{O_2}= 50%, and p_{O_2}= 67%.

XRD data confirmed that the synthesized $Hf_{0.5}Zr_{0.5}O_2$ thin films were well crystallized and the predominantly in the monoclinic phase. Two peaks can be distinguished in both cases, located at $2\theta = 36.663°$ and 42.597°, corresponding to the TiN bottom electrode.

X-ray reflectivity (XRR, PANalytical X'pert Pro diffractometer) was used to determine the thickness of the thin films under study. Figure 4-7(b) shows the XRR data for the two samples of $Hf_{0.5}Zr_{0.5}O_2$ with p_{O_2}= 50% and p_{O_2}= 67%. By fitting the diffractograms, an average thickness of 3.5 nm and 3 nm for the $Hf_{0.5}Zr_{0.5}O_2$ films deposited with p_{O_2}= 50% and p_{O_2}= 67%, respectively, were determined.

4.2.3 Electrical characterization

The electrical characterization of the samples obtained at the two oxygen partial pressures was performed by subjecting them to voltage-current loops. Figure 4-8 shows the I(V) characteristic of two TiN/$Hf_{0.5}Zr_{0.5}O_2$/Au structures deposited under p_{O_2}= 50% (3.5 nm) and p_{O_2}= 67% (3 nm), respectively. Both samples exhibit a butterfly-shaped nonlinear I-V characteristic curve.

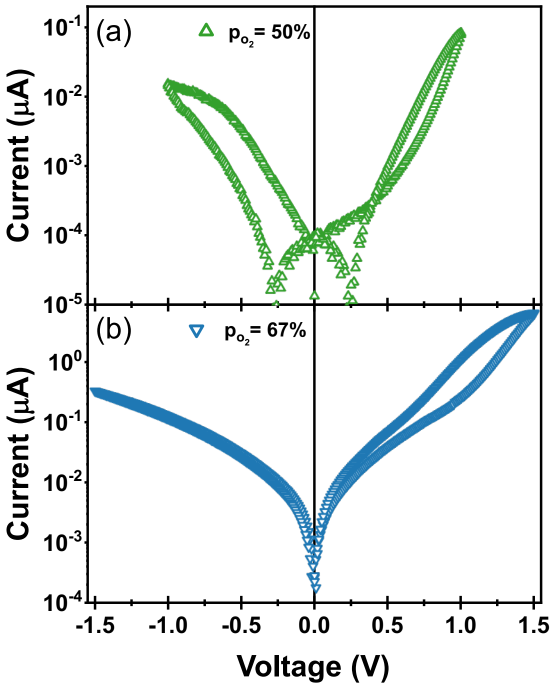

Figure 4-8: Current-voltage characteristics of the TiN/$Hf_{0.5}Zr_{0.5}O_2$/Au devices.

The I-V characteristics of two TiN/$Hf_{0.5}Zr_{0.5}O_2$/Au devices with the $Hf_{0.5}Zr_{0.5}O_2$ thin films deposited under an oxygen partial pressure of a) p_{O_2}= 50%, and b) p_{O_2}= 67%. Figures a) and b) show the absolute value of the current on a logarithmic scale.

Notably, the I–V characteristic shows significant change with the variation of the oxygen partial pressure and thickness of the $Hf_{0.5}Zr_{0.5}O_2$ layers, as shown in Figure 4-8 (a) and (b). The magnitudes of tunneling current for the 3.5 and 3 nm thick $Hf_{0.5}Zr_{0.5}O_2$ thin films depend exponentially on the thickness of the thin film. The influence of the dielectric thickness is, thus, crucial for the device's operation.

To illustrate this point, we can briefly refer to the fundamental tunneling theory through a one-dimensional potential barrier, as shown in Figure 4-9.

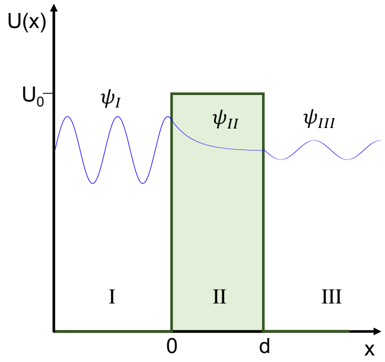

Figure 4-9: Quantum tunneling through a potential barrier.

The solutions of the stationary Schrödinger equation characterize the three regions of the quantum-tunneling problem: Oscillatory behavior in regions I and III, and exponential-decay behavior in region II.

In this case, quantum mechanics describes an electron under a potential U(x) by a wave function ψ(x), which satisfies the time-independent Schrödinger's equations.

Equation 4-1 Time-independent Schrödinger's equations

$$-\frac{\hbar^2}{2m}\frac{d^2}{dx^2}\psi(x) + U(x)\psi(x) = E\psi(x)$$

the solution of the time-independent Schrödinger's equations for each region are:

$$\psi_I = e^{ikx} + Ae^{-ikx}$$

$$\psi_{II} = Be^{-\varkappa x} + Ce^{\varkappa x}$$

$$\psi_{III} = De^{ikx}$$

Where: $\boldsymbol{k} = \frac{\sqrt{\boldsymbol{2m(E-|U|)}}}{\hbar}$ **is the wave vector.**

$\boldsymbol{\varkappa} = \frac{\sqrt{\boldsymbol{2m(|U|-E)}}}{\hbar}$ **is the decay constant**

The constants A, B, C and D are determined from the boundary conditions by matching the wave functions and their derivatives $d\psi/dx$ at the two extremes.

The transmission coefficient (T) can be presented as the ratio between the transmitted current density and the incident current density as indicate in equation 4-2:

Equation 4-2 Transmission coefficient

$$T = \frac{I_t}{I_i} = |D|^2 = \frac{1}{1 + \frac{(k^2 + \varkappa^2)^2}{4k^2\varkappa^2} sinh^2(\varkappa d)}$$

For large decay rate T can be simplified to:

$$T \sim \frac{16\, k^2\varkappa^2}{(k^2 + \varkappa^2)^2} e^{-2\varkappa d}$$

Our experimental results show that for smaller thicknesses, larger tunneling currents were obtained in the device with a 3 nm thick $Hf_{0.5}Zr_{0.5}O_2$ layer, as compared to the 3.5 nm thick film. According to equation 4-2 and considering $\varkappa = 5nm^{-1}$ in our case, for an increase of 0.5 nm, the current should drop by a factor of $\sim e^5$, which is about three orders of magnitude. In contrast to this estimation, our experimental results show lower current values at identical voltages at approximately one order of magnitude. A thorough analysis of the conduction mechanisms is essential to elucidate this inconsistency.

4.2.4 Tunneling mechanisms through TiN/$Hf_{0.5}Zr_{0.5}O_2$/Au devices

Different conduction mechanisms have been suggested to describe the tunneling current, depending on the operating electric fields of the tunnel junction devices, including direct tunneling, Fowler–Nordheim, tunneling, and thermionic injection [82]. In general, for small thicknesses and low electric fields, when the barrier thickness is ultrathin (typically less than 4 nm), the electrons can tunnel through a trapezoidal barrier, and direct tunneling becomes the defining conduction mechanism (Figure 2-16). Therefore, the transport properties of the TiN/$Hf_{0.5}Zr_{0.5}O_2$/Au heterojunctions fabricated using 3 nm thick $Hf_{0.5}Zr_{0.5}O_2$ (p_{O_2}= 67%) were investigated first using a direct tunneling mechanism.

The tunneling current density (J) for direct tunneling can be calculated using the Wentzel-Kramers–Brillouin (WKB) approximation depicted in Equation 2-4.

Two different resistance states are present in the I–V curve of the 3 nm sample (p_{O_2}= 67%), the high resistance state (HRS) and the low resistance state (LRS). As shown in Figure 4-10(a), these states were modelled using equation 2-4 with the potential barriers Φ_1 and Φ_2 at the interfaces of the electrodes reported in the literature (see Table 4-4) [104] and an effective mass of $m^* = 0.49m_0$ determined from our experimental results. For voltages from –1 to 0.5 V, it can be noticed that the current calculated from equation 2-4 for the HRS is in good agreement with the experimental measurement. In contrast, the deviation between the model and experimental measurements for the LRS is attributed to the negligible portion of the polar phase in the device.

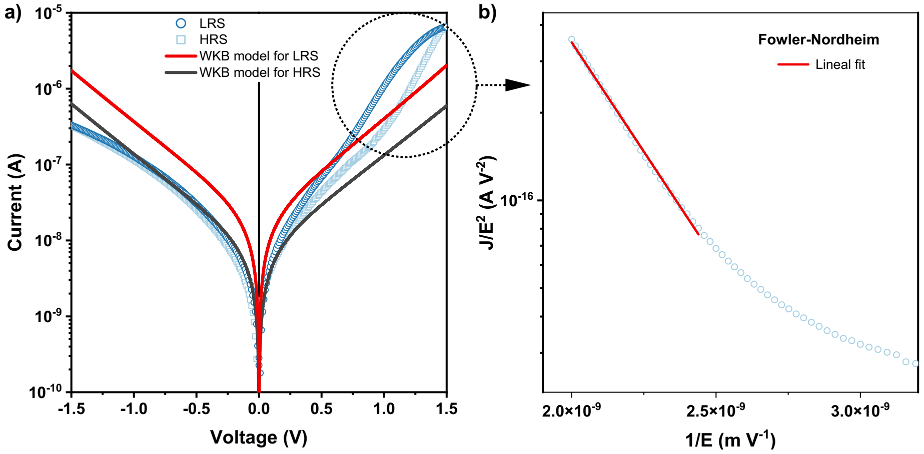

Figure 4-10: Two tunneling regimes of TiN/$Hf_{0.5}Zr_{0.5}O_2$/Au device.

Experimental (symbols) and fitting (solid) I–V curves for low resistive state (LRS) and high resistive state (HRS) of TiN/ $Hf_{0.5}Zr_{0.5}O_2$/Au device with $Hf_{0.5}Zr_{0.5}O_2$ deposited using p_{O_2}= 67%. a) I–V behavior in the HRS and the LRS according to WKB approximation for low field region. b) Fowler–Nordheim fitting plot for high field region.

At high bias, the WKB model no longer accurately describes the current response in the sample. In this regime, as expected, Fowler–Nordheim tunneling (FNT) describes the electron transport for thicker barriers and relatively large electric fields. When the applied voltage (V) exceeds the barrier height, electrons tunnel through an effective triangular barrier that constitutes Fowler-Nordheim tunneling (Figure 2-17). Following Equation 2-7, the J–E characteristics of the tunneling current for Fowler–Nordheim tunneling (FNT) mechanism should satisfy the linear function relationship between $\ln(J/E^2)$ and 1/E. The obtained fitting suggests that Fowler-Nordheim tunneling provides an excellent description, as shown Figure 4-10 (b).

Table 4-4: Interface potentials.

Interface potential	Value[1]
$\Phi^{\downarrow}_{Top}$	2.14 eV
$\Phi^{\uparrow}_{Top}$	2.42 eV
$\Phi^{\downarrow}_{Bot}$	2.33 eV
$\Phi^{\uparrow}_{Bot}$	2.27 eV

[1]Reproduced from Yoon *et al.* [104]

Our next step is to apply the same procedure to the sample obtained with a partial pressure of 50% in order to determine the effect of oxygen partial pressure on the transport mechanism in $Hf_{0.5}Zr_{0.5}O_2$. In other words, to confirm the correlation between tunneling currents and oxygen vacancies. A comparison between the experimental I–V characteristic of 3.5 nm sample (p_{O_2}= 50%) (symbols) and both WKB (dashed line) and phonon-assisted tunneling between traps (solid line) models is shown in Figure 4-11. The current for the HRS and the LRS according to the WKB approximation was calculated using the parameters reported in Table 4-4. The current values measured in the sample are an order of magnitude larger than that calculated using the WKB approximation (Equation 2-4) with the appropriate parameters, suggesting the presence of a second conduction mechanism. The reduction of oxygen partial pressure from 67 to 50 % during $Hf_{0.5}Zr_{0.5}O_2$ deposition resulted in a change in both HRS and LRS conductivities.

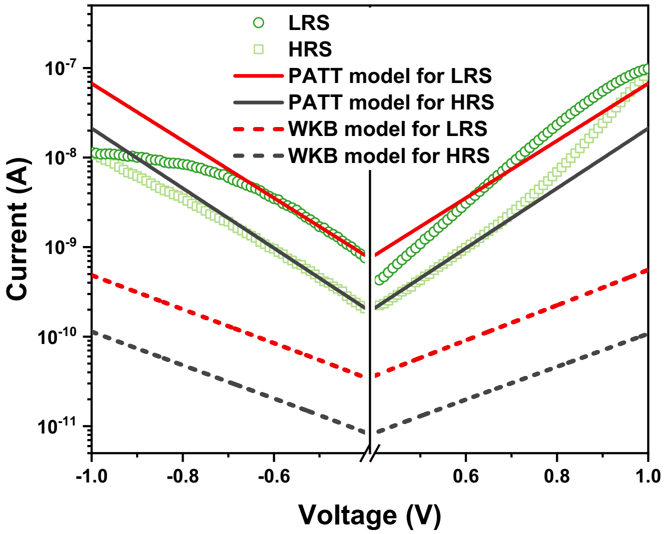

Figure 4-11: Experimental and modelled I–V curves for LRS and HRS of TiN/$Hf_{0.5}Zr_{0.5}O_2$/Au device with $Hf_{0.5}Zr_{0.5}O_2$ deposited using a O_2 partial pressure of 50%.

The solid lines correspond to the PATT model, and the dashed lines to the WKB model.

To describe this transport and to determine the distance between traps, we used the phonon-assisted tunneling between traps (PATT) model (see illustration in Figure 2-19), which was initially developed by Makram-Ebeid and Lannoo [105]. It has been shown that this transport model offers an accurate description of electrical properties in both ferroelectric and non-ferroelectric $Hf_{0.5}Zr_{0.5}O_2$ [90].

The model based on the PATT mechanism (Equation 2-10) is shown in Figure 4-11. The HRS (black solid line) and the LRS (red solid line) are evaluated using the parameters reported in Table 4-5 and for a thickness of $d = 3.5\ nm$. The result indicates a good quantitative agreement between the PATT model and I–V curves. The obtained effective mass $m^* = 0.33m_0$ is in good agreement with the previous value of tunnel effective mass reported in the literature for this material [90, 106]. The average distance between traps of 1.39 and 1.27 nm was determined by the fit of HRS and

LRS measurements, respectively. Even though it could not be independently corroborated so far, the values are close to the experimentally meaningful threshold of half the thickness.

Table 4-5: PATT model parameters for $Hf_{0.5}Zr_{0.5}O_2$.

Description	Symbol	Value	Reference
Thermal energy of the trap	W_T	1.25 eV	Islamov *et al*. [107]
Optical energy of the trap	W_{opt}	2.5 eV	
Fraction of filled traps	n_t/N	0.5	This work
Effective electron mass	m^*	0.33 m_0	This work

Starting from the LRS for increasing negative bias voltage, as the electric field strength exceeds $\sim 2\ MV/cm$, an increase in the average distance between traps is observed. This indicates an annihilation of oxygen vacancies and switching of the sample into HRS. The sample remains in the HRS until the positive bias reaches $\sim 2\ MV/cm$ at which point new oxygen vacancies are being generated. The electric field required for oxygen vacancy generation/annihilation is lower than reported by Strand *et al.* [108], an observation that we attribute to pre-existing oxygen vacancies. The pre-existing vacancies act as electron traps, and the vacancies that form are stable, reducing the energy of defect formation [109].

4.2.5 Direct vs trap-assisted tunneling

In order to assess whether direct or trap-assisted tunneling prevails, we now discuss the effect of $Hf_{0.5}Zr_{0.5}O_2$ layer thickness and trap distance. Figure 4-12(a) shows the current densities resulting from DT and PATT conduction mechanisms as a function of the average distance between traps for a fixed bias of 0.5 V and for a $Hf_{0.5}Zr_{0.5}O_2$ layer thickness of 3.5 nm. Figure 4-12(b) shows the current densities resulting from DT and PATT conduction mechanisms as a function of $Hf_{0.5}Zr_{0.5}O_2$ thickness at a fixed bias voltage of 0.5 V and an average distance between traps of 1.5 nm. In both cases, the potential barriers for the HRS polarization state were used in the WKB approximation. The direct tunneling current density is approximately independent of the distance between traps, as shown in Figure 4-12(a). In contrast, the current density for the trap-assisted tunnel depends exponentially on the average distance between traps. Consequently, for small inter-trap distances, the contribution of the trap-assisted current will be significantly larger than the direct tunneling current, as we experimentally demonstrated for sample p_{O_2}= 50% (Figure 4-11). However, for a larger distance between traps, the probability of trap-assisted tunneling rapidly decreases, which means that the total current will be dominated by direct tunneling.

This result is corroborated experimentally in the sample p_{O_2}= 67% (Figure 4-10). The same is true when we fix a constant average distance between traps and analyze the dependence of the current density on the thin film thickness (Figure 4-12(b)). At small thicknesses, the rate at which electrons tunnel through the barrier is high, so the contribution of the direct tunneling current is large. As the thickness increases, the contribution of direct tunneling decreases exponentially, reaching a critical thickness at which trap-assisted tunneling becomes dominant.

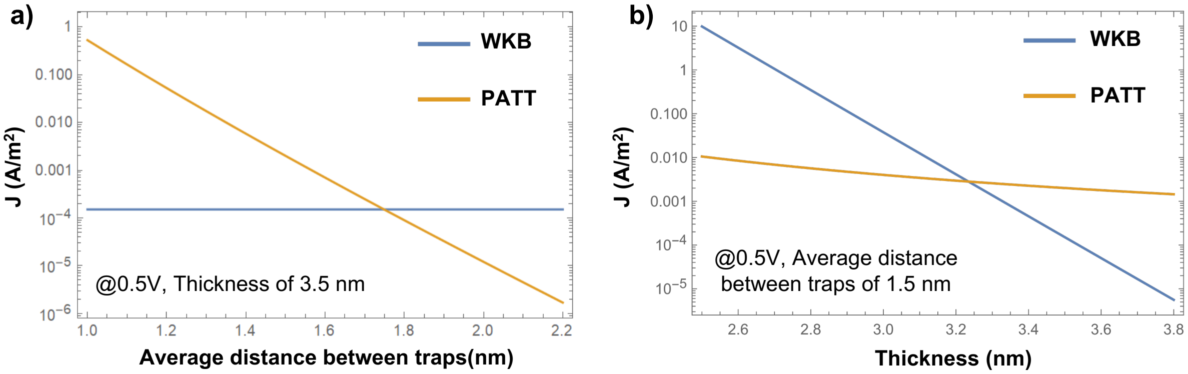

Figure 4-12: Semi-logarithmic plot of the current density contributions from DT, and PATT.

Semi-logarithmic plot of the current density contributions from DT, and PATT as a function of a) the average distance between traps and b) the thickness.

4.2.6 Endurance of direct and trap-assisted tunneling

As we demonstrated above, both the direct tunneling and the trap-assisted tunneling have the characteristic of providing two different states; HRS and LRS. These states will be modulated by the polarization reversal in the case of FTJ (direct tunneling) and by the average distance between traps (oxygen vacancies) in the case of trap-assisted tunneling. Therefore, the reliability of these states will depend on the inherent properties of these two processes. In the case of an ideal FTJ, the recurring application of an alternating electric field (e.g. pulse cycle of opposite bias) will produce a polarization reversal indefinitely. However, various factors such as electric field imprint, domain wall pinning, degradation of the ferroelectric-electrode interface or oxygen vacancies will cause a degradation of the remaining polarization, leading to device fatigue. For trap-assisted tunneling, a somewhat unstable performance is expected due to its direct connection with the formation/annihilation of defects in the material.

To investigate these scenarios, we subjected the devices obtained under p_{O_2}= 50% and p_{O_2}= 67% to 6×10^3 cycles of write/erase. Figure 4-13 shows the HRS and LRS for both samples.

In this study, we used a pulse sequence, as shown in Figure 3-8, with write and erase voltages of -2 and 2 volts, respectively, for the samples with p_{O_2}= 50% (3.5 nm) and p_{O_2}= 67% (3 nm). In both cases, a read voltage of 0.6 V was used.

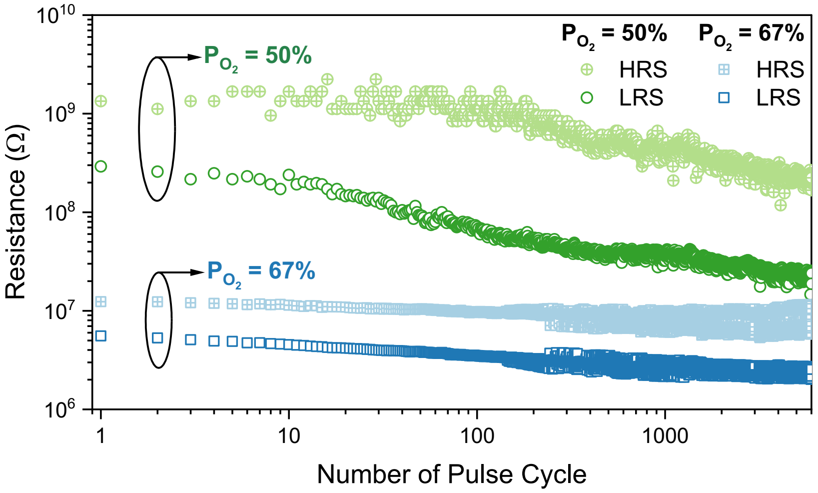

Figure 4-13: Endurance measurement on two TiN/$Hf_{0.5}Zr_{0.5}O_2$/Au devices obtained under different oxygen partial pressure.

Log-log plot of resistance as a function of cycle number. The circles correspond to a device obtained with p_{O_2}= 50% (3.5 nm), and the squares correspond to a device obtained with p_{O_2}= 67% (3 nm).

The HRS and LRS states of the p_{O_2}= 67% sample show a stable trend during cycling with an approximately constant but slightly reduced LRS/HRS ratio, possibly due to the negligible portion of the polar phase in the device. This remarkable stable trend of the HRS and LRS corresponds with a relatively low defect rate (oxygen vacancy) in the $Hf_{0.5}Zr_{0.5}O_2$ film.

In contrast, the device based on varying average inter-trap distances (p_{O_2}= 50%) shows a higher LRS/HRS ratio. However, the HRS and LRS have a drift towards lower resistances, making it impossible to define a unique threshold to discriminate HRS against LRS throughout the complete operation of the device. This drift renders the system less suitable for use as a memory cell.

The HRS and LRS splitting at 120 cycles and above, which is observed in the p_{O_2}= 67% sample, will not be discussed in this document as it is currently under investigation. This behavior was observed only in the cells obtained at p_{O_2}= 67%, which may provide linkage with a logistic map (negative feedback loop) associated with different ferroelectric domain populations.

4.2.7 Summary

We investigated the electrical properties of $Hf_{0.5}Zr_{0.5}O_2$ thin films deposited by the RF magnetron sputtering method, with varying oxygen partial pressures. We show that the variation in oxygen partial pressure induces a change in the conduction mechanism within the TiN/$Hf_{0.5}Zr_{0.5}O_2$/Au device due to the variation of the intrinsic concentration of oxygen vacancies. The two competing tunneling mechanisms in $Hf_{0.5}Zr_{0.5}O_2$ are direct tunneling and trap-assisted tunneling. Our experimental data for p_{O_2}= 67% are found to be in good agreement with a WKB model. In contrast to that, the reduced oxygen partial pressure of p_{O_2}= 50% shows a good agreement with the PATT transport model, which yielded an average distance between traps of 1.39 and 1.27 nm for the HRS and LRS case, respectively. The switching in the PATT regime was explained by formation/annihilation of oxygen vacancies. Using the thickness dependence in the equations of the PATT and WKB models and selecting the appropriate parameters, we report a critical thickness at which the transition between the two mechanisms occurs. We confirm that for small inter- trap distances, the trap-assisted current is significantly larger than that of the direct tunneling current. As shown in this work, the dominant conduction mechanism can be controlled by defect concentration and film thickness. However, the film thickness has been reported to be critical for device stability due to the high sensitivity of tunneling currents with respect to thickness [99]. Therefore, we would like to highlight the importance of controlling the amount of intrinsic traps. Both the technological processes of film synthesis and post-treatment, such as annealing in O_2 atmosphere, are vitally important in this matter.

4.3 Oxygen vacancy filament-based resistive switching in non-polar $Hf_{0.5}Zr_{0.5}O_{2-\delta}$ thin films

Disclaimer: This section contains a partial or complete description (including verbatim) of the results adapted with permission from *ACS Appl. Electron. Mater*. **2022**, 4, 3, 1311–1317. Copyright 2022 American Chemical Society.

In the last decade, Hafnium zirconium oxide ($Hf_{0.5}Zr_{0.5}O_2$) in its thin-film form has been considered as a prominent candidate for the future design and fabrication of non-volatile memories applications, in particular, to develop resistive random-access memory (ReRAM) devices [110-115]. Nevertheless, many challenges related to the optimization of the structural and electronic properties of $Hf_{0.5}Zr_{0.5}O_2$ still have to be addressed to meet the technological needs and conditions.

The high performance of resistive switching memory devices relies on optimizing several parameters and principally the defect concentration in the dielectric barrier material [116-118]. The presence of high defect concentration, i.e. oxygen vacancies, may impact the electron transport mechanisms and switching performance of $Hf_{0.5}Zr_{0.5}O_2$ thin films and the degradation of its orthorhombic phase and, as a consequence, its ferroelectric properties [119]. In this case, the electron transport mechanism may be dominated by the migration of oxygen vacancies (V_o), filamentary paths' formation and rupture, and charge carriers' trapping and de-trapping [69, 120].

In order to achieve high performance of $Hf_{0.5}Zr_{0.5}O_2$-based resistive random-access memories (ReRAM), the study of the effects related to the oxygen vacancies formation has to be considered to a better understanding of the mechanisms involved in the switching process [34].

In the present section, a ReRAM device based on an oxygen-deficient $Hf_{0.5}Zr_{0.5}O_{2-\delta}$ storage layer was fabricated using RF magnetron sputtering in order to investigate the electrical properties and performance of these memory cells.

4.3.1 Oxygen-deficient Ti/$Hf_{0.5}Zr_{0.5}O_{2-\delta}$/Au ReRAM fabrication

The two-terminal metal-insulator-metal (MIM) capacitors were deposited on (100) p-type Si/SiO substrates by radio frequency (RF) magnetron sputtering (tabletop SPT310 system from Plasmionique Inc.). The device was manufactured in two steps; (1) the bottom electrode (TiN) and the oxide layer ($Hf_{0.5}Zr_{0.5}O_2$) were deposited consecutively without breaking the vacuum of the sputtering chamber, and (2) top electrodes (Au) were deposited using a shadow mask with circular holes of 300 µm in diameter. The deposition parameters are listed in Table 4-6.

Table 4-6: Deposition parameters for TiN/$Hf_{0.5}Zr_{0.5}O_{2-\delta}$/Au memory cells

Target	Power	Deposition pressure	Medium	Substrate temperature	Deposition time
TiN	100 W	5 mTorr	N_2	650°C	30 min
$Hf_{0.5}Zr_{0.5}O_2$	20 W	5 mTorr	Ar	600°C	90 min
Au	20 W	6 mTorr	Ar	RT	5 min

Unlike the $Hf_{0.5}Zr_{0.5}O_2$ deposition discussed previously in section 4.2.1, oxygen was suppressed entirely from the sputtering chamber during the synthesis of the $Hf_{0.5}Zr_{0.}5O_2$ layer under analysis in this section. By suppressing the O_2, we aimed to create as many vacancies as possible in the $Hf_{0.5}Zr_{0.}5O_2$ oxide layer to investigate their influence on the electrical response of the layer.

4.3.2 Morphology and structure of TiN/$Hf_{0.5}Zr_{0.5}O_{2-\delta}$/Au memory cells

The morphology and structure of the as-synthesized TiN bottom electrode and $Hf_{0.5}Zr_{0.5}O_{2-\delta}$ oxide layer were analyzed by AFM and XRD, respectively, as shown in Figure 4-14. The Figure 4-14 (a) and (b) show the topography images of the TiN bottom electrode and the $Hf_{0.5}Zr_{0.5}O_{2-\delta}$ layer of the device structure. The morphology of the TiN electrode indicates the formation of a smooth surface of a homogeneous grainy layer with an average root mean square (RMS) roughness of 0.7 nm, while the surface morphology of the as-grown $Hf_{0.5}Zr_{0.5}O_{2-\delta}$ layer on TiN indicates a slight increase in the grain size of the nanostructures which uniformly cover the TiN surface.

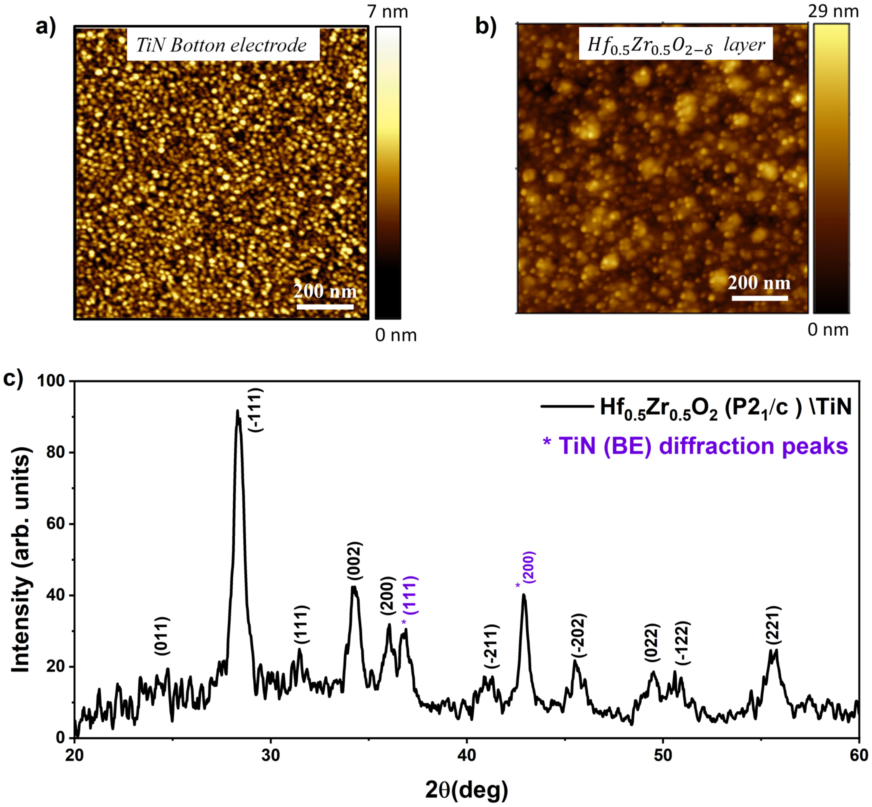

Figure 4-14: Morphology and structural characterization of the deposited TiN bottom electrode and $Hf_{0.5}Zr_{0.5}O_{2-\delta}$ film.

(a) (1 µm × 1 µm) AFM morphology of the TiN bottom electrode, (b) (1 µm × 1 µm) AFM morphology of the $Hf_{0.5}Zr_{0.5}O_{2-\delta}$ layer deposited on the TiN bottom electrode, (c) XRD pattern for the TiN/ $Hf_{0.5}Zr_{0.5}O_{2-\delta}$ film.

To obtain information about the crystal phase analysis of the $Hf_{0.5}Zr_{0.5}O_{2-\delta}$ film deposited on the TiN bottom electrode, phase identification by XRD was performed (Figure 4-14(c)). The grazing incidence scan indicates the presence of the (111) and (200) reflections of the TiN bottom electrode at approximately $2\theta = 36.8°$ and $2\theta = 42.9°$, while all the other diffraction peaks can be indexed to the monoclinic structure ($P2_1/c$) of $Hf_{0.5}Zr_{0.5}O_{2-\delta}$ film. No impurity peaks are observed in the diffraction pattern. Using XRR measurements, the oxide layer thickness of the device was estimated to be ~ 40 nm.

4.3.3 Electrical characterization of TiN/$Hf_{0.5}Zr_{0.5}O_{2-\delta}$/Au memory cells

The DC current-voltage (I–V) characteristic of the typical TiN/$Hf_{0.5}Zr_{0.5}O_{2-\delta}$/Au memory cell is shown in Figure 4-15(a). As can be noticed in the first cycle, highlighted in red, the pristine state is the high resistive state (HRS). When the voltage bias is swiped from 0 V to -3.5 V, the device switches to the low resistance state (LRS) at the set voltage (V_{Set}) of approximately -2 V. On the reverse sweep, from 0V to +3.9 at the reset voltage (V_{Reset}) of approximately 2.5 V, the device switches from HRS to LRS. This confirms the non-volatile bipolar resistive switching behavior. The presence of an electroforming process was not observed, which may be due to the intentionally induced high initial defect concentration. In contrast to the samples described in section 4.2, the $Hf_{0.5}Zr_{0.5}O_{2-\delta}$ layer studied in this section was deposited in a fully oxygen-depleted atmosphere (p_{O_2}= 0%). It enhances the formation of defects (oxygen vacancies) in the oxide layer [34]. To investigate the stability and reproducibility of the memory, 100 continuous DC cycles were analyzed. The distribution of the set and reset voltages are shown in a histogram in Figure 4-15(b). The V_{Set} shows a mean of -1.92 V with a standard deviation of 0.14 V, while the mean for the V_{Reset} was 2.67 V with a standard deviation of 0.11 V. Narrow distribution with slight standard deviations are a strong indicator of memory stability. The device showed an excellent ΔR/R ratio of 204 extracted at 0.1 V over 100 DC sweep cycle (Figure 4-15(c)), R_{HRS} = 27.02 ± 9.25 KΩ (mean value: 27.02 KΩ; standard deviation: 9.25 KΩ) and R_{LRS} = 134.2 ± 17.8 Ω (mean value: 134.2 Ω; standard deviation: 17.8 Ω). The slope of the LRS was nearly vertical, while the HRS exhibited a narrow distribution. Figure 4-15(d) shows the distribution of HRS and LRS in 8 memory cells.

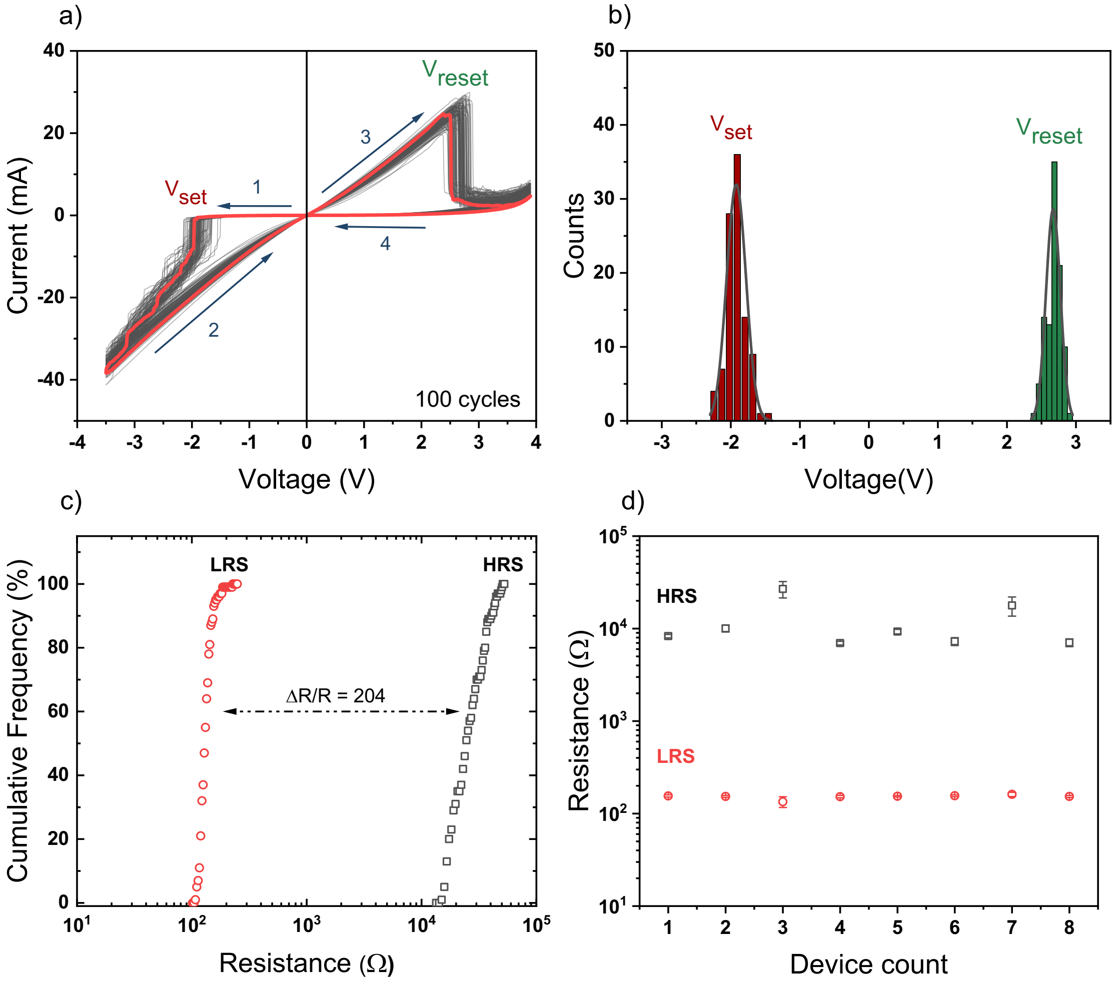

Figure 4-15: Current-voltage characteristics of the fabricated Au/$Hf_{0.5}Zr_{0.5}O_{2-\delta}$/TiN devices.

a) 100 DC sweep cycles, forming-free and self-compliant of the Au/$Hf_{0.5}Zr_{0.5}O_{2-\delta}$/TiN device. The first loop is outlined in red. b) Distribution of set and reset voltages. c) Cumulative frequency for LRS and HRS at 0.1V. d) HRS and LRS values tested over eight different memory cells.

4.3.4 Conduction mechanism through TiN/$Hf_{0.5}Zr_{0.5}O_{2-\delta}$/Au devices.

To study the dominant conduction mechanism of the TiN/$Hf_{0.5}Zr_{0.5}O_{2-\delta}$/Au devices and to understand the implications of defects in the evolution of the resistive switching process, HRS and LRS were redrawn in a log-log scale, as indicated in Figure 4-16. Experimental data for both positive and negative biases were plotted on the same axis, using the absolute values of currents and voltages. With regard to the LRS for positive and negative bias, a linear fitting with a slope of 1.014 ± 0.001 in the low-voltage region (< 0.5 V) was determined from the log(I) versus log(V) plot, as shown in Figure 4-16. A slope of ~ 1 indicates that the LRS is dominated by a lineal conduction mechanism. This indicates that the traps have been occupied by the injected charge carriers forming a conductive filament [121]. At this point, we would like to point out that the formation of a metallic gold filament cannot be entirely ruled out, even though the low porosity and considerable thickness of the film make this scenario relatively unlikely. In the case of experimental negative and positive I(V) curves for the HRS, two regions were identified; for small voltages (<0.15 V), the curve shows a linear behavior while a nonlinear region for higher voltages (>0.15 V) is observed. The slope of ~1 observed for small voltages <0.15 V, as pointed out by J.F. Scott [122], is not sufficient to establish Ohmic conduction. This linear I–V relationship can alternatively be explained by Schottky and/or Simmons' modified Schottky emission mechanisms [122]. As J.F. Scott discusses in his paper, thickness-dependent current measurements are required to distinguish between Ohmic conduction mechanisms and Simmons/Schottky mechanisms, as only the Ohmic model, given by Kirchhoff's empirical equation, depends on thickness.

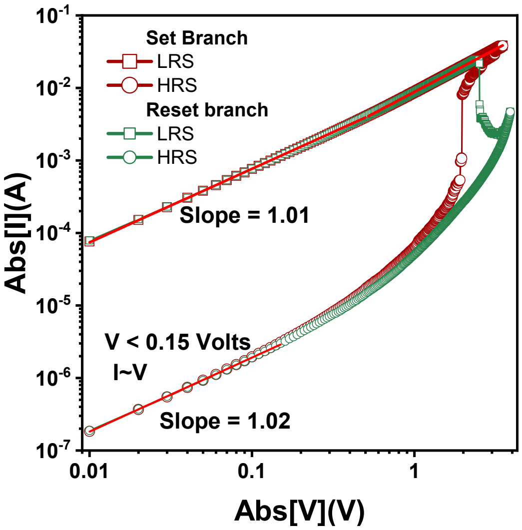

Figure 4-16: Log-log plot of typical I-V of the Au/$Hf_{0.5}Zr_{0.5}O_{2-\delta}$/TiN device.

Experimental data for both positive and negative biases were plotted on the same axis, measured at 295 K. Absolute values were applied to voltage and current.

For a higher voltage regime (slope ≠ 1), the current was modeled using various conductivity mechanisms. In this study, we consider three of the most commonly used conduction mechanisms for oxide materials: space-charge-limited conduction (SCLC) [123], Poole Frenkel [124], and Schottky emission [125, 126].

As defects, specifically oxygen vacancies embedded in the $Hf_{0.5}Zr_{0.5}O_{2-\delta}$ lattice, act as shallow traps, trapping and de-trapping provide an easy conduction pathway. Taking this into account, the first mechanism considered for fitting the HRS I–V curves is the space-charge-limited (SCLC) model, which is commonly used to explain the carrier migration process involved in resistive switching [123, 127] and is strongly related to characteristic parameters of charge traps.

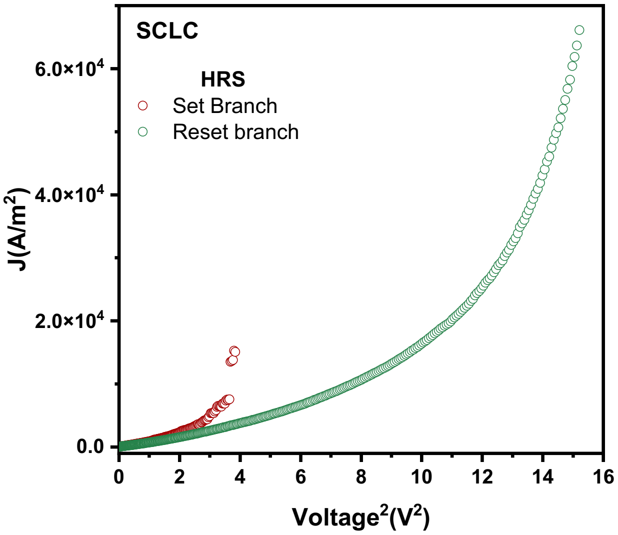

Figure 4-17: J−V^2 curve of the TiN/$Hf_{0.5}Zr_{0.5}O_{2-\delta}$/Au device.

The SCLC model does not appear to be in good agreement with the experimental data.

The model's reliability is verified by fitting the measured I–V curves. According to Equation 2-9, SCLC can be investigated by plotting the negative and positive I-V curve data as J versus V^2, as shown in Figure 4-17. The SCLC model does not appear to be in good agreement with the experimental data. As can be seen in Figure 4-17, positive and negative biases exhibited a non-linear trend. Therefore, the SCLC mechanism is not an applicable mechanism for the I-V curves of HRS.

A similar I-V plot fitting was carried out using Poole-Frenkel (

Equation 2-8) and Schottky emission (Equation 2-5) mechanisms to determine the mechanisms controlling the conduction. To investigate whether the Poole-Frenkel or Schottky emission mechanisms prevail, we plotted the I–V curves as ln(J/E) vs. $V^{1/2}$ and ln(J/T^2) vs. $V^{1/2}$, respectively, as shown in Figure 4-18. In both cases, a linear correlation was observed. To identify the dominant mechanism, the fitted value of the dielectric permittivity from the slopes of these plots was used as it is a strong indicator of whether the model produces meaningful values. As a reference, the dielectric permittivity (ε_r) reported for the monoclinic $Hf_{0.5}Zr_{0.5}O_2$ is 18 [128].

Poole-Frenkel emission (PFE) refers to the thermal emission of electrons from traps to reach the conduction band of the oxide layer. In the case of the Poole-Frenkel plot (Figure 4-18 (a)), a straight-line fit would be expected for $ln(J/E)$ versus $(V)^{1/2}$. From the Poole-Frenkel fitting slope

(Figure 4-18 (b)), an unphysical dielectric permittivity of approximately 196.7 is obtained for fields exceeding 0.25 V. The obtained ε_r value is not consistent with the value reported in the literature for the monoclinic $Hf_{0.5}Zr_{0.5}O_2$ phase, indicating that the current flow in the device does not follow the Poole-Frenkel process.

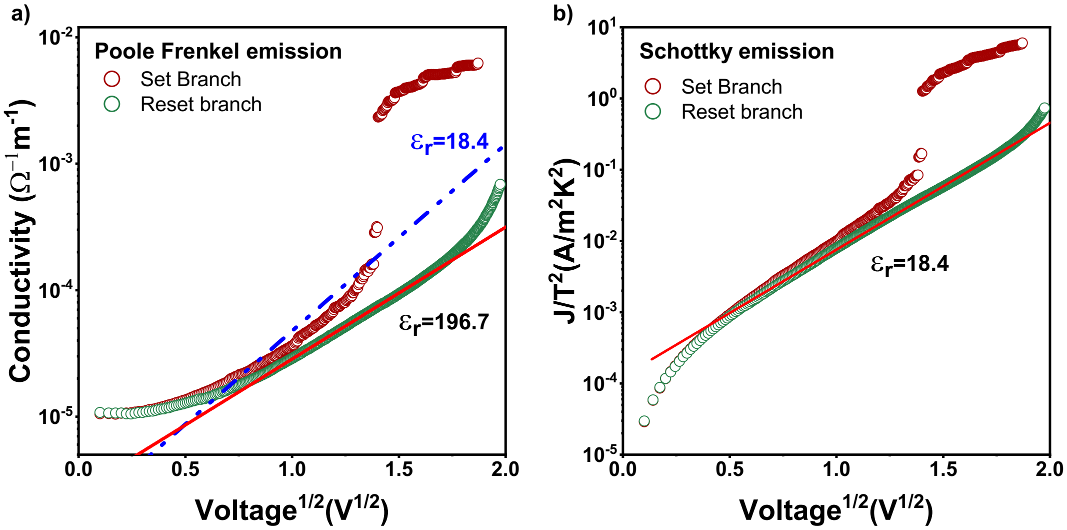

Figure 4-18: Various fits of experimental data to determine the conduction mechanism for the $Hf_{0.5}Zr_{0.5}O_{2-\delta}$ film.

a) Poole−Frenkel emission fit, and b) Schottky emission fit. The dielectric permittivity (ε_r) of 196.7, estimated from the Poole-Frenkel fit, has an unphysical meaning. The ε_r of 18.4, calculated from the Schottky emission fit, agrees with the reported value reported in the literature for the monoclinic $Hf_{0.5}Zr_{0.5}O_2$. For illustration, the Poole-Frenkel for $\varepsilon_r = 18.4$ is plotted (blue dashed line) in a).

In order to determine the dominant transport mechanism in the device, the I-V plot was also fitted using the Schottky emission mechanism. In Schottky or thermionic emission, electrons under sufficient thermal energy overcome the potential barrier at the electrode-oxide interface. The fitted result of the I-V curve in the HRS state using Schottky emission is depicted in the Figure 4-18 (b). A linear fit of ln(J/T^2) vs. V$^{1/2}$ for HRS indicates that Schottky emission is the dominant conduction mechanism. From the Schottky fitting slope (Figure 4-18 (b)), the calculated dielectric constant (ε_r) was approximately 18.4, which is in good agreement with the reported ε_r value reported in the literature [128]. Because this is the value expected for the dielectric constant, this suggests that the conduction mechanism in the device is dominated by Schottky emission [129].

4.3.5 Filament formation and breakdown

Oxygen vacancies (V$_o$), intrinsic defects, play a crucial role in resistance switching in Hf$_{0.5}$Zr$_{0.5}$O$_2$ thin films. At low oxygen concentrations, oxygen vacancies nucleate across the structure and induce a rather non-specific leakage as they migrate to or preferentially nucleate at the electrode interface. This may modulate the Schottky barrier height. Their organization into extended defects across the film into so-called oxygen vacancy filaments, however, may eventually change the nature of the conduction across the film from insulating to semiconducting or even Ohmic [130, 131]. The slope of ~1 on the LRS observed in Figure 4-16 confirms the formation of this conducting filament. The final electric properties and switching performance of the ReRAM device result from the formation of oxygen vacancies and their migration. The existence of a conductive path between the top and bottom electrodes led to the formation of a low resistive state (LRS). Reversing the polarity of the applied voltage to the top electrode causes the movement of oxygen ions, which can recombine with the oxygen vacancy. Consequently, the conductive filament will partially break down and the device returns to the HRS (Figure 4-19).

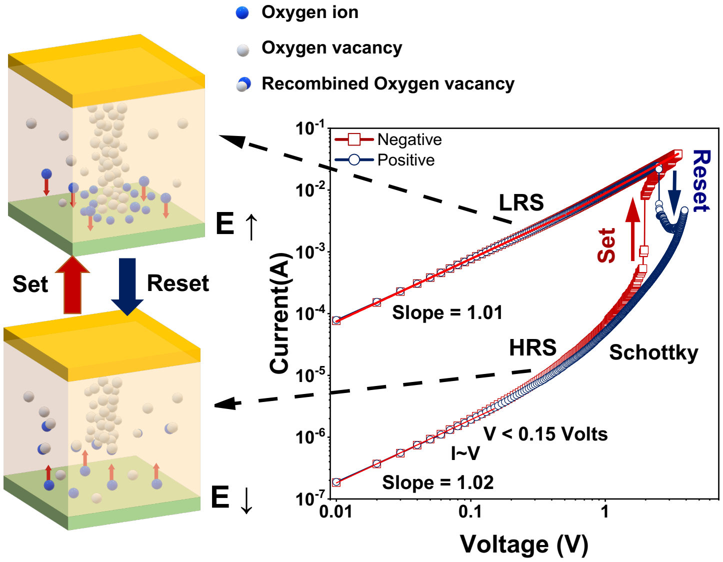

Figure 4-19: Schematic representation of the resistive switching mechanism for the TiN/Hf$_{0.5}$Zr$_{0.5}$O$_{2-\delta}$/Au devices.

The forming and soft breakdown steps are shown; a positive voltage on the top electrode causes the migration of the vacancies towards the bottom electrode until a filament gradually grows. Applying a voltage of reverse polarity changes the direction of migration of the vacancies until the filament breaks.

4.3.6 Endurance and retention test

The endurance and retention characteristics of the device were determined to further evaluate the reliability of the TiN/$Hf_{0.5}Zr_{0.5}O_{2-\delta}$/Au device. For endurance, a sequence of write/erase pulses with an amplitude of −3.5 V/+3.9 V and a width of 5 ms was applied. The HRS and LRS were read at 0.1 V, fixed as the base write/erase pulses, for 5 ms (inset in Figure 4-20(a)). The endurance of the TiN/$Hf_{0.5}Zr_{0.5}O_{2-\delta}$/Au device depicted in Figure 4-20(a) demonstrates the capability of the TiN/$Hf_{0.5}Zr_{0.5}O_{2-\delta}$/Au device to alter current pulses for 10^4 cycles under ambient conditions at room temperature. The histograms for HRS and LRS are shown in Figure 4-20(b). The LRS exhibit a mean value 162.19 Ω of with a standard deviation of 8.20 Ω, while the HRS shows a standard deviation of 0.560 KΩ and a mean value of 7.20 KΩ. No fluctuations or endurance degradation were observed even up to 10^4 pulse numbers, confirming the stability of the R_{ON}/R_{OFF} ratio. During the successive 10^4 pulse cycles, the tested sample exhibited a ratio $\Delta R/R > 4000\%$, with no degradation observed, which means that the device exceeds the basic requirement for ReRAM applications. Operation under ambient conditions without a protective atmosphere and oxygen diffusion barrier generally promotes the exchange of oxygen with the atmosphere and accelerates device degradation. With these additional precautions in place, future experiments will provide values closer to the integrated device operation.

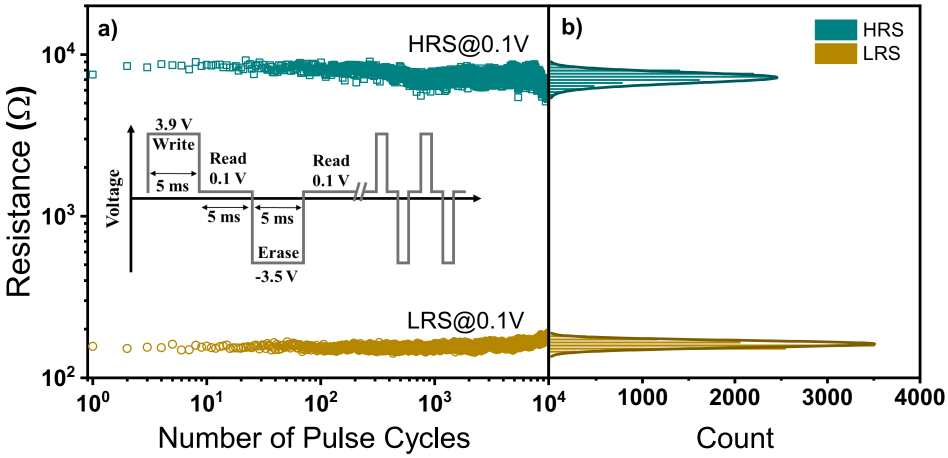

Figure 4-20: Endurance measurement on the TiN/$Hf_{0.5}Zr_{0.5}O_{2-\delta}$/Au device.

a) Resistance as a function of cycle number. b) Distribution of the ON and OFF state resistances. Resistance was measured in pulse regime at a read voltage of 0.1 V. Inset shows the sequences of pulse measurement.

The time evolution of the HRS and LRS and the retention characteristics of the device were determined, as shown in Figure 4-21. The HRS and LRS were measured with a read voltage of 0.1 V applied for 5 ms during logarithmic intervals, after applying a single −3.5 V/+3.9 V write/erase pulse.

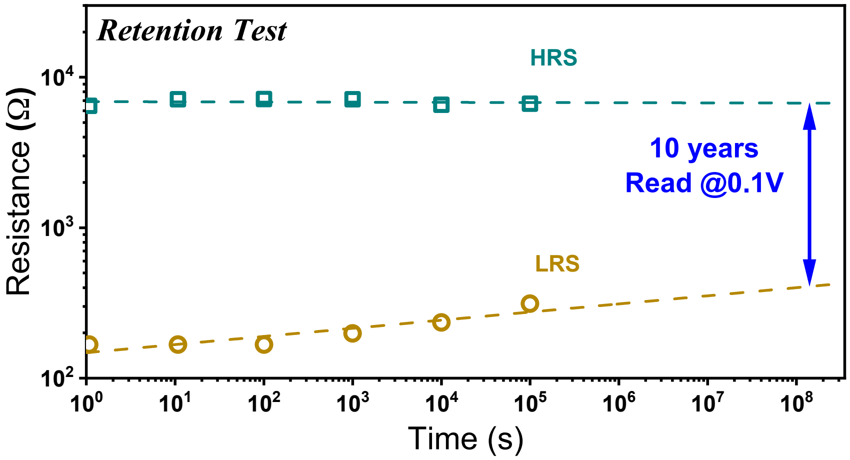

Figure 4-21: Retention measurement on on the TiN/$Hf_{0.5}Zr_{0.5}O_{2-\delta}$/Au device.

The dashed lines show an extrapolation to ten years under the assumption of a power-law dependence. Resistance was measured in pulse regime at a read voltage of 0.1 V.

Resistance values in the LRS and HRS remained constant over a long period of time (10^5 s), confirming the stability and nonvolatile nature of the device. The retention measurement indicates a degradation trend that would still preserve an order of magnitude of the ON/OFF ratio after 10 years, as illustrated in Figure 4-21, of the endurance characteristics and experimental data of the TiN/$Hf_{0.5}Zr_{0.5}O_{2-\delta}$/Au devices. These characteristics suggest a superior storage performance for the ReRAM.

4.3.7 Summary

In summary, the effect of oxygen deficiency in a $Hf_{0.5}Zr_{0.5}O_{2-\delta}$ layer on the resistive switching properties of TiN/$Hf_{0.5}Zr_{0.5}O_{2-\delta}$/Au devices for nonvolatile memory applications has been demonstrated experimentally. The current−voltage characteristics of the $Hf_{0.5}Zr_{0.5}O_2$-based device showed a Schottky emission conduction mechanism for the HRS, while ohmic conduction was observed for the LRS. The fitting of the experimental I(V) curves suggests that during the RS process from the HRS to LRS, a filamentary switching process occurs because of the formation of high oxygen vacancies across the oxide layer, which in turn leads to the RS process in the present device. We demonstrate the formation of stable and reproducible resistive switching with a high ON/OFF ratio of 10^2 up to 10^4 pulse cycles and a retention of at least 10^5 s, which can be extrapolated to 10 years, therefore validating the potential of the TiN/$Hf_{0.5}Zr_{0.5}O_{2-\delta}$/Au device for ReRAM memory applications.

5 CONCLUSION AND PERSPECTIVES

5.1 Conclusion

HfO_2-based FTJs have attracted enormous interest in the information storage field, mainly due to the performance of FTJs (high fatigue resistance, high speed, and high scalability) and the compatibility of the $Hf_{0.5}Zr_{0.5}O_2$ with CMOS technology processes. In addition, achieving spike-time-dependent-plasticity (STDP) in FTJ memory is possible, highlighting its potential for neuromorphic computing. The metastable orthorhombic phase ($Pca2_1$) is responsible for ferroelectricity in doped-HfO_2. Different pathways to stabilize this non-centrosymmetric phase include doping, strain, surface/interface/grain boundary energy, annealing temperature and intentionally introduced oxygen vacancies.

In this thesis, we have fabricated TiN/$Hf_{0.5}Zr_{0.5}O_2$/Au structures using radio frequency (RF) magnetron sputtering with a variable oxygen partial pressure during $Hf_{0.5}Zr_{0.5}O_2$ film deposition. The formation of the ferroelectric orthorhombic phase in $Hf_{0.5}Zr_{0.5}O_2$ has been investigated by two annealing methods, in situ annealing and rapid thermal annealing (RTA). The diffractograms of the samples subjected to RTA showed an increase in intensity at $2\theta = 30.8°$, corresponding to the overlapping positions of the orthorhombic (111) and tetragonal (101) peaks. Piezoresponse force microscopy (PFM) was used to elucidate between these two phases since the orthorhombic phase is the only one favourable to ferroelectricity and, therefore, the only one that will show a reversible spontaneous polarization. It corroborates the RTA process as a straightforward pathway for forming the ferroelectric orthorhombic phase ($Pca2_1$) in $Hf_{0.5}Zr_{0.5}O_2$. Furthermore, our results agree with the literature on enhancing the ferroelectric phase in $Hf_{0.5}Zr_{0.5}O_2$ films deposited under an oxygen-depleted atmosphere.

The study of tunneling through TiN/$Hf_{0.5}Zr_{0.5}O_2$/Au structures allowed us to analyze the influence of oxygen partial pressure on the tunneling mechanism. We demonstrated that $Hf_{0.5}Zr_{0.5}O_2$ deposited in an oxygen-rich atmosphere (p_{O_2}= 67%) are suitable for direct tunneling. In comparison, those obtained in a semi-oxygen-deficient atmosphere (p_{O_2}= 50%) are favourable for trap-assisted tunneling. Using the PATT model, it was possible to obtain the average distance between traps, being in the range of ~1.3 nm. The comparative analysis of the PATT and WKB models for different film thicknesses allowed us to determine the critical thicknesses at which one of the tunneling mechanisms will dominate. Likewise, comparing different trap densities (average distance between traps) allows us to determine the average distance between traps threshold for the prevalence of the tunneling mechanisms. This work, therefore, provides a window of thin film thicknesses and trap densities for an optimal FJT tunneling performance. The endurance test demonstrates the stability of direct tunneling devices over those based on trap-mediated tunneling.

For the case of $Hf_{0.5}Zr_{0.5}O_2$ deposited in a fully oxygen-depleted atmosphere (p_{O_2}= 0%) I have demonstrated that the formation of an oxygen vacancy filament is possible. We conclude that in addition to its exclusive performance in FTJs, $Hf_{0.5}Zr_{0.5}O_2$ may even be used as an oxygen valence resistive memory with the benefit of COMS compatibility and the primary demerit of high activation energies to produce and displace oxygen vacancies as compared to other valency change materials. We demonstrate the formation of stable and reproducible resistive switching with a high ON/OFF ratio of two orders of magnitude for up to 10^4 pulse cycles and retention of at least 10^5 s.

5.2 Perspectives

The influence of oxygen partial pressure during $Hf_{0.5}Zr_{0.5}O_2$ film deposition by radio frequency (RF) magnetron sputtering on the formation of the ferroelectric orthorhombic phase (*Pca2₁*) and tunneling mechanisms through the $Hf_{0.5}Zr_{0.5}O_2$ film was investigated, with promising results documented. Despite the significant progress made from synthesis to elucidation of the charge transport mechanisms, some aspects of this study require further investigation.

As we noticed above, an increase in the RTA time led to the formation of a diffraction peak corresponding to TiO_2. This could be due to the presence of O_2 in the RTA chamber. A similar effect may occur in the sputtering chamber under certain temperatures and partial oxygen pressures or via oxygen reactive sputtering in the case of susceptible metals such as titanium. An extensive investigation of the composition and chemical stability of the TiN bottom electrode, when exposed to different atmospheres and temperatures, should be carried out.

All performance tests in this work have been conducted under ambient conditions. Operation under controlled atmosphere or with oxygen diffusion barriers will provide values closer to the integrated device operation with these additional precautions.

As for the integration of FTJs into crossbar arrays, the bottom electrodes introduce a surface topography that will interfere with the operation of an FTJ that requires extremely flat surfaces. So, for crossbar arrays, any bottom electrode will have to first be embedded into a low-*k* dielectric e.g. a spin-on glass followed by a chemical-mechanical planarization step. This planarization is non-trivial for heterostructures over large areas if out-of-plane tolerances for steps need to be kept to dimensions of the thickness of tunnel junctions. In other words, a planarization step over large areas to achieve steps in the range of 1 nm at most, which is required for predictable operation of FTJs is far from obvious.

A remarkable bifurcation effect of the HRS and LRS states was observed in the endurance evolution of the samples deposited in an oxygen-rich atmosphere (p_{O_2}= 67%). This is still under investigation, with a possible link to a logistic map (negative feedback loop) associated with different ferroelectric domain populations. Such behavior would provide an opportunity to use FTJs as random number generators via chaotic cycles in the Feigenbaum diagram. Both the principle feasibility of this approach as well as the underlying mechanisms for a negative feedback look require a deeper look into the long-term switching mechanisms of ferroelectric tunnel junctions under different tunneling regimes.

6 APPENDIX A

Crystal structure and phases of Zr-doped HfO_2

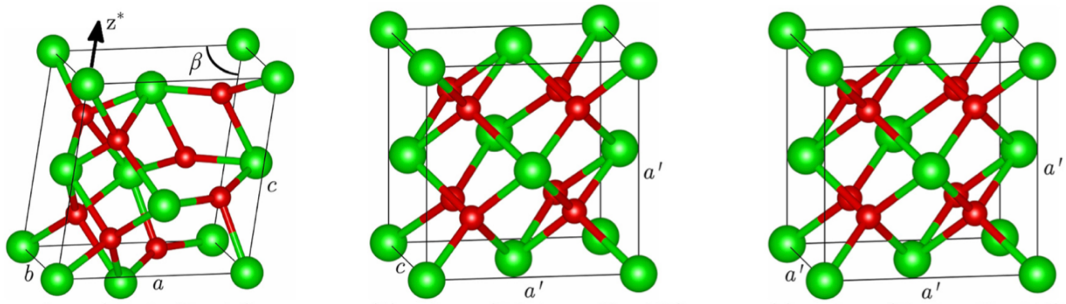

(a) m-phase ($P2_1/c$, No. 14); Exp. ZrO_2:[4] $\beta = 80°$, $a = 5.15$, $b = 5.20$, $c = 5.32$

(b) t-phase ($P4_2/nmc$, No. 137); ZrO_2 (exp.):[4] $a' = 5.09$, $c = 5.18$

(c) c-phase ($Pm3m$, No. 225); ZrO_2 (exp.):[53] $a' = 5.12$

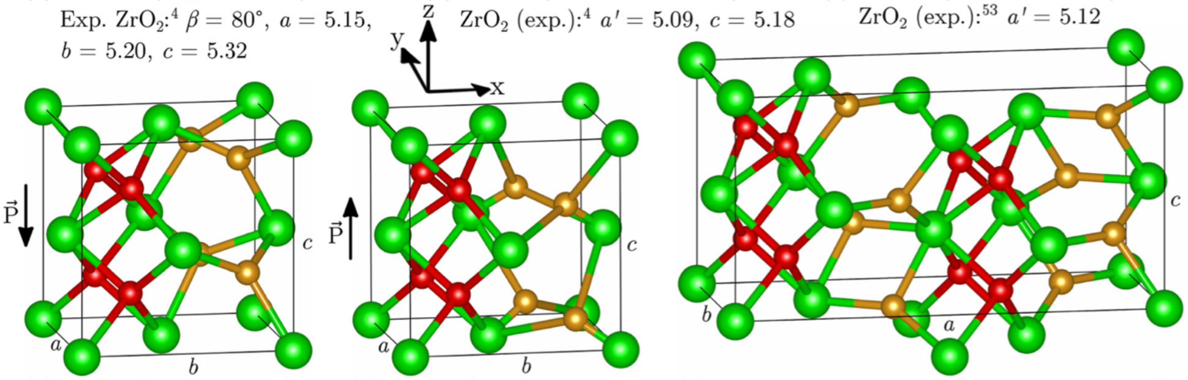

(d) f-phase ($Pca2_1$, No. 29); ZrO_2 (exp.):[5] $a = 5.07$, $b = 5.26$, $c = 5.08$

(e) f-phase ($Pca2_1$, No. 29); inversed polarization

(f) o-phase (Pbmm,mca, No. 61); ZrO_2 (exp.):[52] $a = 2\times5.04$, $b = 5.09$, $c = 5.26$

Figure: A-1: Crystal phases in Zr-doped HfO_2 films. a) monoclinic ($P2_1/c$), b) tetragonal ($P4_2/nmc$), c) cubic (Pm3m), d) orthorhombic ($Pca2_1$), and f) orthorhombic (Pbmm) phases. Zr atoms are green, and O atoms are red. Figure from [28]

EFFET DE L'OXYGÈNE SUR LE MÉCANISME DE CONDUCTION À TRAVERS LE $Hf_{0,5}Zr_{0,5}O_2$ POUR LES APPLICATIONS DE ReRAM

7.1 INTRODUCTION

La diffusion des appareils électroniques de nos jours est la conséquence des progrès extrêmement rapides de l'industrie de la microélectronique depuis les années 1970. Les efforts de l'industrie pour suivre cette tendance ont entraîné une réduction drastique des coûts de fabrication, ce qui a rendu les appareils électroniques accessibles à un plus grand nombre de personnes, tout en augmentant leur portabilité.

En même temps, ces réductions constantes de la taille des fonctionnalités répondaient à une demande en forte croissance de stockage d'informations (musique, photos, vidéos, etc.). C'est la raison pour laquelle les mémoires flash se sont imposé ces dernières années comme le type dominant de stockage de masse, allant des clés USB (*Universal Serial Bus*) aux cartes SD (*Secure Digital*) pour les appareils photo et les téléphones, en passant par les dispositifs de grande capacité tels que les SSD (*Solid-State Drive*). Les mémoires flash sont basées sur le transistor à effet de champ (à grille flottante) métal-oxyde-semiconducteur (*floating gate Metal-Oxide-Semiconductor Field-Effect Transistor* – MOSFET). Il s'agit d'un transistor à effet de champ dont le métal de la grille est totalement isolé du reste de la structure par un oxyde.

Le MOSFET est relativement peu coûteux et peut facilement suivre l'évolution générale de la technologie des semi-conducteurs. Cependant, cette technologie est inefficace sur le plan énergétique, est lente et se rapproche progressivement de ses limites physiques d'extensibilité, car le dispositif devient sensible à l'effet tunnel aux dimensions nanométriques, ce qui entraîne des pertes de charge et des courants de fuite importants [4].

En réponse à ce problème, de nouveaux concepts de mémoire non volatile ont été développés pour remplacer les MOSFETs à grille flottante. Ces concepts sont soit basés sur la charge, soit sur la résistance. Les mémoires ferroélectriques (FeRAM) sont un exemple de dispositifs basés sur les charges avec une limite critique intrinsèque, car la taille des caractéristiques diminue jusqu'à des dimensions qui ne permettent pas le stockage d'un nombre suffisant de charges pour être détectées (et amplifiées) par un transistor. Les mémoires ReRAM surmontent ce problème, car elles stockent des informations dans plusieurs états de résistance. Dans le cas d'un dispositif binaire, ces deux états de résistance représentent zéro et un. L'intégration du courant qui traverse un tel dispositif fournit les charges nécessaires pour déclencher un transistor de lecture. D'ailleurs, même un courant très faible résultant d'une résistance élevée dans un dispositif très petit peut encore produire des charges suffisantes pour des temps d'intégration suffisamment longs. En d'autres termes, la RAM résistive offre la possibilité d'un compromis entre la taille et la vitesse de lecture.

Une jonction tunnel ferroélectrique (*Ferroelectric Tunnel Junction* – FTJ) est une mémoire résistive à accès aléatoire composée de deux électrodes métalliques entourant une couche ferroélectrique (FE) ultrafine (Métal/Ferroélectrique/Métal), présentant deux états de polarisation stables à champ appliqué nul. La direction de polarisation de la couche FE peut être commutée d'un de ces états de mémoire à l'autre par un champ électrique dépassant le champ coercitif. Les charges de surface associées à la polarisation permanente induisent une modulation de la hauteur de la barrière, ce qui modifie considérablement le courant d'effet tunnel de la pile, connu sous le nom d'électrorésistance par effet tunnel (*Tunnelling Electroresistance Effect* – TER) [5].

L'effet TER dans une cellule mémoire a été démontré expérimentalement en 2009 en utilisant une couche ultrafine de $BaTiO_3$ comme barrière ferroélectrique [6, 7]. La démonstration expérimentale d'un dispositif de mémoire FTJ basé sur des matériaux pérovskites a déclenché des recherches intenses sur ses propriétés. Une grande résistance à la fatigue (endurance ~ 106 cycles) due à une opération de lecture non destructive [9], une vitesse élevée (vitesse d'écriture jusqu'à 10 ns) [10], une grande extensibilité [11] et une architecture simple [5] sont les principaux avantages de cette technologie par rapport aux mémoires Flash ou DRAM (Dynamic Random Access Memory) classiques.

Cependant, malgré les excellentes propriétés de mémoire des dispositifs FTJ, leur introduction sur le marché des semi-conducteurs a été limitée, car l'intégration des FTJ avec des couches ferroélectriques ultrafines à structure pérovskite dans la technologie de mémoire conventionnelle à base de Si (*Complementary Metal-Oxide Semiconductor* – CMOS) reste un défi pour essentiellement trois raisons: 1) la limitation du budget thermique pour les processus de « *front and back-end-of-CMOS* » puisque les pérovskites nécessitent des températures et des temps de cristallisation qui dépassent les tolérances de la technologie CMOS, 2) le manque de compatibilité de la plupart des oxydes métalliques ternaires avec le silicium. Comme Hubbard et al. [12] et Schlom et al. [13] l'ont souligné, la règle d'or pour déterminer la compatibilité d'un oxyde ternaire avec le silicium est de savoir si les oxydes binaires qui le composent sont individuellement compatibles avec le silicium, ce qui exclut par exemple les pérovskites avec un sous-réseau TiO_2 tel que $BaTiO_3$, $PbTiO_3$ et leurs dérivés $Ba_xSr_{1-x}TiO_3$ and $PbZr_xTi_{1-x}O_3$, et 3) la sensibilité de la plupart des ferroélectriques pérovskites à une atmosphère réductrice « *forming gas* », un produit chimique courant dans l'industrie des semi-conducteurs pour limiter ou inverser les effets de l'oxydation. Il y avait donc une forte demande pour un ferroélectrique compatible CMOS tout au long de l'évolution de la micro- et nanoélectronique.

La découverte de la ferroélectricité dans l'oxyde d'hafnium dopé au silicium par Böscke et al. en 2011 [14] a donc relancé l'intérêt pour les mémoires ferroélectriques à jonction tunnel. Proposé comme matériau compatible CMOS en 2002 par Gilmer et al. [15], Intel a pleinement intégré l'oxyde d'hafnium dans les processus de fabrication CMOS à partir de 2007 [16]. De plus, la ferroélectricité du HfO_2 dopé a été démontrée pour des épaisseurs inférieures à 10 nm [17], ouvrant la voie à des dispositifs de mémoire FTJ entièrement compatibles CMOS.

Le modèle de base des jonctions tunnel ferroélectriques repose sur deux états de polarisation distincts qui donnent lieu à deux états résistifs. Ces états résistifs sont communément appelés état de haute résistance (*High Resistance State* – HRS) et état de basse résistance (*Low Resistance State* – LRS) et sont associés à « *OFF* » et « *ON* », ou « 0 » et « 1 » respectivement. L'utilisation de ces termes n'est pas unifiée, mais largement cohérente dans la littérature.

Depuis 2011, une abondance d'études a été réalisée sur ce type de mémoire. Et pourtant, plusieurs défis restent à relever afin d'envisager une intégration par l'industrie.

La phase orthorhombique non centrosymétrique du groupe spatial $Pca2_1$ est largement acceptée comme responsable de la ferroélectricité dans les couches minces à base de HfO_2 [22-24]. Cependant, il s'agit d'une phase métastable. De nombreux efforts ont été entrepris pour stabiliser cette phase non centrosymétrique, y compris le réglage de propriétés telles que le dopage [25], la déformation [26], la température de recuit [29] et les lacunes d'oxygène introduites intentionnellement [30]. Néanmoins, bien que ces mécanismes améliorent les propriétés ferroélectriques des couches à base de HfO_2, ils ont également un effet adverse sur les performances d'une JFT à base de HfO_2. Pendant les premiers cycles de vie de la mémoire, les valeurs de polarisation rémanente augmentent progressivement (en valeur absolue) au fur et à mesure du cycle jusqu'à atteindre leur valeur maximale et se stabiliser. Ce phénomène est appelé « *wake-up* » et est attribué à une redistribution des lacunes d'oxygène dans le matériau [33]. Une diminution des valeurs de polarisation rémanente marque la durée de vie de la mémoire, ce qui correspond à une fatigue du matériau ferroélectrique attribuée à une augmentation du nombre de défauts générés (par exemple, des lacunes d'oxygène) dans le matériau. Ainsi, alors que l'effet des lacunes d'oxygène au stade précoce de l'inversion de la polarisation dans les dispositifs à base d'oxyde d'hafnium est bénéfique pour la polarisation rémanente, la conséquence ultime de la migration des lacunes d'oxygène entraîne une fatigue, c'est-à-dire une réduction de la polarisation réversible après de nombreux cycles.

Les lacunes d'oxygène doivent donc être considérées comme un élément clé dans la compréhension des propriétés électroniques des jonctions tunnel ferroélectriques à base de HfO_2 dopé, car elles influencent également les mécanismes de conduction dans la structure. Dans ce travail, nous étudions l'effet des lacunes d'oxygène sur le mécanisme de conduction dans les jonctions tunnel à base de $Hf_{0,5}Zr_{0,5}O_2$ et ces couches minces. Comme nous le montrerons, il est possible de passer d'une conduction tunnel directe à une PATT (*Phonon-Assisted Tunnelling between Traps*) [34], ou même plus loin à la formation de filaments de lacunes d'oxygène [35].

Une question importante résultante de toutes ces considérations est de savoir comment la compétition entre la commutation de la jonction tunnel ferroélectrique idéalisée et les mécanismes d'effet tunnel basés sur les lacunes d'oxygène affecte les possibilités de déployer ces dispositifs.

7.1.1 Objectifs de recherche

Cette thèse étudie le rôle des lacunes d'oxygène dans le mécanisme de conduction électrique à travers le $Hf_{0,5}Zr_{0,5}O_2$ déposé par pulvérisation cathodique magnétron à radiofréquence (RF) et ses applications pour la mémoire ReRAM. Ceci concerne les objectifs spécifiques suivants :

i) Stabiliser la phase ferroélectrique orthorhombique ($Pca2_1$) dans $Hf_{0,5}Zr_{0,5}O_2$ et déterminer sa dépendance à la pression partielle d'oxygène pendant la pulvérisation cathodique magnétron à radiofréquence de $Hf_{0,5}Zr_{0,5}O_2$.

ii) Fabrication de couches minces à épaisseur contrôlée de $Hf_{0,5}Zr_{0,5}O_2$ avec et sans ordre polaire. L'épaisseur doit être contrôlée avec une précision suffisante pour obtenir des couches ultraminces avec transport de charges par effet tunnel et des couches légèrement plus épaises où, par exemple, les mécanismes thermioniques prévalent. Cet objectif porte, en particulier, sur le contrôle des paramètres de dépôt pour découpler la concentration en lacunes d'oxygène de la vitesse de croissance.

iii) Identification des mécanismes dominants de transport de charges sur la base d'un modèle microscopique de mécanismes, possiblement coexistants et concurrents, à effet tunnel.

iv) Extraction des paramètres du matériau, par exemple la concentration de lacunes d'oxygène, à partir d'expériences quantitatives de transport de charges à travers des jonctions tunnel ferroélectriques.

v) Le début d'une étude sur la façon dont les lacunes d'oxygène affectent la fatigue des jonctions tunnel ferroélectriques.

7.2 CONTEXTE THÉORIQUE

7.2.1 Ferroélectricité

Dans les matériaux ferroélectriques, la polarisation spontanée est réversible sous l'effet d'un champ électrique externe et reste non nulle lorsque le champ est retiré. La ferroélectricité est un phénomène coopératif [36], c'est-à-dire que la polarisation spontanée d'une cellule unitaire interagit avec les cellules adjacentes, les orientant dans la même direction. Elle a été observée pour la première fois en 1920 par Joseph Valasek lors d'expériences sur le sel de Rochelle [37].

La Figure 7-1 montre une structure typique de matériau ferroélectrique appelée pérovskite : un ion métallique, tel que Ti ou Zr, est incorporé dans un octaèdre d'oxygène étiré dans une orientation donnée (le long de l'axe c dans le schéma). Cette déformation conduit à une position de l'ion métallique légèrement décalée par rapport au centre de l'octaèdre. Il en résulte un moment dipolaire électrique dans le réseau cristallin puisque le barycentre des charges négatives induites par les atomes d'oxygène ne coïncide plus avec l'ion métallique, qui porte les charges positives. Dans le cas des pérovskites, les atomes entourant le réseau cristallin sont également des ions métalliques (comme Pb ou Ba), mais leur participation au moment dipolaire est négligeable.

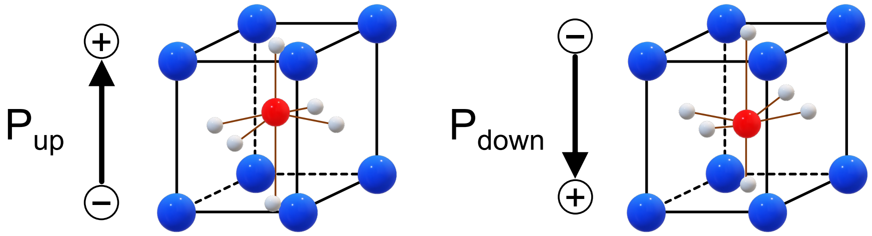

Figure 7-1: Structures atomiques des oxydes pérovskites ABO_3.

Structures atomiques des oxydes pérovskites ferroélectriques ABO3 pour la polarisation « up » et « down ». Les anions d'oxygène (gris) dans le plan horizontal de la structure subissent un petit déplacement dans la direction opposée du cation B central (rouge), fournissant ainsi un ordre à longue portée.

7.2.2 Domaines et commutation de polarisation

La définition d'un ferroélectrique peut être résumée par le cycle d'hystérésis reliant la polarisation spontanée au champ électrique appliqué (Figure 7-2). Initialement dirigée dans une direction, la polarisation bascule dans l'autre direction, c'est-à-dire que dans le cas d'une pérovskite, le cation du site B de la Figure 7-1 passe d'une position à l'autre lorsqu'un fort champ électrique est appliqué dans cette direction. Ce champ est appelé champ coercitif, noté E_c.

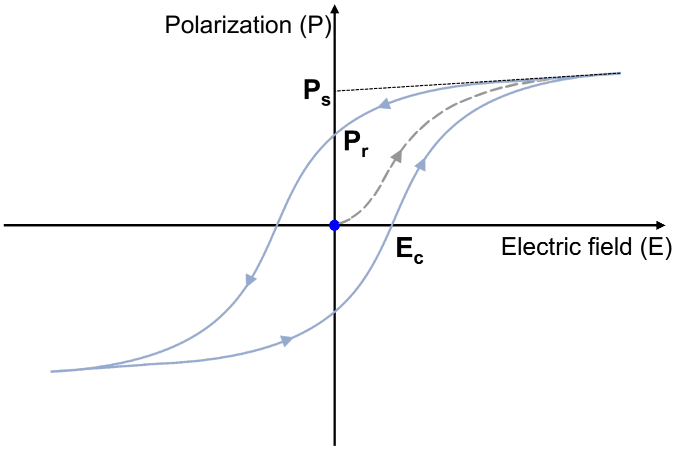

Figure 7-2: Un cycle typique d'hystérésis ferroélectrique.

La ligne pointillée illustre la transition d'un état polydomaine initial avec une polarisation globale nulle vers un état avec deux états de polarisation distincts.

Typiquement, il y a au moins deux états de polarisation possibles. Par conséquent, il existe des régions du matériau où la polarisation se trouve dans l'un ou l'autre de ces états. Ces régions sont appelées des domaines. Lorsqu'un champ électrique est appliqué, la polarisation est forcée de s'aligner sur le champ, ce qui entraîne la formation de nouveaux domaines ou un réarrangement des domaines préexistants. Une paroi de domaine sépare deux domaines de polarisation différente.

Le processus de commutation se déroule en trois étapes : nucléation hétérogène des domaines, croissance verticale rapide des domaines et croissance latérale relativement lente des domaines [39].

Dans la première étape, la formation d'un domaine commence par l'apparition d'un grain (noyaux). Cette germination se fait au niveau des sites dits de nucléation. La surface, les défauts ponctuels ou étendus, la frontière des domaines existants, ou plus généralement, toutes les inhomogénéités modulant localement le champ électrique sont autant des centres actifs diminuant l'énergie d'activation et pouvant ainsi initier la nucléation d'un domaine. Après sa formation (généralement à l'interface), le domaine croît le long de l'axe polaire en se propageant à la vitesse d'un phonon optique. Pour une couche mince d'une épaisseur de 10 nm et une vitesse du son d'environ 5000 m/s, cette étape ne prend donc que quelques picosecondes. L'extension latérale du domaine, c'est-à-dire perpendiculaire à l'axe polaire, constitue la troisième étape. La croissance latérale est beaucoup plus lente que la croissance verticale, ce qui est compréhensible puisque la direction de l'extension est perpendiculaire au champ appliqué.

7.2.3 Ferroélectricité de $Hf_{0,5}Zr_{0,5}O_2$

La phase orthorhombique non centrosymétrique (groupe spatial *Pca2₁*) a été largement reconnue comme responsable de la ferroélectricité des couches minces à base de HfO_2 [22-24]. Il s'agit d'une phase métastable et, par conséquent, elle ne figure pas dans le diagramme de phase du HfO_2 *bulk* [24, 41]. Le besoin de matériaux à haut coefficient de friction pour remplacer le SiO_2 dans le processus de mise à l'échelle de la microélectronique a déclenché l'exploration du HfO_2 à l'échelle nanométrique [43]. En 2011, Böscke et al. ont signalé pour la première fois la présence de la phase orthorhombique métastable dans les couches minces de HfO_2 dopés au Si [14]. Cette découverte a eu un effet direct, entre autres, dans le domaine des mémoires ferroélectriques, où l'incompatibilité des matériaux à base de pérovskite avec le procédé CMOS était un obstacle majeur à leur intégration dans l'électronique CMOS. Les ferroélectriques à base de HfO_2 sont entièrement compatibles avec la technologie CMOS, avec une grande extensibilité [17]. Différents mécanismes ont été étudiés pour la stabilisation de la phase orthorhombique, par exemple le dopage, la déformation, l'énergie de surface/interface/joint de grain et les lacunes d'oxygène.

À ce stade, l'auteur aimerait souligner que l'influence des lacunes d'oxygène a été étudiée principalement pour stabiliser la phase non polaire orthorhombique dans le HfO_2 dopé et non dopé. Dans ce contexte, il est toutefois important de préciser que les lacunes d’oxygène influencent le courant de fuite des couches minces ferroélectriques de HfO_2 [65, 67]. Ceci est véridique lorsque le matériau est utilisé comme condensateur ou comme dispositif à jonction tunnel, mais dans ce dernier cas, la présence de lacunes d'oxygène ne sera pas seulement une nuisance, mais plutôt un facteur de compétition pour le transport de charge global. À l'heure actuelle, il existe peu de travaux connexes sur l'influence de l'oxygène pendant le dépôt, et ce, sur les performances électroniques des dispositifs à base de HfO_2.

7.2.4 Jonctions tunnel ferroélectriques

Une jonction tunnel ferroélectrique (FTJ) est une mémoire vive résistive composée d'une couche ferroélectrique (FE) ultrafine entre deux électrodes métalliques. Elle a donc le potentiel conceptuel de combiner l'excellente résistance à la fatigue des dispositifs ferroélectriques avec la réduction de la taille et la lecture non destructive de la RAM résistive. Le concept de FTJ a été prédit pour la première fois en 1971 par Esaki et al. [77]. Pendant des décennies, les limitations technologiques et la difficulté pour les matériaux ferroélectriques d'atteindre une échelle de quelques nanomètres ont retardé la validation expérimentale du FTJ. En 2003, J. Rodriguez et al. ont observé une commutation résistive dans des jonctions ferroélectriques nanométriques, qui ne pouvait pas être directement liée à une inversion de polarisation de la couche ferroélectrique [78]. En 2009, un groupe d'auteurs a établi que l'inversion de polarisation était responsable de la commutation résistive dans les FTJs [6, 7, 79]. La direction de polarisation de la couche FE peut être commutée entre les électrodes supérieures et inférieures par un champ électrique à travers la pile. Si les électrodes sont asymétriques, cela produira une modulation de la hauteur de la barrière, comme le montre la Figure 7-3. Par conséquent, le courant d'effet tunnel (résistance) à travers la pile est considérablement modifié.

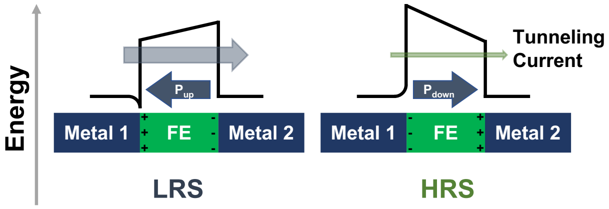

Figure 7-3: Diagramme de bande d'une jonction Métal$_1$/FE/Métal$_2$ avec différentes directions de polarisation.

Dans ce schéma, l'électrode de gauche est esquissée pour contribuer à une certaine quantité d'écrantage, tandis que l'électrode de droite est supposée être idéale. Le TiN serait un exemple approprié pour l'électrode de gauche et le platine pour l'électrode de droite.

Le processus d'écriture est réalisé en appliquant un champ électrique supérieur au champ coercitif qui inverse la polarisation. En revanche, la lecture non destructive est réalisée en détectant le courant tunnel lorsqu'un petit potentiel est appliqué, empêchant l'inversion de polarisation.

Comme son nom l'indique, l'effet tunnel est le principal mécanisme des FTJ. Cependant, des paramètres tels que la tension électrique ou l'épaisseur de la couche ferroélectrique peuvent permettre la différenciation du mécanisme de conduction dans le dispositif FTJ [82]. La section suivante traite des mécanismes de conduction les plus couramment rencontrés dans les structures métal-isolant-métal.

7.2.5 Mécanisme de conduction dans les structures métal-isolant-métal (MIM)

Les mécanismes de conduction les plus courants dans les mémoires résistives à base de MIM sont classés en deux groupes : ceux qui dépendent des propriétés de l'interface électrode-diélectrique, par exemple l'émission Schottky, l'effet tunnel Fowler-Nordheim (Fowler-Nordheim *Tunnelling* – FNT) et l'effet tunnel direct (*Direct Tunnelling* – DT), et ceux qui dépendent uniquement des propriétés du diélectrique, par exemple l'émission Poole-Frenkel (Poole-Frenkel *Emission* – PFE), la conduction ohmique, *Space-Charge-Limited Conduction* (SCLC) et l'effet tunnel assisté par un piège (*Trap-Assisted Tunnelling* – TAT).

7.3 MATÉRIELS ET MÉTHODES

7.3.1 Croissance des couches minces

Les dispositifs analysés dans cette étude consistent d’un empilement de trois couches : électrode inférieure (TiN), couche active ou couche d'oxyde ($Hf_{0,5}Zr_{0,5}O_2$) et Au comme électrode supérieure. Chacune de ces couches a été déposée séquentiellement par pulvérisation cathodique magnétron à radiofréquence (RF). Cette section décrira cette technique de dépôt, qui appartient à la famille des techniques de dépôt physique en phase vapeur, et décrira l'équipement utilisé dans cette étude. Compte tenu de la nature polycristalline de l'électrode inférieure (TiN) relativement épaisse, le substrat a peu d'importance. Nous utilisons des plaquettes de Si avec un oxyde natif sur le dessus.

7.3.2 Pulvérisation cathodique magnétron à radiofréquence (RF)

Dans le processus de pulvérisation, une surface solide (cible) est bombardée de particules énergisées (dans notre cas, principalement des ions accélérés de gaz argon ou un mélange oxygène-argon pour la couche mince et de l'azote pour l'électrode inférieure). Les collisions affectent la surface de la cible, provoquant par transfert d’impulsion l'éjection des atomes de la cible qui se déposent ensuite sur le substrat. Cette technique de dépôt est largement utilisée dans le milieu universitaire et dans la production à grande échelle. La température du substrat est souvent réglable en tant que paramètre supplémentaire du processus.

Dans la pulvérisation, la formation du plasma peut être déclenchée par une alimentation en courant continu (CC) ou en radiofréquence (RF). La pulvérisation en courant continu fonctionne très bien pour les matériaux conducteurs. Alors que pour les matériaux isolants, la polarisation CC provoque une accumulation de charges sur la surface de la cible. Cette accumulation de charge pendant le bombardement ionique est une source d'hétérogénéité de dépôt et d'instabilité du plasma [91]. Alors que, dans le cas de la pulvérisation par radiofréquence (RF), il est possible de déposer des matériaux conducteurs, isolants ou semi-conducteurs.

La cible du magnétron a pour effet d'augmenter la vitesse de dépôt. Son rôle est de confiner les électrons secondaires, émis sous l'effet de l'impact des ions, à proximité de la cible pour augmenter la densité ionique de la zone plasma. Cette technique permet également de fonctionner à des pressions de gaz plus faibles, ce qui augmente le libre parcours moyen des particules. En général, le transfert de quantité de mouvement entre le gaz de traitement et la cible permet d'obtenir des énergies de particules de plusieurs électrons-volts équivalant à des dizaines de milliers de Kelvin d'énergie thermique.

Dans le cas où, par exemple, un des éléments constituant la cible est volatil, il peut être emporté lors du pompage, et la recombinaison des atomes éjectés ne permet pas d'obtenir le matériau d'origine. Il est alors nécessaire d'utiliser un gaz réactif lors de la pulvérisation (oxygène dans le cas des oxydes, azote dans le cas des nitrites ou sulfure d'hydrogène dans le cas des sulfures) afin d'éviter que la couche mince soit déficiente en cet élément. Le rôle du gaz réactif est triple :

- Rétablir la stœchiométrie de surface de la cible.
- Favoriser la recombinaison des ions, des atomes et des molécules lors du transfert cible-substrat.
- Restaurer la composition de la couche mince ou la modifier par rapport au matériau de la cible.

7.3.3 Fabrication de condensateurs Ti/$Hf_{0,5}Zr_{0,5}O_2$/Au à deux bornes

Des condensateurs Ti/$Hf_{0,5}Zr_{0,5}O_2$/Au à deux bornes ont été conçus pour cette étude. Les échantillons ont été fabriqués sur des substrats de Si de type p (100) par pulvérisation cathodique magnétron à radiofréquence (RF) (système sur table SPT310 de Plasmionique Inc.). Avant chaque dépôt, la chambre est évacuée à l'aide d'une pompe à vide mécanique puis d'une pompe à vide turbomoléculaire pour atteindre une pression de base inférieure à 10^{-5} Torr. L'électrode inférieure en TiN et les couches minces d'oxyde à base de $Hf_{0,5}Zr_{0,5}O_2$ ont été déposés sur un substrat Si/SiO_2 nettoyé de 0,5 cm x 0,5 cm de manière séquentielle sans rompre le vide de la chambre de pulvérisation. Le TiN a été pulvérisé à partir d'une cible métallique sur le substrat à une température de 650°C pendant 30 minutes avec une puissance de 100 watts à une pression de 5 mTorr sous une atmosphère d'azote. Un disque céramique polycristallin et stœchiométrique en $Hf_{0,5}Zr_{0,5}O_2$ a été utilisé comme cible de pulvérisation pour les couches ferroélectriques. Le $Hf_{0,5}Zr_{0,5}O_2$ a été pulvérisé sur le substrat de TiN à une température de 600°C, avec une puissance de 20 watts pendant 30 minutes à une pression de 5 mTorr sous un mélange de Ar:O_2. La pression partielle d'oxygène dans le mélange a varié pour chaque échantillon. Les électrodes supérieures en Au ont été déposées à l'aide d'un masque avec des trous circulaires d'un diamètre de 300 µm, ce qui a donné des électrodes avec une surface de contact de $A = 7,1\times10^{-4}$ cm^2. Le dépôt a été réalisé à température ambiante en utilisant une cible Au pendant cinq minutes, une puissance de 20 watts et une pression de 6 mTorr avec un débit d'Argon de 8 SCCM.

7.3.4 Diffraction des rayons X

Les rayons X d'une longueur d'onde d'environ 0,1 nm ont la particularité de pénétrer profondément dans le matériau et d'interagir élastiquement avec les électrons qui le composent sans modifier les propriétés du matériau. Les techniques qui utilisent les rayons X sont non-destructives et fournissent des informations sur la structure des couches minces et les propriétés des matériaux qui les composent.

Cette thèse traite de deux méthodes utilisées pour caractériser les couches obtenues par pulvérisation cathodique magnétron à RF : La réflectivité des rayons X (*X-Ray Reflectivity* - XRR) et la diffraction des rayons X en incidence rasante (*Grazing Incidence X-Ray Diffraction* - GIXRD). La réflectivité des rayons X nous permet de déterminer quantitativement le profil de densité électronique d'un matériau. Nous pouvons extraire des informations sur la densité, l'épaisseur des couches, ainsi que sur la rugosité de celles-ci ou à l'interface entre plusieurs couches.

La diffraction des rayons X en incidence rasante apporte des informations sur la structure cristalline des matériaux et permet d'identifier l'arrangement atomique. Nous ne développerons que le principe essentiel de cette technique.

7.3.5 PANalytical X'Pert Pro

L'équipement utilisé au cours de cette thèse, tant pour les mesures de réflectivité que de diffraction, est le X'PERT PRO from PANalytical. La source de rayons X provient de la raie Kα du cuivre ($\lambda_{CuK\alpha} = 1.5418\ \text{Å}$).

Dans le cas d'une mesure XRR, nous ajoutons une fente de 1/2° après la source et une fente de 0,18 mm avant le détecteur.

Pour une mesure GIXRD, nous ajoutons seulement une fente de 1/8° à la source.

7.3.6 Microscopie à force atomique

La microscopie à force atomique (*Atomic force microscopy* - AFM) est une technique largement utilisée pour étudier et explorer la topographie, la morphologie, la mesure de la force et la manipulation des propriétés physiques et chimiques de surface d'échantillons cristallins, semi-cristallins ou amorphes dans le vide, dans l'air et même dans des milieux liquides [95].

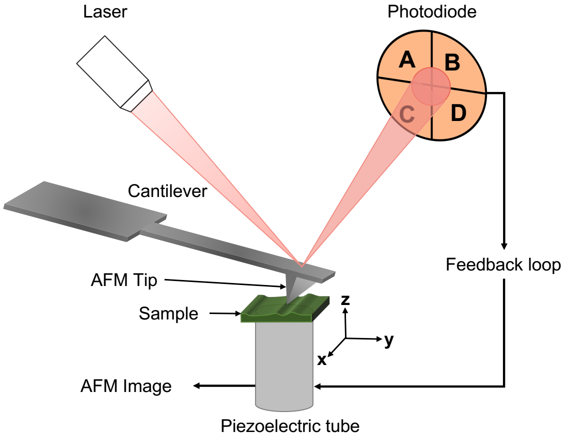

Figure 7-4: Principe de fonctionnement de l'AFM.

Un faisceau laser détecte les mouvements du levier flexible (*cantilever*), qui le réfléchit vers une photodiode. Une boucle de rétroaction maintient constante la position verticale du levier flexible (*cantilever*) en agissant sur le cylindre piézoélectrique dont les variations de tension électrique sont utilisées pour construire les images.

Une pointe ayant un petit rayon de courbure et montée sur un levier flexible (*cantilever*) est mise en contact avec une surface où la force de contact fait plier le levier flexible (*cantilever*). Un système optique composé d'un laser focalisé sur l'extrémité du levier flexible (*cantilever*) et d'une photodiode à quatre quadrants mesure la position de la réflexion du laser. De cette position, on déduit la courbure du levier flexible (*cantilever*) et, par conséquent, la hauteur de la surface en contact. En balayant la pointe de la surface, la variation de la topographie de l'échantillon peut être mesurée par la courbure (ou la déviation) du levier flexible (*cantilever*) due à la réflexion laser. En ajoutant un système piézoélectrique pour contrôler la hauteur de la pointe ou de l'échantillon, et une boucle de rétroaction sur le signal du détecteur à quatre quadrants, il est possible de suivre la variation de la hauteur de l'échantillon en maintenant constante la force pointe/surface (Figure 7-4).

Ce premier mode de contact a été suivi par des modes dits « dynamiques », dont le premier a été proposé par Martin et al. en 1987 [96]. Ce mode de contact dit intermittent, également connu sous le nom de *tapping mode* ou modulation d'amplitude, a été suivi d'un second mode inventé par Albrecht en 1991 [97] appelé mode non-contact (ou modulation de fréquence).

7.3.7 SmartSPM1000

Dans cette thèse, nous avons utilisé un microscope à force atomique SmartSPM1000 de AIST-NT Inc. pour étudier la morphologie de surface des couches minces synthétisées. L'AFM a fonctionné en mode semi-contact avec une fréquence de balayage de 0.5 Hz en utilisant des sondes AFM MikroMash (Si) avec un rayon de pointe de ~8 nm, une fréquence de résonance nominale de 325 kHz et une constante de ressort nominale de 40 N/m.

7.3.8 Caractérisation électrique

Une unité de source/mesure (*Source/Measurement Unit* - SMU) Keysight B2901A a été utilisée pour la caractérisation électrique des dispositifs TiN/$Hf_{0,5}Zr_{0,5}O_2$/Au. La connexion électrique avec les cellules de mémoire a été effectuée en utilisant des sondes en tungstène (avec un rayon de pointe de 12 µm) couplées à deux micromanipulateurs. La station de sonde est écrantée dans une cage de Faraday.

Ce dispositif expérimental a permis de réaliser la caractérisation du balayage de tension quasi statique, la réponse à l'excitation par impulsions, ainsi que des tests de rétention et d'endurance des cellules de mémoire.

7.4 RÉSULTATS ET DISCUSSION

7.4.1 Phase orthorhombique de $Hf_{0,5}Zr_{0,5}O_2$

Comme évoqué tout au long de ce document, la stabilisation de la face polaire ferroélectrique dans $Hf_{0,5}Zr_{0,5}O_2$ est un processus complexe. Dans cette section, nous allons discuter des effets de deux méthodes de recuit sur la formation de la phase ferroélectrique orthorhombique ($Pca2_1$), le recuit in situ et le recuit thermique rapide (*Rapid Thermal Annealing* - RTA). Les diffractogrammes d'échantillons de différentes épaisseurs soumis à ces deux procédés thermiques ont été analysés. La Figure 7-5 montre l'intervalle 2θ où sont situés les pics les plus distinctifs des faces monoclinique ($P21/c$) à 28,5° (-111) et 31,8° (111), orthorhombique ($Pca2_1$) à 30,8° (111) et tétragonale ($P4_2/\mathrm{nmc}$) à 30,8° (101). Comme on peut l'observer sur la figure, l'échantillon déposé pendant 30 minutes à une température de 550 °C présente une contribution majoritaire de la phase monoclinique, avec une contribution négligeable ou nulle des phases orthorhombique/tétragonale. En revanche, les échantillons soumis à un recuit thermique rapide (RTA) pendant 60 secondes à une température de 750 °C ont montré une augmentation de l'intensité des phases orthorhombique/tétragonale. Le chevauchement des positions des pics (111) et (101) correspondant aux phases orthorhombique et tétragonale, respectivement, rend difficile, voire impossible, de les distinguer.

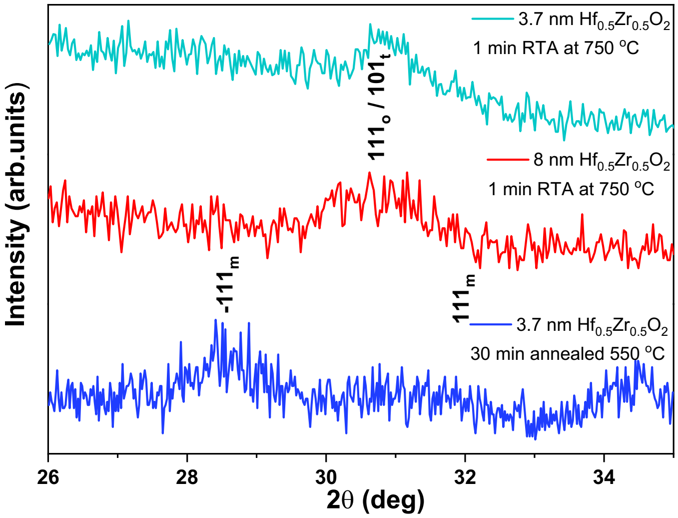

Figure 7-5: Diffractogrammes d'échantillons de différentes épaisseurs soumis à des processus thermiques in-situ et RTA.

L'intervalle montre les pics les plus distinctifs des phases monoclinique ($P2_1/c$) à 28,5° (-111) et 31,8° (111), orthorhombique ($Pca2_1$) à 30,8° (111) et tétragonale ($P4_2/\mathrm{nmc}$) à 30,8° (101).

Afin de discriminer les phases orthorhombique et tétragonale, un échantillon de $Hf_{0,5}Zr_{0,5}O_2$ d'une épaisseur de 3,7 nm soumis à la RTA a été étudié par microscopie à force piézoélectrique (*Piezoresponse Force Microscopy* - PFM). Une zone carrée de 1 µm × 1 µm sur la surface nue de la couche de $Hf_{0,5}Zr_{0,5}O_2$ a été cartographiée avec une tension électrique constante au niveau de la pointe (-2V). Par la suite, un carré rétréci de 0,5 µm × 0,5 µm a été cartographié avec une tension électrique constante de polarité opposée à la pointe (+2V). En conséquence, sur la Figure 7-6, un contraste de phase de ~180° peut être distingué entre les deux régions carrées inscrites à -2V et +2V dans une carte de phase de 2 µm × 2 µm. La zone vierge entourant le carré externe a montré une polarisation spontanée préférentielle « *down* ». La ligne sombre observée dans la carte d'amplitude (Figure 7-6) à la frontière entre les régions polarisées de manière opposée est communément attribuée aux parois de domaine [101].

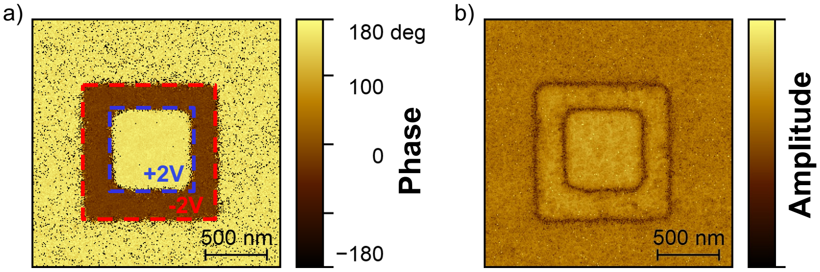

Figure 7-6: Phase et amplitude de la PFM obtenues sur une couche mince de $Hf_{0,5}Zr_{0,5}O_2$ exposé à des processus thermiques de type RTA.

a) phase, b) amplitude, obtenues sur une couche mince $Hf_{0,5}Zr_{0,5}O_2$ de 3,7 nm d'épaisseur exposé à des processus thermiques RTA.

Les mesures PFM montrent une polarisation réversible constante dans la couche ultramince de $Hf_{0,5}Zr_{0,5}O_2$, couplée à la présence du pic de diffraction correspondant à la phase orthorhombique/tétragonale, indiquant que le recuit des films ultraminces de $Hf_{0,5}Zr_{0,5}O_2$ par RTA est une voie directe pour la formation de la phase orthorhombique ferroélectrique ($Pca2_1$).

7.4.2 $Hf_{0,5}Zr_{0,5}O_2$ en fonction des pressions partielles d'oxygène

Cette section étudie l'influence de la pression partielle d'oxygène sur la vitesse de dépôt de $Hf_{0,5}Zr_{0,5}O_2$ dans la pulvérisation magnétron à RF. La pression partielle d'oxygène a été manipulée en modifiant le rapport Ar:O_2 dans la chambre de pulvérisation. Le changement de rapport est nécessaire pour fournir différentes pressions partielles d'oxygène à l'intérieur de la chambre et, par conséquent, différents potentiels chimiques qui affecteront en retour la concentration de lacunes d'oxygène à l'intérieur de la couche mince. En même temps, le rendement de pulvérisation de l'argon et de l'oxygène est différent. Sur la base du transfert d'impulsion pour expulser les atomes de la cible, l'argon est sensiblement plus efficace que l'oxygène, de sorte que le changement de composition du gaz de traitement, même pour une pression totale de fonctionnement équivalente, entraînera des taux de pulvérisation très différents. Une fois que les différentes vitesses de dépôt sont établies, l'épaisseur globale de la couche mince peut à nouveau être déterminée par un choix approprié du temps de dépôt.

L'épaisseur des couches obtenues pour les différentes pressions partielles d'oxygène a été déterminée par XRR. Les spectres XRR pour cinq échantillons de $Hf_{0,5}Zr_{0,5}O_2$ déposés pendant 30 minutes à une puissance de 20 W et une température de substrat de 600 °C avec différentes pressions partielles d'oxygène sont présentés dans la Figure 7-7 (a). La dépendance de l'épaisseur de la couche de $Hf_{0,5}Zr_{0,5}O_2$ par rapport à la pression partielle d'oxygène est représentée sur la Figure 7-7 (b).

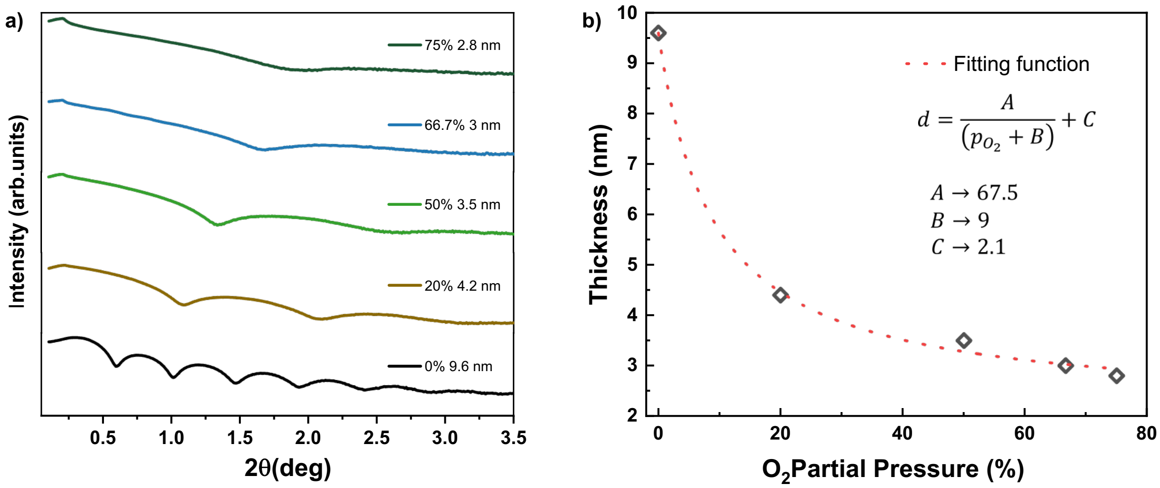

Figure 7-7: Analyse de l'épaisseur des couches minces de $Hf_{0,5}Zr_{0,5}O_2$ déposés à différentes pressions partielles d'oxygène.

a) Spectres XRR mesurés sur des couches minces à base de $Hf_{0,5}Zr_{0,5}O_2$ déposés en utilisant différentes pressions partielles d'O_2 pendant le processus de pulvérisation. b) Variation de l'épaisseur des couches minces à base de $Hf_{0,5}Zr_{0,5}O_2$ en fonction de la pression partielle d'O_2 dans la chambre de pulvérisation. La courbe rouge pointillée est un ajustement numérique.

Des rendements différents de pulvérisation d'Ar et d'O_2 produiront des vitesses de dépôt différentes pour chaque p_{O_2} et, par conséquent, une variation de l'épaisseur des couches minces de $Hf_{0,5}Zr_{0,5}O_2$ pulvérisés. L'épaisseur de la couche mince $Hf_{0,5}Zr_{0,5}O_2$ a montré une dépendance inversement proportionnelle à la pression partielle d'oxygène pendant le dépôt, comme on peut le voir sur la Figure 7-7 (b). Comme prévu, les paramètres *A*, *B* et *C* ont été trouvés à partir de l'ajustement avec l'équation $d = C + A/(P_{O_2} + B)$ où d est l'épaisseur de la couche mince déposée et p_{O_2} est la pression partielle d'oxygène pendant le dépôt.

La pression partielle d'oxygène dans le processus de pulvérisation de la couche mince $Hf_{0,5}Zr_{0,5}O_2$ a également influencé le post recuit (RTA) des couches minces $Hf_{0,5}Zr_{0,5}O_2$. Trois échantillons obtenus à des pressions partielles d'oxygène différentes ont été soumis à un RTA pendant 60 secondes à une température de 750 °C. Les diffractogrammes obtenus en configuration GIXRD pour ces échantillons sont représentés dans la Figure 7-8.

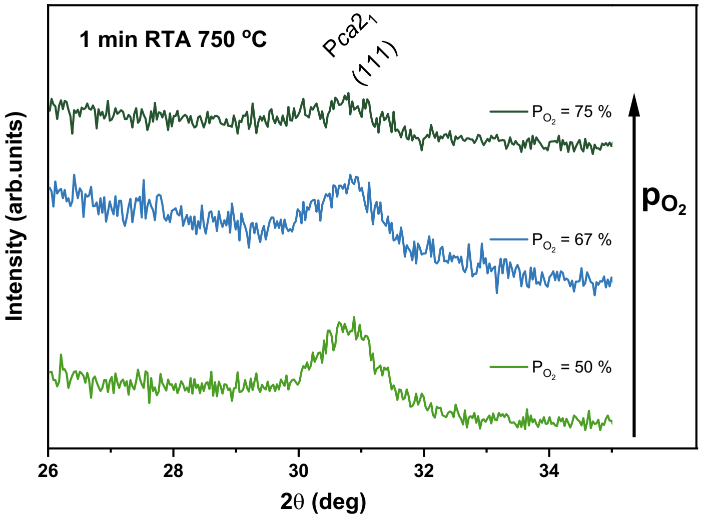

Figure 7-8: Diffractogrammes des échantillons pulvérisés sous différentes pressions partielles d'O_2 soumis à la RTA.

L'intensité du pic de diffraction augmente avec la diminution de la pression partielle d'oxygène pendant la pulvérisation. Ce résultat est en bon accord avec les observations de Monica et al. indiquant qu'une couche mince de $Hf_{0,5}Zr_{0,5}O_2$ déficient en oxygène favorise l'apparition de la phase ferroélectrique orthorhombique [30].

Une couche mince de $Hf_{0,5}Zr_{0,5}O_2$ homogène avec une portion majoritaire de la phase orthorhombique est une condition cruciale pour la fonctionnalité des FTJs à base de $Hf_{0,5}Zr_{0,5}O_2$. Cependant, l'obtention de cette phase orthorhombique via l'induction de lacunes d'oxygène aura un effet adverse sur le courant de fuite du dispositif. Une étude de l'influence de la pression partielle d'oxygène sur les mécanismes de conduction à travers le TiN/$Hf_{0,5}Zr_{0,5}O_2$/Au est présentée dans la section suivante.

7.4.3 Mécanismes concurrents de conduction par effet tunnel dans le $Hf_{0,5}Zr_{0,5}O_2$ déficient en oxygène

7.4.4 Caractérisation électrique

La caractérisation électrique de deux structures TiN/$Hf_{0,5}Zr_{0,5}O_2$/Au déposées sous p_{O_2}= 50% (3,5 nm) et p_{O_2}= 67% (3 nm) a été réalisée en les soumettant à des cycles tension électrique-courant. Notamment, la caractéristique I-V montre un changement significatif avec la variation de la pression partielle d'oxygène et de l'épaisseur des couches de $Hf_{0,5}Zr_{0,5}O_2$, comme le montre la Figure 4-8 (a) et (b). L'étendue des valeurs du courant de l'effet tunnel pour les couches minces de $Hf_{0,5}Zr_{0,5}O_2$ de 3,5 et 3 nm d'épaisseur dépendent exponentiellement de l'épaisseur de la couche mince. L'influence de l'épaisseur du diélectrique est donc cruciale pour le fonctionnement du dispositif.

7.4.5 Mécanismes à effet tunnel à travers les dispositifs TiN/$Hf_{0,5}Zr_{0,5}O_2$/Au

Différents mécanismes de conduction ont été proposés pour décrire le courant par effet tunnel, en fonction des champs électriques des dispositifs à jonction tunnel, notamment l'effet tunnel direct, l'effet tunnel Fowler-Nordheim et l'injection thermoionique [82]. En général, pour de petites épaisseurs et de faibles champs électriques, lorsque l'épaisseur de la barrière est ultramince (typiquement moins de 4 nm), les électrons peuvent traverser par effet tunnel une barrière trapézoïdale, et l'effet tunnel direct devient le mécanisme de conduction déterminant. Par conséquent, les propriétés de transport des hétérojonctions TiN/$Hf_{0,5}Zr_{0,5}O_2$/Au fabriquées à l'aide de $Hf_{0,5}Zr_{0,5}O_2$ de 3 nm d'épaisseur (p_{O_2}= 67%) ont d'abord été étudiées en utilisant un mécanisme d'effet tunnel direct.

La densité de courant à effet tunnel (J) pour l'effet tunnel direct peut être calculée en utilisant l'approximation de Wentzel Kramers-Brillouin (WKB) décrite dans l'équation 2-6.

Deux états de résistance différents sont présents dans la courbe I-V de l'échantillon de 3 nm (p_{O_2}= 67%), l'état de haute résistance (HRS) et l'état de basse résistance (LRS). Comme le montre la figure 4-8 (a), ces états ont été modélisés à l'aide de l'équation 2-6 avec les barrières de potentiel Φ_1 et Φ_2 aux interfaces des électrodes rapportées dans la littérature (voir tableau 4-4) [104] et une masse effective de $m^* = 0{,}49m_0$ déterminée à partir de nos résultats expérimentaux. Pour des tensions électriques allant de -1 à 0,5 V, on peut remarquer que le courant calculé à partir de l'équation 2-6 pour le HRS est en bon accord avec la mesure expérimentale. En revanche, l'écart entre le modèle et les mesures expérimentales pour le LRS est attribué à la part négligeable de la phase polaire dans le dispositif.

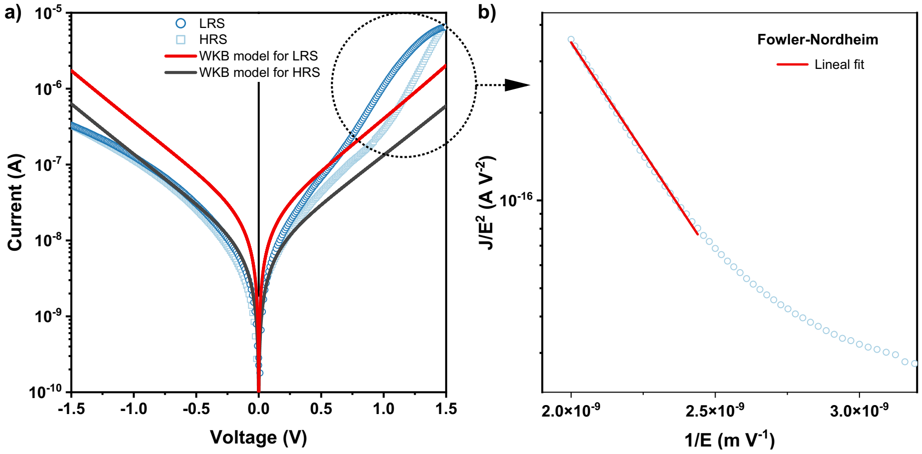

Figure 7-9: Deux effets tunnel du dispositif TiN/$Hf_{0,5}Zr_{0,5}O_2$/Au.

Courbes I-V expérimentales (symboles) et d'ajustement (solide) pour l'état de faible résistivité (LRS) et l'état de haute résistivité (HRS) du dispositif TiN/$Hf_{0,5}Zr_{0,5}O_2$/Au déposé en utilisant p_{O_2}= 67%. a) Comportement I-V dans le HRS et le LRS selon l'approximation WKB pour la région à faible champ. b) Tracé d'ajustement de Fowler-Nordheim pour la région à haut champ.

À une tension élevée, le modèle WKB ne décrit plus avec précision la réponse du courant dans l'échantillon. Dans cet intervalle, comme prévu, l'effet tunnel de Fowler-Nordheim (FNT) décrit le transport des électrons pour des barrières plus épaisses et des champs électriques relativement importants. Lorsque la tension électrique appliquée (V) dépasse la hauteur de la barrière, les électrons traversent par effet tunnel une barrière triangulaire effective qui constitue l'effet tunnel de Fowler-Nordheim (Figure 2-17). Selon l'équation 2-7, les caractéristiques J-E du courant à effet tunnel pour le mécanisme d'effet tunnel de Fowler-Nordheim (FNT) devraient satisfaire la relation de fonction linéaire entre $\ln(J/E^2)$ et 1/E. L'ajustement obtenu suggère que le mécanisme d'effet tunnel de Fowler-Nordheim fournit une excellente description, comme le montre la Figure 7-9(b).

Notre prochaine étape consiste à appliquer la même procédure à l'échantillon obtenu avec une pression partielle de 50% afin de déterminer l'effet de la pression partielle d'oxygène sur le mécanisme de transport dans $Hf_{0,5}Zr_{0,5}O_2$. En d'autres termes, confirmer la corrélation entre les courants d'effet tunnel et les lacunes d'oxygène. La figure 4-6 présente une comparaison entre la caractéristique I-V expérimentale de l'échantillon de 3,5 nm (p_{O_2}= 50%) (symboles) ainsi que les modèles WKB (ligne pointillée) et PATT (ligne pleine). Le courant pour le HRS et le LRS selon l'approximation WKB a été calculé en utilisant les paramètres indiqués dans le tableau 4-4. Les valeurs de courant mesurées dans l'échantillon sont d'un ordre de grandeur supérieur à celui calculé en utilisant l'approximation WKB (équation 2-6) avec les paramètres appropriés, ce qui suggère la présence d'un second mécanisme de conduction. La réduction de la pression partielle d'oxygène de 67 à 50 % pendant le dépôt de $Hf_{0,5}Zr_{0,5}O_2$ a entraîné un changement des conductivités HRS et LRS.

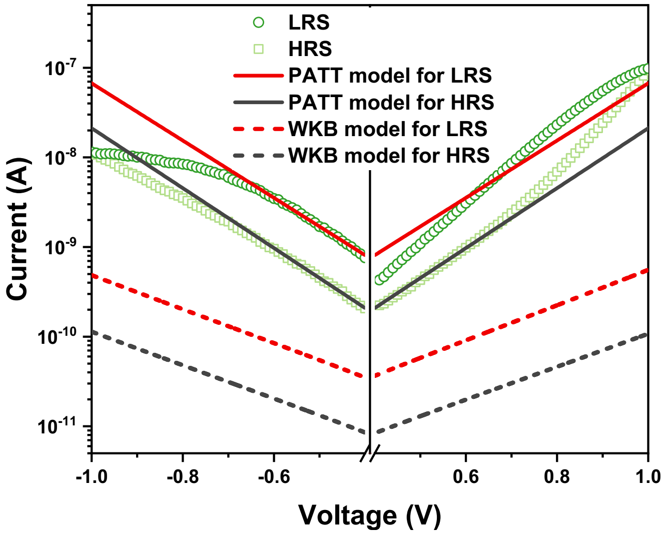

Figure 7-10: Courbes I-V expérimentales et modélisées pour le LRS et le HRS du dispositif TiN/$Hf_{0,5}Zr_{0,5}O_2$/Au avec $Hf_{0,5}Zr_{0,5}O_2$ déposé en une pression partielle d'oxygène de 50 %.

Les lignes pleines correspondent au modèle PATT et les lignes pointillées au modèle WKB.

Pour décrire ce transport et déterminer la distance entre les pièges, nous avons utilisé le modèle PATT (*Phonon-assisted Tunnelling Between Traps*) (Figure 2-19), qui a été initialement développé par Makram-Ebeid et Lannoo [105]. Il a été démontré que ce modèle de transport offre une description précise des propriétés électriques du $Hf_{0,5}Zr_{0,5}O_2$ ferroélectrique et non ferroélectrique [90].

Le modèle basé sur le mécanisme PATT (équation 2-8) est représenté sur la Figure 7-10. Le HRS (ligne continue noire) et le LRS (ligne continue rouge) sont évalués en utilisant les paramètres indiqués dans le tableau 4-4 et pour une épaisseur de $d = 3.5\ nm$. Le résultat indique un bon accord quantitatif entre le modèle PATT et les courbes I-V. La masse effective obtenue $m^* = 0.33m_0$ est en bon accord avec la valeur de la masse effective tunnel rapportée précédemment dans la littérature pour ce matériau [90, 106]. La distance moyenne entre les pièges de 1,39 et 1,27 nm a été déterminée par l'ajustement des mesures HRS et LRS, respectivement. Même si elles n'ont pas pu être corroborées indépendamment jusqu'à présent, ces valeurs sont proches du seuil expérimental significatif, soit de la moitié de l'épaisseur.

7.4.6 Effet tunnel direct ou assisté par pièges

Afin d'évaluer quel mécanisme, soit l'effet tunnel direct ou assisté par pièges, prévaut, nous examinons maintenant l'effet de l'épaisseur de la couche de $Hf_{0,5}Zr_{0,5}O_2$ et de la distance entre les pièges. La Figure 7-11(a) montre les densités de courant résultant des mécanismes de conduction DT et PATT en fonction de la distance moyenne entre les pièges pour une tension électrique fixe de 0,5 V et pour une épaisseur de couche de $Hf_{0,5}Zr_{0,5}O_2$ de 3,5 nm. La Figure 7-11(b) montre les densités de courant résultant des mécanismes de conduction DT et PATT en fonction de l'épaisseur de $Hf_{0,5}Zr_{0,5}O_2$ pour une tension électrique fixe de 0.5 V et une distance moyenne entre les pièges de 1,5 nm. Dans les deux cas, les barrières de potentiel pour l'état de polarisation HRS ont été utilisées dans l'approximation WKB. La densité de courant par effet tunnel direct est approximativement indépendante de la distance entre les pièges, comme le montre la Figure 7-11(a). En revanche, la densité de courant pour le tunnel assisté par pièges dépend de manière exponentielle de la distance moyenne entre les pièges. Par conséquent, pour de petites distances interpièges, la contribution du courant assisté par pièges sera significativement plus importante que le courant direct par effet tunnel, comme nous l'avons démontré expérimentalement pour l'échantillon p_{O_2}= 50% (Figure 7-10). Cependant, pour une plus grande distance entre les pièges, la probabilité de l'effet tunnel assisté par pièges diminue rapidement, ce qui signifie que le courant total sera dominé par l'effet tunnel direct.

Ce résultat est corroboré expérimentalement dans l'échantillon p_{O_2}= 67% (Figure 7-9). Il en est de même lorsque nous fixons une distance moyenne constante entre les pièges et que nous analysons la dépendance de la densité de courant par rapport à l'épaisseur de la couche mince (Figure 7-11(b)). Pour les petites épaisseurs, la vitesse à laquelle les électrons traversent la barrière par effet tunnel est élevée, la contribution du courant d'effet tunnel direct est donc importante. Au fur et à mesure que l'épaisseur augmente, la contribution de l'effet tunnel direct diminue de manière exponentielle, pour atteindre une épaisseur critique à laquelle l'effet tunnel assisté par pièges devient dominant.

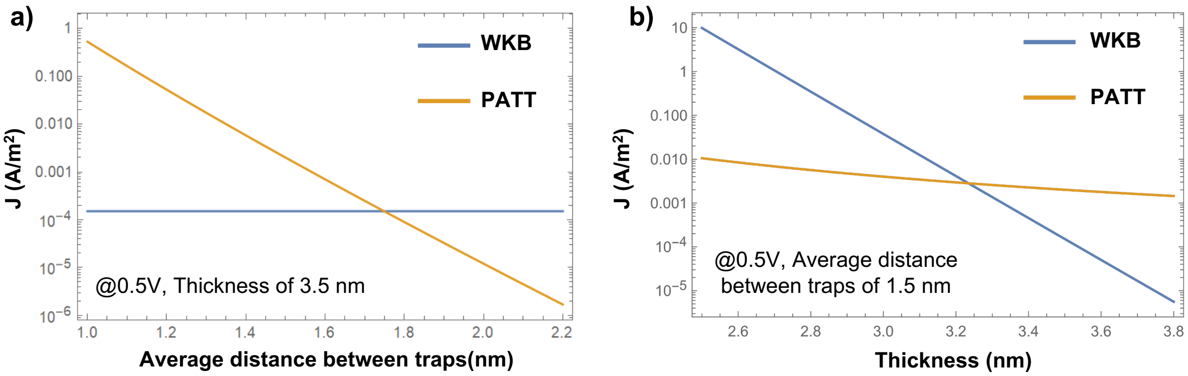

Figure 7-11: Tracé semi-logarithmique des contributions de la densité de courant de DT et PATT.

Tracé semi-logarithmique des contributions de la densité de courant de DT et PATT en fonction de a) la distance moyenne entre les pièges et b) l'épaisseur.

7.4.7 Endurance de l'effet tunnel direct et assisté par pièges

Comme nous l'avons démontré ci-dessus, l'effet tunnel direct et l'effet tunnel assisté par pièges ont la caractéristique de fournir deux états différents : HRS et LRS. Ces états seront modulés par l'inversion de polarisation dans le cas du FTJ (effet tunnel direct) et par la distance moyenne entre les pièges (lacunes d'oxygène) dans le cas de l'effet tunnel assisté par pièges. Par conséquent, la fiabilité de ces états dépendra des propriétés inhérentes de ces deux processus. Dans le cas d'une FTJ idéale, l'application récurrente d'un champ électrique alternatif (par exemple, un cycle d'impulsion de polarisation opposée) produira indéfiniment une inversion de polarisation. Cependant, divers facteurs tels que l'empreinte du champ électrique (*electric field* imprint), le *pinning* de la paroi du domaine (*domain wall pinning*), la dégradation de l'interface ferroélectrique-électrode ou les lacunes d'oxygène provoqueront une dégradation de la polarisation restante, conduisant à la fatigue du dispositif. Pour l'effet tunnel assisté par pièges, une performance quelque peu instable est attendue en raison de son lien direct avec la formation/annihilation de défauts dans le matériau.

Pour étudier ces scénarios, nous avons soumis les dispositifs obtenus sous p_{O_2}= 50% et p_{O_2}= 67% à 6×10^3 cycles d'écriture/effacement. La Figure 7-12 montre le HRS et le LRS pour les deux échantillons. Dans cette étude, nous avons utilisé une séquence d'impulsions, comme le montre la Figure 3-8, avec des tensions électriques d'écriture et d'effacement de -2 et 2 volts, respectivement, pour les échantillons avec p_{O_2}= 50% (3,5 nm) et p_{O_2}= 67% (3 nm). Dans les deux cas, une tension électrique de lecture de 0,6 V a été utilisée.

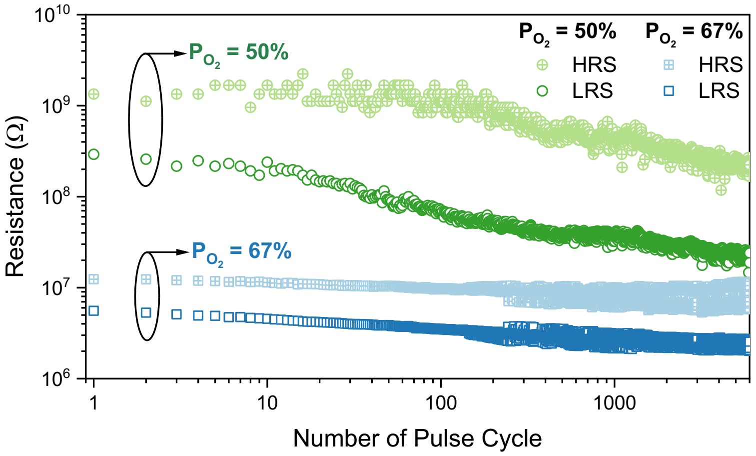

Figure 7-12: Mesure d'endurance sur deux dispositifs TiN/$Hf_{0,5}Zr_{0,5}O_2$/Au obtenus sous différentes pressions partielles d'oxygène.

Tracé log-log de la résistance en fonction du nombre de cycles. Les cercles correspondent à un dispositif obtenu avec p_{O_2}= 50% (3,5 nm) et les carrés correspondent à un dispositif obtenu avec p_{O_2}= 67% (3 nm).

Les états HRS et LRS de l'échantillon p_{O_2}= 67% montrent une tendance stable pendant le cyclage avec un rapport LRS/HRS approximativement constant mais légèrement réduit, probablement dû à la portion négligeable de la phase polaire dans le dispositif. Cette tendance stable remarquable du HRS et du LRS correspond à un taux de défaut relativement faible (lacunes d'oxygène) dans la couche mince de $Hf_{0,5}Zr_{0,5}O_2$.

En revanche, le dispositif basé sur des distances interpièges moyennes variables (p_{O_2}= 50%) présente un rapport LRS/HRS plus élevé. Cependant, le HRS et le LRS ont une dérive vers les résistances plus faibles, ce qui rend impossible la définition d'un seuil unique pour discriminer le HRS du LRS pendant tout le fonctionnement du dispositif. Cette dérive rend le système moins apte à être utilisé comme cellule de mémoire.

7.4.8 Commutation résistive basée sur les filaments de lacunes d'oxygène dans les couches minces non polaires de $Hf_{0,5}Zr_{0,5}O_{2-\delta}$

La caractéristique courant-tension (I-V) en courant continu de la cellule mémoire typique TiN/$Hf_{0.5}Zr_{0.5}O_{2-\delta}$/Au est représentée dans la Figure 7-13(a). Comme on peut le remarquer dans le premier cycle, surligné en rouge, l'état primitif est l'état résistif élevé (HRS). Lorsque la tension électrique passe de 0 V à -3,5 V, le dispositif passe à l'état de faible résistance (LRS) à la tension d'écriture (*Set Voltage* - V_{SET}) d'environ -2 V. Lors du balayage inverse, de 0 V à +3,9 V à la tension d'effacement (*Reset Voltage* - V_{RESET}) d'environ 2,5 V, le dispositif passe de l'état HRS à l'état LRS. Ceci confirme le comportement de commutation résistive bipolaire non volatile. La présence d'un processus d'électroformage n'a pas été observée, ce qui peut être dû à la concentration initiale élevée de défauts induite intentionnellement. Contrairement aux échantillons décrits dans la section 4.2, la couche de $Hf_{0,5}Zr_{0,5}O_{2-\delta}$ étudiée dans cette section a été déposée avec p_{O_2} = 0%. Cela favorise la formation de défauts (lacunes d'oxygène) dans la couche d'oxyde [34]. Pour étudier la stabilité et la reproductibilité de la mémoire, 100 cycles continus de courant continu ont été analysés. La distribution des tensions d'écriture et d'effacement est représentée dans un histogramme dans la Figure 7-13(b). Le V_{SET} montre une moyenne de -1,92 V avec un écart-type de 0,14 V, tandis que la moyenne pour le V_{RESET} était de 2,67 V avec un écart-type de 0,11 V. Une distribution étroite avec de faibles écarts-types est un indicateur fort de la stabilité de la mémoire. Le dispositif a montré un excellent rapport ΔR/R de 204 extrait à 0,1 V sur 100 cycles de balayage en courant continu (Figure 7-13(c)), R_{HRS} = 27,02 ± 9,25 KΩ (valeur moyenne : 27,02 KΩ ; écart-type : 9,25 KΩ) et R_{LRS} = 134,2 ± 17,8 Ω (valeur moyenne: 134,2 Ω ; écart-type : 17,8 Ω). La pente de la LRS était presque verticale, tandis que la HRS présentait une distribution étroite. La Figure 7-13(d) montre la distribution de la HRS et de la LRS dans huit cellules mémoires.

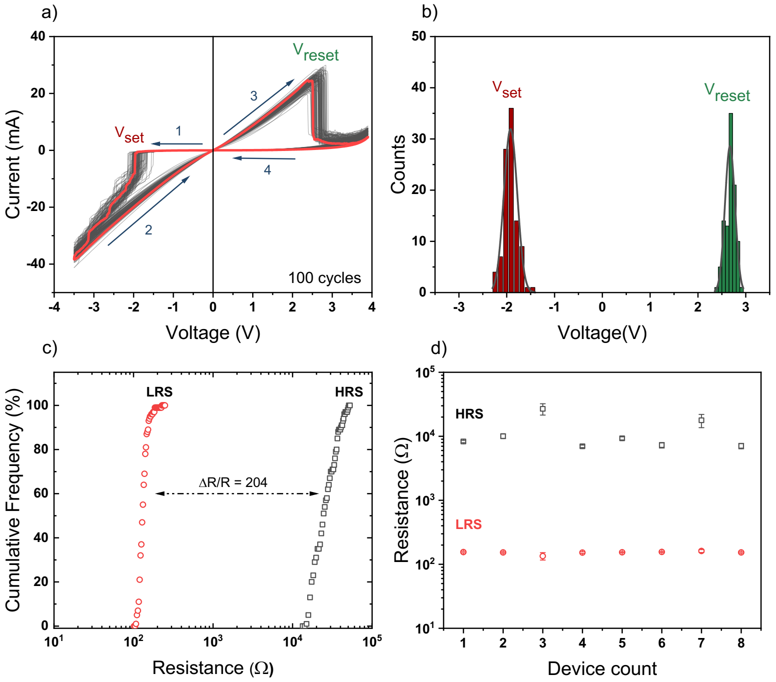

Figure 7-13: Caractéristiques courant-tension des dispositifs Au/$Hf_{0,5}Zr_{0,5}O_{2-\delta}$/TiN fabriqués.

a) 100 cycles de balayage en courant continu du dispositif Au/$Hf_{0,5}Zr_{0,5}O_{2-\delta}$/TiN. b) Distribution des tensions d'écriture et d'effacement. c) Fréquence cumulée pour LRS et HRS à 0,1V. d) Valeurs HRS et LRS testées sur huit cellules de mémoire différentes.

7.4.9 Mécanisme de conduction à travers les dispositifs TiN/$Hf_{0,5}Zr_{0,5}O_{2-\delta}$/Au

Pour étudier le mécanisme de conduction dominant des dispositifs TiN/$Hf_{0,5}Zr_{0,5}O_{2-\delta}$/Au et pour comprendre les implications des défauts dans l'évolution du processus de commutation résistive, les HRS et LRS ont été redessinés sur une échelle log-log, comme indiqué sur la Figure 7-14(a). Les données expérimentales pour les tensions électriques positives et négatives ont été reportées sur le même axe, en utilisant les valeurs absolues des courants et des tensions. En ce qui concerne le LRS pour les tensions électriques positive et négative, un ajustement linéaire avec une pente de 1,014 ± 0,001 dans la région de basse tension (< 0,5 V) a été déterminé à partir du tracé log(I) en fonction de log(V), comme indiqué sur la Figure 7-14(a). Une pente de ~ 1 indique que le LRS est dominé par un mécanisme de conduction linéaire. Cela indique que les pièges ont été occupés par les porteurs de charge injectés formant un filament conducteur [121]. À ce stade, nous aimerions souligner que la formation d'un filament d'or métallique ne peut être entièrement exclue, même si la faible porosité et l'épaisseur considérable de la couche mince rendent ce scénario relativement improbable. Dans le cas des courbes expérimentales négatives et positives I(V) pour le HRS, deux régions ont été identifiées ; pour les petites tensions (<0,15 V), la courbe présente un comportement linéaire tandis qu'une région non linéaire pour les tensions plus élevées (>0,15 V) est observée. La pente de ~1 observée pour les petites tensions <0,15 V, comme l'a souligné J.F. Scott [122], n'est pas suffisante pour établir une conduction ohmique. Cette relation linéaire I-V peut alternativement être expliquée par les mécanismes d'émission Schottky et/ou Schottky modifié de Simmons [122]. Comme le souligne J.F. Scott dans son article, des mesures de courant en fonction de l'épaisseur sont nécessaires pour distinguer les mécanismes de conduction ohmique des mécanismes de Simmons/Schottky, car seul le modèle ohmique, donné par l'équation empirique de Kirchhoff, dépend de l'épaisseur.

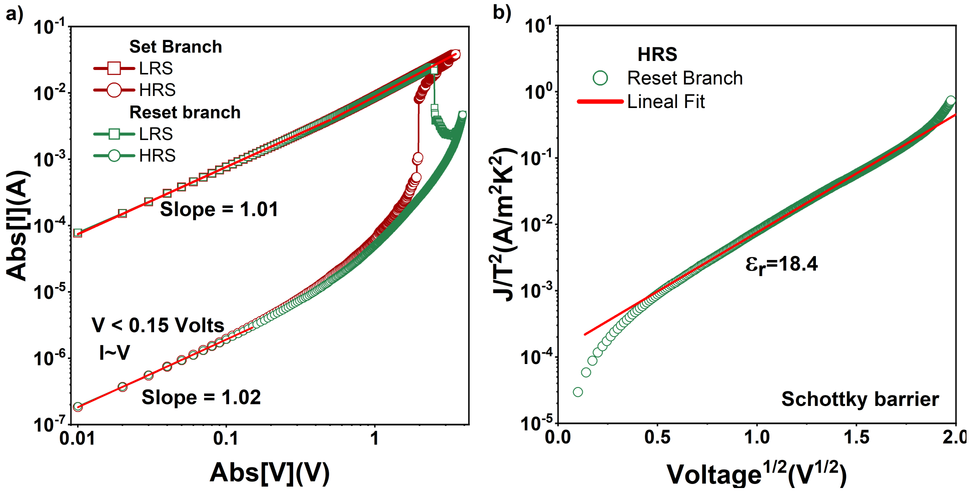

Figure 7-14: Tracé de l'I-V typique du dispositif TiN/$Hf_{0,5}Zr_{0,5}O_{2-\delta}$/Au.

a) Tracé log-log de l'I-V typique Les données expérimentales pour les tensions électriques positives et négatives ont été reportées sur le même axe, mesurées à 295 K. Les valeurs absolues ont été appliquées à la tension et au courant. b) Tracé semi-logarithmique de (J/T^2) en fonction de $V^{1/2}$ pour la portion positive du cycle positive avec un ajustement linéaire.

Pour une gamme de tension électrique plus élevée (pente ≠1), afin de déterminer le mécanisme de transport dominant dans le dispositif, le tracé I-V a également été ajusté en utilisant le mécanisme d'émission Schottky. Dans l'émission Schottky ou thermionique, les électrons sous une énergie thermique suffisante surmontent la barrière de potentiel à l'interface électrode-oxyde. Le résultat de l'ajustement de la courbe I-V dans l'état HRS en utilisant l'émission Schottky est représenté sur la Figure 7-14(b). Un ajustement linéaire de $\ln(J/T^2)$ en fonction de $V^{1/2}$ pour HRS indique que l'émission Schottky est le mécanisme de conduction dominant. À partir de la pente d'ajustement Schottky (Figure 7-14 (b)), la constante diélectrique calculée (ε_r) était d'environ 18,4, ce qui est en accord avec la valeur ε_r rapportée dans la littérature [128]. Puisque c'est la valeur attendue pour la constante diélectrique, cela suggère que le mécanisme de conduction dans le dispositif est dominé par l'émission Schottky [129].

7.4.10 Test d'endurance et de rétention

Les caractéristiques d'endurance et de rétention du dispositif ont été déterminées afin d'évaluer plus précisément la fiabilité du dispositif TiN/$Hf_{0,5}Zr_{0,5}O_{2-\delta}$/Au. Pour l'endurance, une séquence d'impulsions d'écriture/effacement d'une amplitude de -3,5 V/+3,9 V et d'une largeur de 5 ms a été appliquée. Le HRS et le LRS ont été lus à 0,1 V, fixé comme les impulsions d'écriture/effacement de base, pendant 5 ms (illustration dans la Figure 7-15(a)). L'endurance du dispositif TiN/$Hf_{0,5}Zr_{0,5}O_{2-\delta}$/Au représenté dans la figure 4-20(a) démontre la capacité du dispositif TiN/$Hf_{0,5}Zr_{0,5}O_{2-\delta}$/Au à modifier les impulsions de courant pendant 10^4 cycles dans des conditions ambiantes à température ambiante. Les histogrammes pour le HRS et le LRS sont présentés dans la Figure 7-15(b). Le LRS présente une valeur moyenne de 162,19 Ω avec un écart-type de 8,20 Ω, tandis que le HRS présente un écart-type de 0,560 KΩ et une valeur moyenne de 7,20 KΩ. Aucune fluctuation ou dégradation de l'endurance n'a été observée même jusqu'à 10^4 nombres d'impulsions, ce qui confirme la stabilité du rapport R_{ON}/R_{OFF}. Au cours des 10^4 cycles d'impulsions successifs, l'échantillon testé a présenté un rapport $\Delta R/R > 4000\%$, sans dégradation observée, ce qui signifie que le dispositif dépasse l'exigence de base pour les applications ReRAM. Le fonctionnement dans des conditions ambiantes sans atmosphère protectrice ni barrière de diffusion de l'oxygène favorise généralement l'échange d'oxygène avec l'atmosphère et accélère la dégradation du dispositif. Avec ces précautions supplémentaires, les expériences futures fourniront des valeurs plus proches du fonctionnement du dispositif intégré.

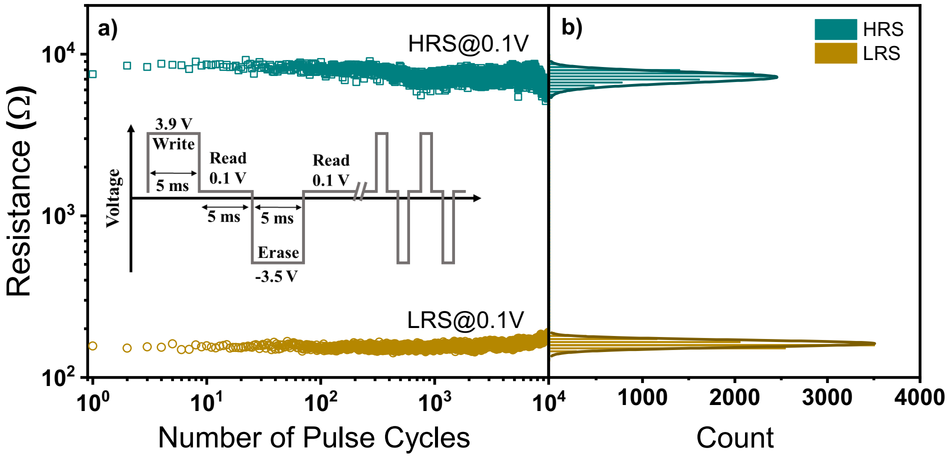

Figure 7-15: Mesure d'endurance sur le dispositif TiN/$Hf_{0,5}Zr_{0,5}O_{2-\delta}$/Au.

a) Résistance en fonction du nombre de cycles. b) Distribution des résistances des états ON et OFF. La résistance a été mesurée en régime d'impulsions à une tension de lecture de 0,1 V. L'illustration montre les séquences de mesure des impulsions.

L'évolution temporelle du HRS et du LRS et les caractéristiques de rétention du dispositif ont été déterminées, comme le montre la Figure 7-16. Le HRS et le LRS ont été mesurées avec une tension de lecture de 0,1 V appliquée pendant 5 ms pendant des intervalles logarithmiques, après avoir appliqué une seule impulsion d'écriture/effacement de -3,5 V/+3,9 V.

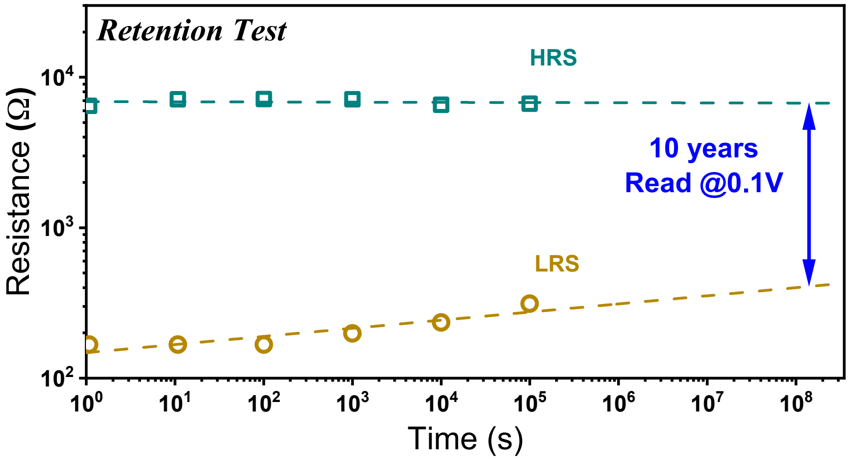

Figure 7-16: Mesure de rétention sur le dispositif TiN/$Hf_{0,5}Zr_{0,5}O_{2-\delta}$/Au.

Les lignes pointillées montrent une extrapolation à dix ans sous l'hypothèse d'une dépendance de type loi de puissance. La résistance a été mesurée en régime impulsionnel à une tension de lecture de 0,1 V.

Les valeurs de résistance dans le LRS et le HRS sont restées constantes sur une longue période (10^5 s), confirmant la stabilité et la nature non volatile du dispositif. La mesure de rétention indique une tendance à la dégradation qui préserverait encore un ordre de grandeur du rapport ON/OFF après 10 ans, comme l'illustre la Figure 7-16, des caractéristiques d'endurance et des données expérimentales des dispositifs TiN/$Hf_{0,5}Zr_{0,5}O_{2-\delta}$/Au. Ces caractéristiques suggèrent une performance d’entreposage supérieure pour la mémoire résistive.

7.5 CONCLUSION

Les FTJ à base de HfO_2 ont suscité un énorme intérêt dans le domaine de l'entreposage d'informations, principalement en raison de leurs performances (résistance élevée à la fatigue, vitesse élevée et grande extensibilité) et de la compatibilité du $Hf_{0,5}Zr_{0,5}O_2$ avec les procédés technologiques CMOS. En outre, il est possible d'obtenir une plasticité fonction du temps d'occurrence des impulsions (STDP) dans la mémoire FTJ, ce qui souligne son potentiel pour l'informatique neuromorphique. La phase orthorhombique métastable ($Pca2_1$) est responsable de la ferroélectricité dans le HfO_2 dopé. Les différentes voies pour stabiliser cette phase non centrosymétrique incluent le dopage, la déformation, l'énergie de la surface/interface/joint de grain, la température de recuit et les lacunes d'oxygène introduites intentionnellement. Dans cette étude, nous fabriquons des structures $TiN/Hf_{0,5}Zr_{0,5}O_2/Au$ en utilisant la pulvérisation cathodique magnétron à radiofréquence (RF) avec une pression partielle d'oxygène variable pendant le dépôt de la couche mince de $Hf_{0,5}Zr_{0,5}O_2$. La formation de la phase ferroélectrique orthorhombique dans $Hf_{0,5}Zr_{0,5}O_2$ a été étudiée par deux méthodes de recuit, le recuit in situ et le recuit thermique rapide (RTA). Les diffractogrammes des échantillons soumis au RTA ont montré une augmentation de l'intensité à $2\theta = 30.8°$, correspondant aux positions de chevauchement des pics orthorhombique (111) et tétragonal (101). La microscopie à force piézoélectrique (PFM) a été utilisée pour élucider ces deux phases puisque la phase orthorhombique est la seule favorable à la ferroélectricité et, par conséquent, la seule qui présentera une polarisation spontanée réversible. Elle corrobore le processus de RTA comme une voie directe pour former la phase orthorhombique ferroélectrique ($Pca2_1$) dans $Hf_{0,5}Zr_{0,5}O_2$. De plus, nos résultats sont en accord avec la littérature sur l'amélioration de la phase ferroélectrique dans les couches minces de $Hf_{0,5}Zr_{0,5}O_2$ déposées sous une atmosphère appauvrie en oxygène.

L'étude de l'effet tunnel à travers des structures $TiN/Hf_{0,5}Zr_{0,5}O_2/Au$ nous a permis d'analyser l'influence de la pression partielle d'oxygène sur le mécanisme d'effet tunnel. Nous avons démontré que les structures $Hf_{0,5}Zr_{0,5}O_2$ déposées dans une atmosphère riche en oxygène (p_{O_2}= 67%) sont adaptées à l'effet tunnel direct. En comparaison, ceux obtenus dans une atmosphère semi-déficiente en oxygène (p_{O_2}= 50%) sont favorables à l'effet tunnel assisté par pièges. En utilisant le modèle PATT, il a été possible d'obtenir la distance moyenne entre les pièges. L'analyse comparative des modèles PATT et WKB pour différentes épaisseurs de couches nous a permis de déterminer les épaisseurs critiques pour lesquelles l'un des mécanismes d'effet tunnel sera dominant. De même, la comparaison de différentes densités de pièges (distance moyenne entre les pièges) nous permet de déterminer le seuil de distance moyenne entre les pièges pour la prédominance des mécanismes d'effet tunnel. Ce travail fournit donc un intervalle d'épaisseurs de couches minces et de densités de pièges pour une performance optimale de l’effet tunnel des FJTs. Le test d'endurance démontre la stabilité des dispositifs à effet tunnel direct par rapport à ceux basés sur l'effet tunnel assisté par pièges.

Dans le cas de $Hf_{0,5}Zr_{0,5}O_2$ déposé dans une atmosphère totalement appauvrie en oxygène (p_{O_2}= 0%), il a été démontré que la formation d'un filament de lacunes d'oxygène est possible. Nous concluons qu'en plus de son excellence dans les FTJs, le $Hf_{0,5}Zr_{0,5}O_2$ peut être utilisé comme une mémoire résistive à lacunes d'oxygène. Nous démontrons la formation d'une commutation résistive stable et reproductible avec un rapport ON/OFF élevé de 10^2 jusqu'à 10^4 cycles d'impulsions et une rétention d'au moins 10^5 s

8 BIBLIOGRAPHY

1. CRTC, *Communications Monitoring Report*. 2020, Government of Canada.
2. Moore, G.E., *Cramming more components onto integrated circuits.* Electronics, 1965. **38**(8): p. 114-114.
3. Lai, S.K., *Flash memories: Successes and challenges.* IBM Journal of Research and Development, 2008. **52**(4.5): p. 529-535.
4. Kingon, A.I., J.P. Maria, and S.K. Streiffer, *Alternative dielectrics to silicon dioxide for memory and logic devices.* Nature, 2000. **406**(6799): p. 1032-1038.
5. Garcia, V. and M. Bibes, *Ferroelectric tunnel junctions for information storage and processing.* Nature Communications, 2014. **5**: p. 1-12.
6. Garcia, V., et al., *Giant tunnel electroresistance for non-destructive readout of ferroelectric states.* Nature, 2009. **460**(7251): p. 81-84.
7. Gruverman, A., et al., *Tunneling electroresistance effect in ferroelectric tunnel junctions at the nanoscale.* Nano Letters, 2009. **9**(10): p. 3539-3543.
8. Fina, I. and F. Sánchez, *Epitaxial Ferroelectric HfO2 Films: Growth, Properties, and Devices.* ACS Applied Electronic Materials, 2021. **3**(4): p. 1530-1549.
9. Yamada, H., et al., *Giant electroresistance of super-tetragonal* $BiFeO_3$*-based ferroelectric tunnel junctions.* ACS Nano, 2013. **7**(6): p. 5385-90.
10. Chanthbouala, A., et al., *A ferroelectric memristor.* Nature Materials, 2012. **11**(10): p. 860-864.
11. Tsymbal, E.Y. and A. Gruverman, *Ferroelectric tunnel junctions: Beyond the barrier.* Nature Materials, 2013. **12**(7): p. 602-604.
12. Hubbard, K.J. and D.G. Schlom, *Thermodynamic stability of binary oxides in contact with silicon.* Journal of Materials Research, 1996. **11**(11): p. 2757-2776.
13. Schlom, D.G. and J.H. Haeni, *A Thermodynamic Approach to Selecting Alternative Gate Dielectrics.* MRS Bulletin, 2002. **27**(3): p. 198-204.
14. Böscke, T.S., et al., *Ferroelectricity in hafnium oxide thin films.* Applied Physics Letters, 2011. **99**(10): p. 102903-102903.
15. Gilmer, D.C., et al., *Compatibility of polycrystalline silicon gate deposition with* HfO_2 *and* Al_2O_3/HfO_2 *gate dielectrics.* Applied Physics Letters, 2002. **81**(7): p. 1288-1290.
16. Mistry, K., et al. *A 45nm logic technology with high-k+ metal gate transistors, strained silicon, 9 Cu interconnect layers, 193nm dry patterning, and 100% Pb-free packaging*. in *Technical Digest - International Electron Devices Meeting, IEDM*. 2007.
17. Müller, J., et al. *Ferroelectric hafnium oxide: A CMOS-compatible and highly scalable approach to future ferroelectric memories*. in *Technical Digest - International Electron Devices Meeting, IEDM*. 2013.
18. Gruverman, A., et al., *Direct studies of domain switching dynamics in thin film ferroelectric capacitors.* Applied Physics Letters, 2005. **87**(8): p. 14-16.

19. Mulaosmanovic, H., T. Mikolajick, and S. Slesazeck, *Accumulative Polarization Reversal in Nanoscale Ferroelectric Transistors.* ACS Appl Mater Interfaces, 2018. **10**(28): p. 23997-24002.

20. Kolhatkar, G., et al., *$BiFe_{1-x}Cr_xO_3$ Ferroelectric Tunnel Junctions for Neuromorphic Systems.* ACS Applied Electronic Materials, 2019. **1**(6): p. 828-835.

21. Mittermeier, B., et al., *CMOS Compatible $Hf_{0.5}Zr_{0.5}O_2$ Ferroelectric Tunnel Junctions for Neuromorphic Devices.* Advanced Intelligent Systems, 2019. **1**(5): p. 1900034-1900034.

22. Chen, H., et al., *HfO_2-based ferroelectrics: From enhancing performance, material design, to applications.* Applied Physics Reviews, 2022. **9**(1): p. 011307-011307.

23. Mueller, S., et al., *Incipient ferroelectricity in Al-doped HfO_2 thin films.* Advanced Functional Materials, 2012. **22**(11): p. 2412-2417.

24. Sang, X., et al., *On the structural origins of ferroelectricity in HfO_2 thin films.* Applied Physics Letters, 2015. **106**(16): p. 162905-162905.

25. Starschich, S. and U. Boettger, *An extensive study of the influence of dopants on the ferroelectric properties of HfO_2.* Journal of Materials Chemistry C, 2017. **5**(2): p. 333-338.

26. Shiraishi, T., et al., *Impact of mechanical stress on ferroelectricity in $(Hf_{0.5}Zr_{0.5})O_2$ thin films.* Applied Physics Letters, 2016. **108**(26): p. 262904-262904.

27. Park, M.H., et al., *A comprehensive study on the mechanism of ferroelectric phase formation in hafnia-zirconia nanolaminates and superlattices.* Applied Physics Reviews, 2019. **6**(4).

28. Materlik, R., C. Kunneth, and A. Kersch, *The origin of ferroelectricity in $Hf_{1-x}Zr_xO_2$: A computational investigation and a surface energy model.* Journal of Applied Physics, 2015. **117**(13): p. 134109-134109.

29. Hyuk Park, M., et al., *Evolution of phases and ferroelectric properties of thin $Hf_{0.5}Zr_{0.5}O_2$ films according to the thickness and annealing temperature.* Applied Physics Letters, 2013. **102**(24): p. 242905-242905.

30. Materano, M., et al., *Influence of oxygen content on the structure and reliability of ferroelectric $Hf_xZr_{1-x}O_2$ layers.* ACS Applied Electronic Materials, 2020. **2**(11): p. 3618-3626.

31. Zhou, Y., et al., *The effects of oxygen vacancies on ferroelectric phase transition of HfO2-based thin film from first-principle.* Computational Materials Science, 2019. **167**: p. 143-150.

32. Mimura, T., et al., *Room-temperature deposition of ferroelectric HfO_2-based films by the sputtering method.* Applied Physics Letters, 2020. **116**(6).

33. Starschich, S., S. Menzel, and U. Böttger, *Evidence for oxygen vacancies movement during wake-up in ferroelectric hafnium oxide.* Applied Physics Letters, 2016. **108**(3).

34. González, Y., et al., *Competing tunneling conduction mechanisms in oxygen deficient $Hf_{0.5}Zr_{0.5}O_2$.* Applied Physics Letters, 2021. **119**(13): p. 132906-132906.

35. González, Y., et al., *Mechanism of Oxygen Vacancy Filament-Based Resistive Switching in Non-polar $Hf_{0.5}Zr_{0.5}O_{2-\delta}$ Thin Films.* ACS Applied Electronic Materials, 2022. **4**(3): p. 1311-1317.

36. Matthias, B.T., *Ferroelectricity.* Journal of Applied Physics, 1967. **38**(3): p. 928-930.

37. Valasek, J., *Piezo-Electric and Allied Phenomena in Rochelle Salt.* Physical Review, 1921. **17**(4): p. 475-481.

38. Fousek, J. and V. Janovec, *The orientation of domain walls in twinned ferroelectric crystals.* Journal of Applied Physics, 1969. **40**(1): p. 135-142.

39. Dawber, M., K.M. Rabe, and J.F. Scott, *Physics of thin-film ferroelectric oxides.* Reviews of Modern Physics, 2005. **77**(4): p. 1083-1130.

40. Soergel, E., *Visualization of ferroelectric domains in bulk single crystals.* Applied Physics B: Lasers and Optics, 2005. **81**(6): p. 729-752.

41. Müller, J., et al., *Ferroelectricity in Simple Binary* ZrO_2 *and* HfO_2*.* Nano Lett, 2012. **12**(8): p. 4318-23.

42. Lee, S.K. and C.W. Bark, *Crystallographic structure and ferroelectricity of epitaxial hafnium oxide thin films.* J. Korean Ceram. Soc., 2022. **59**(1): p. 25-43.

43. He, G. and Z. Sun, *High-k Gate Dielectrics for CMOS Technology*. High-k Gate Dielectrics for CMOS Technology. 2012: Wiley-VCH.

44. Dörfler, A., *Ferroelectric Tunnel Junctions: Models for Memory and Neuromorphic Applications*, in *Institut national de la recherche scientifique*. 2021, Université du Québec: Québec. p. 169.

45. Müller, J., et al., *Ferroelectricity in yttrium-doped hafnium oxide.* Journal of Applied Physics, 2011. **110**(11): p. 114113-114113.

46. Mueller, S., et al., *Ferroelectricity in Gd-Doped* HfO_2 *Thin Films.* ECS Journal of Solid State Science and Technology, 2012. **1**(6): p. N123-N126.

47. Schroeder, U., et al., *Impact of different dopants on the switching properties of ferroelectric hafniumoxide.* Japanese Journal of Applied Physics, 2014. **53**(8S1): p. 08LE02-08LE02.

48. Tsai, S.-H., et al., *Stress-Memorized HZO for High-Performance Ferroelectric Field-Effect Memtransistor.* ACS Applied Electronic Materials, 2022. **4**(4): p. 1642-1650.

49. Pertsev, N.A., A.G. Zembilgotov, and A.K. Tagantsev, *Effect of Mechanical Boundary Conditions on Phase Diagrams of Epitaxial Ferroelectric Thin Films.* Physical Review Letters, 1998. **80**(9): p. 1988-1991.

50. Hoffmann, M., et al., *Stabilizing the ferroelectric phase in doped hafnium oxide.* Journal of Applied Physics, 2015. **118**(7).

51. Fan, Z., et al., *Ferroelectricity emerging in strained (111)-textured* ZrO_2 *thin films.* Applied Physics Letters, 2016. **108**(1): p. 012906-012906.

52. Cao, J., et al., *An Overview of Ferroelectric Hafnia and Epitaxial Growth*, in *Physica Status Solidi - Rapid Research Letters*. 2021, John Wiley and Sons Inc.

53. Migita, S., et al., *Polarization switching behavior of Hf–Zr–O ferroelectric ultrathin films studied through coercive field characteristics.* Japanese Journal of Applied Physics, 2018. **57**(4S).

54. Yurchuk, E., et al., *Impact of layer thickness on the ferroelectric behaviour of silicon doped hafnium oxide thin films.* Thin Solid Films, 2013. **533**: p. 88-92.

55. Shimizu, T., et al., *Growth of epitaxial orthorhombic* $YO_{1.5}$*-substituted* HfO_2 *thin film.* Applied Physics Letters, 2015. **107**(3): p. 032910-032910.

56. Katayama, K., et al., *Orientation control and domain structure analysis of {100}-oriented epitaxial ferroelectric orthorhombic HfO_2-based thin films.* Journal of Applied Physics, 2016. **119**(13): p. 134101-134101.

57. Katayama, K., et al., *Growth of (111)-oriented epitaxial and textured ferroelectric Y-doped HfO_2 films for downscaled devices.* Applied Physics Letters, 2016. **109**(11): p. 112901-112901.

58. Shimizu, T., et al., *The demonstration of significant ferroelectricity in epitaxial Y-doped HfO_2 film.* Scientific Reports, 2016. **6**: p. 32931.

59. Nukala, P., et al., *Direct epitaxial growth of polar $(1-x)HfO_2(x)ZrO_2$ ultra-thin films on Silicon.* ACS Applied Electronic Materials, 2019. **1**(12): p. 2585-2593.

60. Lyu, J., et al., *Growth Window of Ferroelectric Epitaxial $Hf_{0.5}Zr_{0.5}O_2$ Thin Films.* ACS Applied Electronic Materials, 2019. **1**(2): p. 220-228.

61. Xu, X., et al., *Kinetically stabilized ferroelectricity in bulk single-crystalline HfO_2:Y.* Nature Materials, 2021. **20**(6): p. 826-832.

62. Song, T., et al., *Improved polarization and endurance in ferroelectric $Hf_{0.5}Zr_{0.5}O_2$ films on $SrTiO_3$(110).* Nanoscale, 2022. **14**(6): p. 2337-2343.

63. Barriuso, E., et al., *Direct Epitaxial Growth of Polar $Hf_{0.5}$ $Zr_{0.5}$ O_2 Films on Corundum.* Nanomaterials, 2022. **12**(7): p. 1232-1232.

64. Sharath, S.U., et al., *Thickness independent reduced forming voltage in oxygen engineered HfO_2 based resistive switching memories.* Applied Physics Letters, 2014. **105**(7): p. 73505-73505.

65. Lee, Y.H., et al., *Preparation and characterization of ferroelectric $Hf_{0.5}Zr_{0.5}O_2$ thin films grown by reactive sputtering.* Nanotechnology, 2017. **28**(30).

66. Mittmann, T., et al., *Origin of Ferroelectric Phase in Undoped HfO_2 Films Deposited by Sputtering.* Advanced Materials Interfaces, 2019. **6**(11): p. 1900042-1900042.

67. Pal, A., et al., *Enhancing ferroelectricity in dopant-free hafnium oxide.* Applied Physics Letters, 2017. **110**(2): p. 022903-022903.

68. Waser, R. and M. Aono, *Nanoionics-based resistive switching memories*, in *Nanoscience and Technology: A Collection of Reviews from Nature Journals*. 2009. p. 158-165.

69. Slesazeck, S. and T. Mikolajick, *Nanoscale resistive switching memory devices: a review.* Nanotechnology, 2019. **30**(35): p. 352003-352003.

70. De Stefano, F., et al. *Nature of the filament formed in HfO_2-based resistive random access memory*. in *Thin Solid Films*. 2013. Elsevier.

71. Waser, R., et al. *Function by defects at the atomic scale - New concepts for non-volatile memories*. in *Solid-State Electronics*. 2010. Pergamon.

72. Li, X.Y., et al., *Thin TiO_x layer as a voltage divider layer located at the quasi-Ohmic junction in the $Pt/Ta_2O_5/Ta$ resistance switching memory.* Nanoscale, 2017. **9**(6): p. 2358-2368.

73. Cagli, C., et al. *Experimental and theoretical study of electrode effects in HfO_2 based RRAM*. in *Technical Digest - International Electron Devices Meeting, IEDM*. 2011.

74. Buck, D.A., *Ferroelectrics for Digital Information Storage and Switching. Report R-212*. 1952.

75. Scott, J.F., *Applications of modern ferroelectrics.* Science, 2007. **315**(5814): p. 954-959.

76. Schenk, T., et al. *10 Years Fluorite-type Ferroelectrics – A Survey*. in *Toward Oxide-based Electronics, Spring Meeting*. 2017.

77. Esaki, L., R.B.B. Laibowitz, and P.J.J. Stiles, *Polar switch.* IBM Techn. Disclo. Bull., 1971. **13**(2161): p. 2161-2162.

78. Rodriguez Contreras, J., et al., *Resistive switching in metal-ferroelectric-metal junctions.* Applied Physics Letters, 2003. **83**(22): p. 4595-4597.

79. Maksymovych, P., et al., *Polarization control of electron tunneling into ferroelectric surfaces.* Science, 2009. **324**(5933): p. 1421-1425.

80. McKee, R.A., F.J. Walker, and M.F. Chisholm, *Crystalline oxides on silicon: The first five monolayers.* Physical Review Letters, 1998. **81**(14): p. 3014-3017.

81. Wouters, D.J., et al., *Integration of* $SrBi_2Ta_2O_9$ *thin films for high density ferroelectric random access memory.* Journal of Applied Physics, 2006. **100**(5): p. 051603-051603.

82. Pantel, D. and M. Alexe, *Electroresistance effects in ferroelectric tunnel barriers.* Physical Review B - Condensed Matter and Materials Physics, 2010. **82**(13): p. 134105-134105.

83. Sze, S.M. and K.K. Ng, *Physics of Semiconductor Devices*. Physics of Semiconductor Devices. 2006: John Wiley & Sons, Inc.

84. Brinkman, W.F., R.C. Dynes, and J.M. Rowell, *Tunneling conductance of asymmetrical barriers.* Journal of Applied Physics, 1970. **41**(5): p. 1915-1921.

85. Fowler, R.H. and L. Nordheim, *Electron Emission in Intense Electric Fields.* Proceedings of the Royal Society A: Mathematical, Physical and Engineering Sciences, 1928. **119**(781): p. 173-181.

86. Frenkel, J., *On Pre-Breakdown Phenomena in Insulators and Electronic Semi-Conductors.* Physical Review, 1938. **54**(8): p. 647-648.

87. Lampert, M.A. and R.B. Schilling, *Chapter 1 Current Injection in Solids: The Regional Approximation Method*, in *Semiconductors and Semimetals*. 1970, Elsevier. p. 1-96.

88. Nasyrov, K.A. and V.A. Gritsenko, *Charge transport in dielectrics by tunneling between traps.* Journal of Experimental and Theoretical Physics, 2011. **112**(6): p. 1026-1034.

89. Islamov, D.R., et al., *Identification of the nature of traps involved in the field cycling of* $Hf_{0.5}Zr_{0.5}O_2$*-based ferroelectric thin films.* Acta Materialia, 2019. **166**(September 2019): p. 47-55.

90. Islamov, D.R., et al., *Charge transport mechanism in thin films of amorphous and ferroelectric* $Hf_{0.5}Zr_{0.5}O_2$*.* JETP Letters, 2016. **102**(8): p. 544-547.

91. Swann, S., *Magnetron sputtering.* Physics in Technology, 1988. **19**(2): p. 67-75.

92. Chapman, B.N., *RF Discharges*, in *Glow discharge processes: sputtering and plasma etching*. 1980, Wiley. p. 406-406.

93. Gibaud, A., M.S. Chebil, and T. Beuvier, *X-Ray Reflectivity*, in *Surface Science Techniques*, G. Bracco and B. Holst, Editors. 2013, Springer Berlin Heidelberg: Berlin, Heidelberg. p. 191-216.

94. Binnig, G., C.F. Quate, and C. Gerber, *Atomic Force Microscope.* Physical Review Letters, 1986. **56**(9): p. 930-933.

95. Voigtländer, B., *Scanning Probe Microscopy*. NanoScience and Technology. 2015.

96. Martin, Y., C.C. Williams, and H.K. Wickramasinghe, *Atomic force microscope-force mapping and profiling on a sub 100-Å scale.* Journal of Applied Physics, 1987. **61**(10): p. 4723-4729.

97. Albrecht, T.R., et al., *Frequency modulation detection using high-Q cantilevers for enhanced force microscope sensitivity.* Journal of Applied Physics, 1991. **69**(2): p. 668-673.

98. van der Pauw, L.J., *Method of measuring resistivity and Hall coefficient on lamellae of arbitrary shape.* Philips Technical Review, 1959. **20**(8): p. 220-224.

99. Dörfler, A., et al., *The effects of thin film homogeneity on the performance of ferroelectric tunnel junctions.* Journal of Physics: Condensed Matter, 2020. **32**(18): p. 185302-185302.

100. Van Bui, H., A.Y. Kovalgin, and R.A.M. Wolters, *On the difference between optically and electrically determined resistivity of ultra-thin titanium nitride films.* Applied Surface Science, 2013. **269**: p. 45-49.

101. Zenkevich, A., et al., *Electronic band alignment and electron transport in Cr/$BaTiO_3$/Pt ferroelectric tunnel junctions.* Applied Physics Letters, 2013. **102**(6).

102. Chernikova, A., et al., *Ultrathin $Hf_{0.5}Zr_{0.5}O_2$ Ferroelectric Films on Si.* ACS Appl Mater Interfaces, 2016. **8**(11): p. 7232-7.

103. Gunkel, F., et al., *Oxygen vacancies: The (in)visible friend of oxide electronics.* Applied Physics Letters, 2020. **116**(12): p. 120505-120505.

104. Yoon, J., et al., *Understanding tunneling electroresistance effect through potential profile in Pt/$Hf_{0.5}Zr_{0.5}O_2$/TiN ferroelectric tunnel junction memory.* Applied Physics Letters, 2019. **115**(15): p. 153502-153502.

105. Makram-Ebeid, S. and M. Lannoo, *Electric-Field-Induced Phonon-Assisted Tunnel Ionization from Deep Levels in Semiconductors.* Physical Review Letters, 1982. **48**(18): p. 1281-1281.

106. Islamov, D.R., et al., *Origin of traps and charge transport mechanism in hafnia.* Applied Physics Letters, 2014. **105**(22).

107. Islamov, D.R., V.A. Gritsenko, and M.S. Lebedev, *Determination of Trap Density in Hafnium Oxide Films Produced by Different Atomic Layer Deposition Techniques.* ECS Transactions, 2017. **80**(1): p. 265-270.

108. Strand, J.W., et al., *Effect of electric field on defect generation and migration in HfO_2.* Physical Review B, 2020. **102**(1).

109. Bradley, S.R., A.L. Shluger, and G. Bersuker, *Electron-Injection-Assisted Generation of Oxygen Vacancies in Monoclinic HfO_2.* Physical Review Applied, 2015. **4**(6).

110. Max, B., et al., *Hafnia-based double-layer ferroelectric tunnel junctions as artificial synapses for neuromorphic computing.* ACS Applied Electronic Materials, 2020. **2**(12): p. 4023-4033.

111. Kim, S.J., et al., *Ferroelectric $Hf_{0.5}Zr_{0.5}O_2$ Thin Films: A Review of Recent Advances.* JOM, 2019. **71**(1): p. 246-255.

112. Ryu, H., et al., *Ferroelectric Tunneling Junctions Based on Aluminum Oxide/ Zirconium-Doped Hafnium Oxide for Neuromorphic Computing.* Scientific Reports, 2019. **9**(1): p. 1-8.

113. Wang, T.Y., et al., *Atomic Layer Deposited $Hf_{0.5}Zr_{0.5}O_2$-based Flexible Memristor with Short/Long-Term Synaptic Plasticity.* Nanoscale Research Letters, 2019. **14**(1): p. 1-6.

114. Xiao, W., et al., *Memory Window and Endurance Improvement of $Hf_{0.5}Zr_{0.5}O_2$-Based FeFETs with ZrO_2 Seed Layers Characterized by Fast Voltage Pulse Measurements.* Nanoscale Research Letters, 2019. **14**(1): p. 1-7.

115. Kim, J., et al., *Thermal conductivity of plasma-enhanced atomic layer deposited hafnium zirconium oxide dielectric thin films.* Journal of the European Ceramic Society, 2021. **41**(6): p. 3397-3403.

116. Wang, S.Y., et al., *Controllable oxygen vacancies to enhance resistive switching performance in a ZrO_2-based RRAM with embedded Mo layer.* Nanotechnology, 2010. **21**(49): p. 495201-495201.

117. Yong, Z., et al., *Tuning oxygen vacancies and resistive switching properties in ultra-thin HfO_2 RRAM via TiN bottom electrode and interface engineering.* Applied Surface Science, 2021. **551**: p. 149386-149386.

118. Shen, Z., et al., *Advances of RRAM Devices: Resistive Switching Mechanisms, Materials and Bionic Synaptic Application.* Nanomaterials 2020, Vol. 10, Page 1437, 2020. **10**(8): p. 1437-1437.

119. Wei, W., et al., *Spontaneous polarization enhancement in ferroelectric $Hf_{0.5}Zr_{0.5}O_2$ using atomic oxygen defects engineering: An ab initio study.* Applied Physics Letters, 2019. **115**(9): p. 092905-092905.

120. Hamouda, W., et al., *Physical chemistry of the TiN/$Hf_{0.5}Zr_{0.5}O_2$ interface.* Journal of Applied Physics, 2020. **127**(6): p. 064105-064105.

121. Sultana, R., et al., *Effect of Zr doping and lattice oxygen release on the resistive switching properties of $Zr_xHf_{1-x}O_2$-based metal-oxide-semiconductor devices.* Microelectronic Engineering, 2019. **216**: p. 111099-111099.

122. Scott, J.F., *There's no place like Ohm: Conduction in oxide thin films.* Journal of Physics Condensed Matter, 2014. **26**(14): p. 142202-142202.

123. Liu, Q., et al., *Resistive switching memory effect of ZrO_2 films with Zr^+ implanted.* Applied Physics Letters, 2008. **92**(1): p. 012117-012117.

124. Yamaguchi, T., H. Satake, and N. Fukushima, *Band diagram and carrier conduction mechanisms in ZrO_2 MIS structures.* IEEE Transactions on Electron Devices, 2004. **51**(5): p. 774-779.

125. Emtage, P.R. and W. Tantraporn, *Schottky Emission Through Thin Insulating Films.* Physical Review Letters, 1962. **8**(7): p. 267-268.

126. Wang, H., et al., *Interface control and leakage current conduction mechanism in HfO_2 film prepared by pulsed laser deposition.* Applied Physics Letters, 2008. **93**(20): p. 202904-202904.

127. Delfag, M., et al., *Sinter-free inkjet-printed PEDOT:PSS/WO_3/PEDOT:PSS flexible valency change memory.* Flexible and Printed Electronics, 2021. **6**(3): p. 035011-035011.

128. Zhao, X. and D. Vanderbilt, *First-principles study of structural, vibrational, and lattice dielectric properties of hafnium oxide.* Physical Review B, 2002. **65**(23): p. 233106-233106.

129. Tung, R.T., *The physics and chemistry of the Schottky barrier height.* Applied Physics Reviews, 2014. **1**(1): p. 011304-011304.

130. Materano, M., et al., *Interplay between oxygen defects and dopants: effect on structure and performance of HfO_2-based ferroelectrics.* Inorganic Chemistry Frontiers, 2021. **8**(10): p. 2650-2672.

131. Rodenbücher, C., et al., *Is reduced strontium titanate a semiconductor or a metal?* Crystals, 2021. **11**(7): p. 744-744.